CENTRO DE INVESTIGACIÓN Y DE ESTUDIOS AVANZADOS

DEL INSTITUTO POLITÉCNICO NACIONAL

UNIDAD QUERÉTARO

The initial stages of the ALD growth of HfO_2 films on SiO_2 and H-terminated Si (001) substrates

by

Mayra Daniela Morales Acosta

for obtain degree of

Master of Science

in

Materials Science

CINVESTAV IPN
USB INFORMACION Y DOCUMENTACION
SERVICIO DOCUMENTAL

CINVESTAV
IPN
ADQUISICION
DE LIBROS

Thesis Directors:

Dr. Alberto Herrera Gómez

Dr. Francisco Servando Aguirre Tostado

Santiago de Querétaro, Qro. November, 2007.

CENTRO DE INVESTIGACIÓN Y DE ESTUDIOS AVANZADOS

DEL INSTITUTO POLITÉCNICO NACIONAL

UNIDAD QUERÉTARO

Las etapas iniciales del crecimiento por ALD de películas de HfO_2 sobre substratos de Si (001) terminados en H y SiO_2

Tesis que presenta

Mayra Daniela Morales Acosta

para obtener el grado de

Maestro en Ciencias

en la Especialidad de

Materiales

Directores de Tesis:

Dr. Alberto Herrera Gómez

Dr. Francisco Servando Aguirre Tostado

Santiago de Querétaro, Qro. Noviembre 2007

CLASIF.: TA404.2 .M67 2007
ADQUIS.: SSI-099
FECHA: 3-VI-2008
PROCED.: DON-2008
$

I.D. 137816-2001

To my family with love and gratitude
for all their support and inspiration.

Acknowledgments

I am profoundly indebted to Dr. Jiyoung Kim who could not be listed as advisor but without his support I could have not initiated or developed my thesis work.

My special thanks goes to my advisor Professor Alberto Herrera Gómez for sharing his knowledge and providing me with so many opportunities. I am thankful for his indispensable support of my master degree studies.

My sincere thanks to my advisor Dr. F. Servando Aguirre Tostado, who encouraged me and granted me lots of patience, for his support on my research work at every step. His help in the understanding of many theories and in the interpretation of the experimental results, together with his insights and discussions, were invaluable.

I wish to offer my sincere gratitude to Professor Robert M. Wallace for his support. I am especially grateful for his insightful comments, for giving me the opportunity to work in his research group and use the experimental equipment that was fundamental in this dissertation.

I would like to acknowledge Dr. Manuel Quevedo Lopez for his sincere advice. His generosity and guidance were very important to complement my work.

I would also like to thank my committee members, Dr. Rafael Ramirez Bon and Dr. Francisco J. Espinoza Beltrán for their insightful comments on my research work.

I would like to extend my gratitude to Conacyt, especially to "Becas Mixtas" program for the financial support that has made this project possible.

I want to express my gratitude to The University of Texas at Dallas as an institution, to all the personal of the Department of Materials Science and Engineering, and to the staff members of the Clean Room, for the facilities necessary to complete the experimental part of this dissertation. I offer my sincere recognition to Dr. Rodolfo Hernandez Guerrero, director of the Center for U.S-Mexico Studies, for all his help and generosity.

During my studies at Cinvestav and at The University of Texas at Dallas I had the opportunity to meet several collaborators and friends, including Maribel Maldonado, Isabel Medina, Pilar Montellano, Cecilia Juárez, Rocío Contreras, P. Giovanni Maní, Bongki Lee, Miles Selvidge and Rahul Gupta. They made my studies and research work very enjoyable and my stay a memorable experience.

I was blessed with a wonderful family. I am grateful for my Dad who is now my angel. I thank him for providing me the courage to always go forward smiling. I would like to thank to my mom for so much love. When I grow up I want to be just like her. I would like to thank to my dear twin sisters, Diana and Ariana, who were beside me all the time encouraging me and being my accomplices. To my brothers, Daniel and Mario, I thank them for their love and support throughout my research career, without which I would not have come so far.

Resumen

Las películas de óxido de Hafnio sobre Si han sido extensamente investigadas como un material con alta constante dieléctrica para la nueva generación de dispositivos MOS (Metal-Oxido-Semiconductor). El método de Depósito por Capa Atómica (ALD por sus siglas en inglés) es el más ampliamente utilizado para el crecimiento de películas de HfO_2, debido a que ofrece un excelente control de estructura y espesor. Se cree que la formación desenfrenada de óxido de silicio y silicatos durante el deposito de HfO_2 sobre Si afecta el rendimiento eléctrico de dispositivos MOS basados en Hafnio. Con la finalidad de estudiar los efectos de la preparación de la superficie del substrato se crecieron por ALD películas de HfO_2 sobre obleas de Si (100) terminadas en SiO_2 e Hidrógeno. Para entender las etapas iniciales del crecimiento de películas de HfO_2 se realizaron experimentos usando 5-ciclos y 30-ciclos en ALD. La morfología de la superficie y la composición fueron caracterizadas por Microscopía de Fuerza Atómica (AFM), Espectroscopia de Infrarrojo por Transformada de Fourier (FTIR), y Espectroscopia de Fotoelectrones de Rayos-X con Resolución Angular (ARXPS) en alta resolución. A través de un análisis apropiado y autoconsistente de los datos obtenidos de ARXPS fue posible obtener detalles sin precedente acerca de la estequiometría y el espesor de las multicapas formadas. Nuestro estudio reveló la presencia de una capa intermedia de $Hf_xSi_{1-x}O_y$ con x~80% para las dos preparaciones de la superficie para las películas de 30-ciclos. Fue interesante notar que, en las fases iniciales del crecimiento de ALD, la capa de silicato de hafnio tiene deficiencias de oxígeno, mientras que en las películas de 30 ciclos éste silicato es estequiométrico.

Abstract

Hafnium oxide films on Si have been intensively investigated as a high-κ dielectric material for the new generation of MOS devices. Atomic Layer Deposition (ALD) is the preferred method to grow this material because of its excellent thickness control and conformality. The uncontrolled formation of silicon oxide and silicates during the Hafnium oxide deposition on silicon is believed to affect the electrical performance of Hf-based MOS devices. To study the effect of the substrate surface preparation on the structure, we grew HfO_2 films by ALD on SiO_2-terminated and on H-terminated Si (100) substrates. Experiments on 5-cycle and 30-cycle ALD HfO_2 films were performed in order to understand the initial stages of the growth. The surface morphology and composition were characterized by Atomic Force Microscopy, Fourier Transform Infrared Spectroscopy, and high-resolution Angle Resolved X-Ray Photoelectron Spectroscopy (ARXPS). Through appropriate self consistent analysis of ARXPS data it was possible to obtain unprecedent details regarding the stoichiometry and thickness of the multiple layers formed. Our study revealed the presence of a $Hf_xSi_{1-x}O_y$ interlayer with x~80% for both surface preparations for the 30-cycle films. It was interesting to notice that, in the early stages of the ALD growth, the hafnium silicate layer was oxygen deficient, while after 30 cycles it was not.

Outline

Resumen v
Abstract vi
List of tables ix
List of figures x
Acronyms xvi
Chapter 1. Introduction 1
1.1 Background 1
1.1.1 Justification 2
1.2 Objectives 3
1.2.1 General Objective 3
1.2.2 Specific Objectives and Goals 3
1.3 Outline of the Thesis 4
References (Chapter 1) 4
Chapter 2. Angle Resolved X-Ray Photoelectron Spectroscopy (ARXPS) 6
2.1 Photoelectron Spectroscopy 6
2.2 X-Ray Photoelectron Spectroscopy (XPS) 7
2.3 Principles of the Technique 8
2.4 Electron spectrometer Design 10
2.4.1 Vacuum system 10
2.4.2 Sample 11
2.4.3 Analyzers 11
2.5 Spectra Characteristics 12
2.5.1 Core level 12
2.6 Components of an XPS system 13
2.6.1 X-Ray source 14
2.7 Angle Resolved XPS 17
2.8 Data Analysis 18
2.8.1 Data Fitting (AAnalyzer®) 19
2.8.2 Modeling of the Angle Resolved XPS Data (XPSGeometry®) 20
2.8.3 Parameters Employed in the Calculations 22
References (Chapter 2) 24
Chapter 3. Experimental Techniques 26
3.1 Aqueous Chemical Wafers Cleaning Process 26
3.2 RCA Cleaning 26
3.2.1 Organic Removal 27
3.2.2 Native Oxide Removal 27
3.2.3 Particle Removal with Simultaneous Oxide Regrowth 28
3.2.4 Metal Removal 28

3.3 Rinsing and Drying 29
3.4 Atomic Layer Deposition (ALD) 29
3.4.1 Requirements for Self-terminating Reactions 31
3.4.2 Precursors 34
3.4.3 Deposition Equipment 36
3.4.4 Comparison of Deposition Techniques 37
3.5 Atomic Force Microscopy 38
3.6 Fourier Transformed Infrared (FTIR) Spectroscopy 38
References (Chapter 3) 38
Chapter 4. Experimental Details and Results 41
4.1 Description of the Samples 41
4.2 Substrate Preparation 42
4.3 Thermal Growth of 1nm SiO_2 Layer 43
4.3.1 UV Ozone 44
4.3.2 O_2 Annealing 44
4.3.3 SiO_2 Film Thickness Measurement by XPS 44
4.4 ALD Growth of HfO_2 Films 45
4.5 Atomic Force Microscopy Images 48
4.6 Fourier Transmission Infrared Spectroscopy 51
4.7 Angle Resolved XPS 55
4.7.1 Data acquisition 55
4.7.2 Sample Heating in UHV 57
4.7.3 XPS Survey 58
4.7.4 XPS Analysis of HfO_2 on H-terminated Si Substrate Using 5 ALD Cycles 60
4.7.5 XPS analysis of HfO_2 on SiO_2-terminated Si Substrate Using 5 ALD cycles 66
4.7.6 XPS Analysis of HfO_2 on H-terminated Si Substrate Using 30 ALD Cycles 72
4.7.7 XPS Analysis of HfO_2 on SiO_2-terminated Si Substrate Using 30 ALD Cycles 78
4.7.8 Summary of the Fits 84
References (Chapter 4) 86
Chapter 5. Analysis Results and Discussion 87
5.1 Atomic Force Microscopy (AFM) 87
5.2 Fourier Transmission Infrared Spectroscopy (FTIR) 87
5.3 Angle Resolved XPS: Data Analysis 88
5.4 Stoichiometry 92
Conclusions 95
Future Work 97

List of tables

Table 2.1 Set of parameters obtained in the characterization of the XPS equipment. A previous work very complete about it was carried out. 22

Table 2.2 The kinetic energy and cross section of the photoelectrons employed in the calculations were found in the literature. 23

Table 2.3 Effective Attenuation Length values were calculated using the NIST Electron Effective Attenuation Length Database. Lattice constant of the layers and bulk were calculated too. 23

Table 2.4 Core level parameters employed in the calculation of the effective attenuation lengths with the software provided by NIST 24

Table 2.5 Layer parameters employed in the calculation of the effective attenuation lengths with the software provided by NIST.[10] 24

Table 3.1 Comparison of deposition properties for PVD, CVD, and ALD. 37

Table 4.1 Modified RCA wafer cleaning process 42

Table 4.2 ALD process matrix. 47

Table 4.3 Summary of binding energy for all the samples studied. 85

Table 4.4 Summary of Gaussian values for all the samples studied. 85

Table 5.1 Stoichiometry and thickness of the samples. 93

List of figures

Figure 2.1 Schematic representation of photoemission process. 8

Figure 2.2 Energy level for binding energy for metallic samples. 9

Figure 2.3 Diffraction of X-rays at a quarts crystal. 16

Figure 2.4 Compositional depth profiling in ARXPS 18

Figure 2.5 Fitting and deconvolution using AAnalyzer®. 19

Figure 2.6 Illustration of the used square box depth profile model of a buried layer with a chemical specie "*S*" at a depth d_i with a thickness t and for a take-off angle α. 21

Figure 2.7 Qualitative illustration of peak area dependence in Angle Resolved XPS for a chemical specie in a thin layer that is on the surface (left) or buried (right). 22

Figure 3.1 Typical sequence for one unit cycle of the ALD process to obtain AB films by using AX_n and BX_n precursors. 30

Figure 3.2 Adsorption classes. 31

Figure 3.3 Three different types of monolayers relevant to ALD: a) a chemisorbed monolayer (the substrate before chemisorption indicated above, with reactive sites shown), b) a physisorbed monolayer, and c) a monolayer of the ALD-grown material. 32

Figure 3.4 Examples of how the amount of material adsorbed can vary with time. 32

Figure 3.5 Schematic representation of five reaction cycles, assuming irreversible adsorption. 33

Figure 4.1 Cleanroom Research Laboratory at The University of Texas at Dallas. 41

Figure 4.2 Sample preparation process. 42

Figure 4.3 Si 2p spectrum of 1 nm SiO_2 thermally grown before HfO_2 deposition. 44

Figure 4.4 TEMA-Hf molecule. TEMA-Hf was employed as Hf source in the Hafnium oxide deposition by ALD. 46

Figure 4.5 ALD Cambridge Nano Tech system. The system allows a perfect temperature control during the deposition. 46

Figure 4.6 Reactor pressure during 5 cycles of HfO_2 ALD deposition. 48

Figure 4.7 Reactor pressure during 30 cycles of HfO_2 ALD deposition. 48

Figure 4.8 AFM topographs of the HfO_2 films on H-terminated substrates grown by ALD using 5 cycles. 49

Figure 4.9 AFM topographs of the HfO_2 films on SiO_2-terminated substrates grown by ALD using 5 cycles. The RMS average roughness is 0.16 nm for 5-cycles samples. 49

Figure 4.10 AFM topographs of the HfO_2 films on H-terminated substrates grown by ALD using 30 cycles. ALD growth allows to obtain very uniform films and with good conformality. 50

Figure 4.11 AFM topographs of the HfO_2 films on SiO_2-terminated substrates grown by ALD using 30 cycles. The RMS average roughness is 0.15 nm for 30-cycles samples. 50

Figure 4.12 Comparison of the absorption FTIR spectra between samples using 5 ALD cycles on different terminated Si substrate: H-terminated and SiO_2-terminated. The shift of the O-Si-O band for the H-terminated sample might be attributed to the lack of a fully formed silicon oxide. The SiO_2 terminated sample showed a larger signal for the Si-O-Hf band. 52

Figure 4.13 Comparison of the absorption FTIR spectra between samples using 30-ALD cylces on different substrate terminations. The band associated to Si-O-Hf is more apparent for the SiO_2-terminated sample. 53

Figure 4.14 Comparison of the absorption FTIR spectra between samples with H-terminated Si substrate using different number of cycles (5 and 30) during the ALD HfO_2 deposition. The shift of the O-Si-O band for the H-terminated sample might be attributed to the lack of a fully formed silicon oxide. The SiO_2 terminated sample showed a larger signal for the Si-O-Hf band. 54

Figure 4.15 Comparison of the absorption FTIR spectra between samples with SiO_2-terminated Si substrate using different number of cycles (5 and 30) during the ALD HfO_2 deposition. The band associated to O-Hf-O indicates a clear evidence of hafnium oxide growth for 30-cycles sample, while in 5-cycles samples there is not. 54

Figure 4.16 UHV deposition and characterization cluster tool at the University of Texas at Dallas. 56

Figure 4.17 Spectroscopy chamber used for ARXPS experiments. 56

Figure 4.18 Angle Resolved XPS experiment. 57

Figure 4.19 In-situ annealing in UHV to 300 ºC for 20 minutes previous to Angle Resolved XPS measurements. 58

Figure 4.20 Survey for samples with 5 ALD cycles with different substrate terminations. This wide scan allows to identify the chemical components present in the sample and to define acquisition windows. 59

Figure 4.21 Survey for samples with 30 ALD cycles with different substrate terminated. Si 2p, Hf 4f, C 1s, O 1s and F 1s lines were recorded at high resolution for an appropriate ARXPS analysis 59

Figure 4.22 Core level Si 2p XPS spectrum at 25° for 5 ALD cycles of HfO_2 deposited on a H-terminated Si substrate. The binding energy difference between Si in the bulk and in $Hf_{0.33}Si_{0.67}O_{1.62}$ is 3.0 eV. 61

Figure 4.23 Angle Resolved XPS for Si 2p region of HfO_2 film on H-terminated Si substrate using 5 ALD cycles. 61

Figure 4.24 Core level Hf 4f XPS spectrum at 25° for 5 ALD cycles of HfO_2 deposition on H-terminated Si substrate. Only one chemical component is present. As it will be shown in Chapter 5, this component corresponds to hafnium silicate (18.2eV) 62

Figure 4.25 Angle Resolved XPS for Hf 4f region of HfO_2 film on H-terminated Si substrate using 5 ALD cycles. 63

Figure 4.26 Core level O 1s XPS spectrum at 25° of HfO_2 film on H-terminated Si substrate using 5 ALD cycles. The spectrum clearly showed two peaks separated by 0.75eV, one associated to silicon oxide (532.4 eV) and another to hafnium silicate (531.65 eV). 64

Figure 4.27 Angle Resolved XPS for O 1s region of HfO_2 film on H-terminated Si substrate using 5 ALD cycles. 64

Figure 4.28 Angle Resolve XPS for core level C 1s of HfO_2 film on H-terminated Si substrate using 5 ALD cycles. The spectrum clearly showed two chemical species, one associated to C-C bond (285 eV) and another to C-H bond (286.3 eV). 65

Figure 4.29 Angle Resolve XPS for core level F 1s of HfO_2 film on H-terminated Si substrate using 5 ALD cycles. The spectrum clearly showed one chemical specie associated to Fluorine (685.8 eV). 66

Figure 4.30 Core level Si 2p XPS spectrum at 25° of HfO_2 film on SiO_2-terminated Si substrate using 5 ALD cycles. The binding energy difference between Si in the bulk and in $HfSi_xO_y$ is 3.5 eV. 67

Figure 4.31 Angle Resolved XPS for Si 2p region of HfO_2 film on SiO_2-terminated Si substrate using 5 ALD cycles. 67

Figure 4.32 Core level Hf 4f XPS spectrum at 25° of HfO_2 film on SiO_2-terminated Si substrate using 5 ALD cycles. The best fitting was done using two peaks. As it is shown in Chapter 5, both corresponding to hafnium silicate. 68

Figure 4.33 Angle Resolved XPS for Hf 4f region of HfO_2 film on SiO_2-terminated Si substrate using 5 ALD cycles. Employing a pass energy of 15eV resulted in high resolution XPS data that allowed for the proper deconvolution of the peaks. 69

Figure 4.34 Core level O 1s XPS spectrum at 25° of HfO_2 film on SiO_2-terminated Si substrate using 5 ALD cycles. The spectrum clearly showed two peaks separated by 1.30eV, one associated to silicon oxide (532.6eV) and another to silicate (532.6eV). 70

Figure 4.35 Angle Resolved XPS for O 1s region of HfO_2 film on SiO_2-terminated Si substrate using 5 ALD cycles. 70

Figure 4.36 Angle Resolve XPS for core level C 1s of HfO_2 film on SiO_2-terminated Si substrate using 5 ALD cycles. The spectrum clearly showed two chemical species, one associated to C-C bond (284.9 eV) and another to C-H bond (286.2 eV). 71

Figure 4.37 Angle Resolve XPS for core level F 1s of HfO_2 film on SiO_2-terminated Si substrate using 5 ALD cycles. The spectrum clearly showed one chemical specie associated to Fluorine (685.5 eV). 72

Figure 4.38 Core level Si 2p XPS spectrum at 25° of HfO_2 film on H-terminated Si substrate using 30 ALD cycles. The binding energy difference between Si in the bulk and in $HfSi_xO_y$ in this case is 3.1eV. 73

Figure 4.39 Angle Resolved XPS for Si 2p region of HfO_2 film on H-terminated Si substrate using 30 ALD cycles. 73

Figure 4.40 Core level Hf 4f XPS spectrum at 25° of HfO_2 film on H-terminated Si substrate using 30 ALD cycles. Two chemical components are present. As it will be shown in Chapter 5, one corresponds to hafnium silicate and another to hafnium oxide. The binding energy difference between them is 0.40 eV. 74

Figure 4.41 Angle Resolved XPS for Hf 4f region of HfO_2 film on H-terminated Si substrate using 30 ALD cycles. 75

Figure 4.42 Core level O 1s XPS spectrum at 55° of HfO_2 film on H-terminated Si substrate using 30 ALD cycles. The shape of oxygen spectra

allows three peaks deconvolution, the first associated to hafnium oxide (531.2eV), the second attributed to hafnium silicate (532eV) and the third to silicon oxide (533.1eV). 76

Figure 4.43 Angle Resolved XPS for O 1s region of HfO_2 film on H-terminated Si substrate using 30 ALD cycles. 76

Figure 4.44 Angle Resolve XPS for core level C 1s of HfO_2 film on H-terminated Si substrate using 30 ALD cycles. The spectrum clearly showed two chemical species, one associated to C-C bond (285.3 eV) and another to C-H bond (286.6 eV). 77

Figure 4.45 Angle Resolve XPS for core level F 1s of HfO_2 film on H-terminated Si substrate using 30 ALD cycles. The spectrum clearly showed one chemical specie associated to Fluorine (685.6 eV). 78

Figure 4.46 Core level Si 2p XPS spectrum at 25° of HfO_2 film on SiO_2-terminated Si substrate using 30 ALD cycles. The binding energy difference between Si in the bulk and in $Hf_{0.77}Si_{0.23}O_{2.12}$ is 3.1 eV. 79

Figure 4.47 Angle Resolved XPS for Si 2p region of HfO_2 film on SiO_2-terminated Si substrate using 30 ALD cycles. 79

Figure 4.48 Core level Hf 4f XPS spectrum at 25° of HfO_2 film on SiO_2-terminated Si substrate using 30 ALD cycles. Two chemical components are present. As it is shown in Chapter 5, one associated to hafnium silicate and the other to hafnium oxide. The binding energy difference between them is 0.50 eV. 80

Figure 4.49 Angle Resolved XPS for Hf 4f region of HfO_2 film on SiO_2-terminated Si substrate using 30 ALD cycles. 81

Figure 4.50 Core level O 1s XPS spectrum at 25° of HfO_2 film on SiO_2-terminated Si substrate using 30 ALD cycles. The shape of oxygen spectra allows three peaks deconvolution, one associated to hafnium oxide (531.3eV), other attributed to hafnium silicate (532.4eV) and the last to silicon oxide (533.2eV). 82

Figure 4.51 Angle Resolved XPS for O 1s region of HfO_2 film on SiO_2-terminated Si substrate using 30 ALD cycles. 82

Figure 4.52 Angle Resolve XPS for core level C 1s of HfO_2 film on SiO_2-terminated Si substrate using 30 ALD cycles. The spectrum clearly showed two chemical species, one associated to C-C bond (285.3 eV) and another to C-H bond (286.6 eV). 83

Figure 4.53 Angle Resolve XPS for core level F 1s of HfO_2 film on SiO_2-terminated Si substrate using 30 ALD cycles. The spectrum clearly showed one chemical specie associated to Fluorine (685.6 eV). 84

Figure 5.1 Absorption FTIR spectra for samples studied: diferent Si substrate terminated and using 5 or 30 ALD cycles. 87

Figure 5.2 Parameters obtained of the equipment characterization. 88

Figure 5.3 ARXPS modeled data for Si 2p in bulk for all four samples studied. 89

Figure 5.4 Area-angle dependence of Si 2p in Silicon oxide comparing experimental and modeled data. 89

Figure 5.5 Area-angle dependence of Si 2p in Hafnium Silicate comparing experimental and modeled data. 90

Figure 5.6 Area-angle dependence of Hf 4f in Hafnium Silicate comparing experimental and modeled data. 91

Figure 5.7 Area-angle dependence of Hf 4f in Hafnium Oxide comparing experimental and modeled data. 91

Figure 5.8 Area-angle dependence of O 1s total comparing experimental and modeled data. 92

Acronyms

ALD. Atomic Layer Deposition

ALE. Atomic Layer Epitaxy

AFM. Atomic Force Microscopy

ARXPS. Angle Resolved X-Ray Photoemission Spectroscopy

CVD. Chemical Vapor Deposition

EOT. Equivalent Oxide Thickness

ESCA. Electron Spectroscopy for Chemical Analysis

FTIR. Fourier Transmission Infrared Spectroscopy

FWHM . Full Width at Half Maximum Intensity

GPC. Growth per cycle

ML. Monolayer

PVD. Physical Vapor Deposition

RCA. Radio Corporation of America

TEMA-Hf. Tetrakis-ethylmethylamino-Hafnium

SC. Standard Cleaning

XPS. X-Ray Photoemission Spectroscopy

UHV. Ultra-High Vacuum

UPS. Ultraviolet Photoelectron Spectroscopy

Chapter 1

Introduction

This chapter provides an introduction to the subject and motivation of this work. The objectives and goals of the present thesis are also included stressing the importance of this dissertation and how each objective proposed was achieved.

Chapter 1. Introduction

1.1 Background

As the size of silicon dioxide-based transistors continues to be sized down, the leakage current in the metal-oxide semiconductor (MOS) devices becomes unacceptably high. The need for high-κ gate dielectrics has been emphasized in numerous scientific reports.[1,2,3] There is a strong need to find "high-*κ*" gate dielectrics for future MOS devices as a replacement for SiO_2. Recently, hafnium dioxide (HfO_2) has been intensively investigated as a potential gate dielectric candidate for MOS applications because of its high dielectric constant enabling the use of thicker oxide films.

The understanding and prediction of the properties of matter at atomic level represents one of the great achievements of contemporary materials science. In this context, the advances of photoelectron spectroscopy, in the study of chemical bonding and structure of materials is due to the improvement of the experimental technique and fundamental understanding of electron transport in solids. The photoemission technique has been developed sufficiently to become a major tool for the experimental studies of solids.[4]

Comparing various methods for materials deposition, atomic layer deposition (ALD) has a large potential. With this technique very well controlled growth, almost atomic layer by atomic layer, of the desired species from gaseous precursors is possible. ALD deposited ultrathin high-K dielectric films has recently penetrated research and manufacture lines of several major memory and logic industry due to the precise control of thickness, uniformity, quality and material properties.[5] Currently, the ALD technique is drawing significant attention in semiconductor research and development as an enabling technology with a wide range of possible applications in electronic devices manufacturing. Proposals for replacing the conventional SiO_2 growth process for gate dielectric using ALD deposited high-k films is quite promising and may be essential for the future development of Si-based nano-range semiconductor devices.

The aim of this thesis is to present a detailed study of the chemical bonding and structure occurring during the initial stages of ALD deposition of HfO_2 on Si. The samples used in this study included two different substrate terminations, H- and SiO_2-terminated Si(001) substrates and two different thickness, 5 and 30 ALD cycles of hafnium dioxide. The initial p-type Si(001) substrates used, were cleaned before deposition by a modified RCA cleaning method. Structural and chemical characterization was performed to identify the possible formation of multilayer during the hafnium oxide deposition using ARXPS, AFM and FTIR techniques. Finally the compositional depth profile was obtained through a meticulous and self consistent analysis of ARXPS data.

Hafnium dioxide depositions by ALD technique and the ARXPS, AFM and FTIR measurements were performed in the Department of Materials Science and Engineering at The University of Texas at Dallas.

1.1.1 Justification

Numerous high-k dielectrics have been studied for the purpose of replacing the SiO_2 gate dielectric in existing devices. In recent years, hafnium based gate dielectrics have gathered much research attention. It has been extensively studied and will posibilly be the gate dielectric of choice. [6,7,8]. The successful integration Hf-based high-k dielectrics in a MOS devices has been demonstrated by several research groups using a conventional self aligned process flow.

ALD is the most sophisticated and widely used technique for HfO_2 deposition which involves cyclic deposition and oxidation on the substrate. A precise control over thickness can be achieved using this process, however, precursor induced contamination of the film (impurities) can be an issue.[9] A high purity of HfO_2 film can be achieved using ALD at the expense of the thickness control. ALD deposition of metal gates is possible and causes very less damage to the surface of the gate dielectric and control over the thickness of the metal can also be achieved.

The ALD HfO_2 on Si substrates results in the growth of an undesired interfacial layer. The composition of this interfacial layer has been reported to vary from a poor quality

SiO_x to hafnium silicate ($HfSiO_x$) that has a lower dielectric constant than HfO_2 gate dielectric.[7] As a result, the effective dielectric constant of the gate dielectric stack decreases and the equivalent oxide thickness (EOT) of devices increases.[10]

On the other hand, the precursors involved in the depositions can contaminate the gate dielectric and can also lead to an increase in the EOT. The surface conditions of the gate dielectrics alter significantly from one metal or dielectric deposition technique to another, which can lead to differences in the observed effective work function of metals from one deposition technique to another.[11,12]

In this context, is important to understand how is the ALD growth of hafnium oxide at the initial deposition stages by means of a detailed compositional depth profile of the "as deposited" films.

1.2 Objectives

According to the problematic previously explained, it is important to describe the objectives to define the purpose of this work.

1.2.1 General Objective

The main objective in this thesis is to characterize the initial stages of HfO_2 films grown by ALD (using TEMA-Hf) on H-terminated and SiO_2-terminated a silicon substrate. The techniques employed were high resolution ARXPS (Chapter 2), AFM (Chapter 3) and FTIR (Chapter 3).

1.2.2 Specific Objectives and Goals

It is helpful to understand how the hafnium dioxide growth is affected on different substrate terminations. The general objective is achieved through the next specific objectives and goals:

a) To deposit HfO_2 films on Si(001) p-type substrates by ALD using TEMA-Hf precursor.

- To grow HfO_2 on H-terminated Si substrate.
- To grow HfO_2 on SiO_2/Si substrate.

b) To study the differences of growing HfO_2 ultra-thin films on two different surfaces: H-terminated and SiO_2-terminated.

- Morphology study using AFM.
- Composition and structure using FTIR.
- Stoichiometry and thickness through high resolution ARXPS.
- It is useful to reveal the possible presence of multilayers formed and its qualitative and quantitative analysis to obtain the corresponding film depth profiles.

1.3 Outline of the Thesis

The structure of this thesis consist of five additional chapters: It starts by describing ARXPS (Chapter 2), the central technique employed in this thesis. In Chapter 3, together with a brief description of other experimental techniques used for sample preparation and characterization as AFM and FTIR. Chapter 4 includes the experimental details and the results obtained. The analysis and discussion of results are described in Chapter 5. Finally the conclusions and future work are presented at the end.

References (Chapter 1)

1 R.M.Wallace and G. Wilk, "High-k Dielectric Materials for Microelectronics," Critical Reviews in Solid State and Materials Sciences 28, 231 (2003) (Invited Review).

2 M. Houssa, in High-κ Dielectrics, M. Houssa, editor, p.p. 3-13, Institute of physics Publishing, Bristol (2004).

3 Prakaipetch Punchaipetch, Gaurang Pant, Manuel A. Quevedo-Lopez, C. Yao, Mohamed El-Bouanani, Moon J. Kim, Robert M. Wallace and Bruce E. Gnade, IEE Journal of selected topics in Quantum electronics, Vol. 10, No.1 (2004).

4 Albert F Takacs, Electronic structure studies of metal-organic and intermetallic compounds, Osnabruck University (2005).

5 Ofer Sneh, Robert B. Clarck-Phelps, Ana R. Londergan, JereldWinkler and Thomas E. Seidel, Thin solid films 402, 248-261 (2002).

6 A.J. Craven, M. MacKenzie, D.W. McComb, F.T. Docherty, "Investigating physical and chemical changes in high-k gate stacks using nanoanalytical electron microscopy", Microelectronic Engineering, Vol.80, pp 90–97 (2005).

7 P D. Kirsch, C.S. Kang, J. Lozano, J.C. Lee, J.G. Ekerdt, "Electrical and spectroscopic comparison of HfO2/Si interfaces on nitrided and un-nitrided Si(100)", Journal of Applied Physics, Vol. 91, No.7, April (2002).

8 G. Lucovsky, G.B. Rayner, R.S. Johnson, "Chemical and Physical Limits on the Performance of Metal Silicate High-k Gate Dielectrics", Microelectronics Reliability, Vol.41, pp 937-945 (2001).

9 Annelies Delabie, Matty Caymax, Bert Brijs, David P. Brunco, Thierry Conard, Erik Sleeckx, Sven Van Elshocht, Lars-Åke Ragnarsson, Stefan De Gendt, and Marc M. Heyns, "Scaling to Sub-1 nm Equivalent Oxide Thickness with Hafnium Oxide Deposited by Atomic Layer Deposition", Journal of The Electrochemical Society, 153(8), F180-F187 (2006).

10 CeO_2 and HfO_2 High-k gate dielectrics by pulsed laser deposition: from binary oxides to nanolaminates, Koray Karakaya, University of Twente, Enschede, Netherlands (2006).

11 K. J. Park,a J. M. Doub, T. Gougousi, and G. N. Parsons "Microcontact patterning of ruthenium gate electrodes by selective area atomic layer deposition", Applied Physics Letters, Vol. 86, Issue 5, 051903 (2005).

12 Sandwip K. Dey, Jaydeb Goswami, Diefeng Gu Henk de Waard, Steve Marcus, and Chris Werkhoven, "Ruthenium films by digital chemical vapor deposition: Selectivity, nanostructure, and work function", Applied Physics Letters, Vol. 84, Issue 9 (2004).

Chapter 2

Angle Resolved X-Ray Photoelectron Spectroscopy (ARXPS)

The Angle Resolved X-Ray Photoemission Spectroscopy (ARXPS) technique has been developed sufficiently to become one of the major tools for the experimental studies of ultra thin films. The advances of this technique, in the study of chemical bonding and structure of materials allow the understanding and prediction of the properties of matter at atomic level. The theoretical details and the principles for the analysis of ARXPS data are presented in this chapter.

Chapter 2. Angle Resolved X-Ray Photoelectron Spectroscopy (ARXPS)

Surface chemical analysis underpins many developments in Micro and Nanotechnology. The analytical techniques established for over thirty years are now facing new challenges with the creation of devices requiring the analysis of smaller areas, thinner films, and more complex geometries. Advances in instrumentation have resulted in increasingly detailed data about the chemical composition of a surface, so that efficient spectrum is a now a vital component of successful surface analysis.

A successful technique for analyzing surfaces must have at least two characteristics[1]:

- It must be extremely sensitive.
- It must be efficient at filtering out signal from the vast majority of the atoms deeper into the sample.

2.1 Photoelectron Spectroscopy

In surface and thin film analysis the most important photon absorption process is the photoelectric effect. In this process an incident photon of energy $\hbar\omega$ transfers all of its energy to a bound electron in an atom. The photoelectric process is a direct signature of the photon interaction with the atom and is the basis of one of the major analytical tools: Photoelectron Spectroscopy.[2]

Photoelectron Spectroscopy utilizes photo-ionization and energy-dispersive analysis of the emitted photoelectrons to study the composition and electronic state of the surface region of a sample. According to the source of exciting radiation the technique has been subdivided:

- X-Ray Photoelectron Spectroscopy (XPS). Using soft X-Ray (200-2000 eV) radiation to examine core-levels.
- Ultraviolet Photoelectron Spectroscopy (UPS). Using vacuum ultraviolet (10-45 eV) radiation to examine valence.

The transitions are labeled according to the principal quantum number, the orbital angular number (usually given a letter rather than a number as *s,p,d,f*), and the total angular quantum number. The peaks in XPS spectra, derived form orbitals whose angular momentum quantum number is greater than 0, are usually split into two. This is a result of the interaction of the electron angular momentum due to its spin with its orbital angular momentum. Each electron has a quantum number associated with its spin angular momentum, s^2. The value of s can be either +1/2 or -1/2.[2]

The two angular momenta are added vectorially to produce the quantity *j* in the expression nl_j, $j = |l \pm s|$. The relative intensity of the components of the doublets formed by the spin orbit coupling is dependent upon their relative populations (degeneracies) which are given by the expression $(2j+1)$. The spacing between the components of the doublets depends upon the strength of the spin orbit coupling. For a given value of both *n* and *l* the separation increases with the atomic number of the atom. For a given atom, it decreases both with increasing *n* and with increasing *l*. [2]

2.2 X-Ray Photoelectron Spectroscopy (XPS)

X-ray Photoelectron Spectroscopy (XPS) is a form of electron spectroscopy in which a sample is irradiated with a beam of monochromatic x-rays and the energies of the resulting photoelectrons are measured. It is sometimes known by the alternative acronym *Electron Spectroscopy for Chemical Analysis* (ESCA).

XPS is a quantitative spectroscopic technique that measures the empirical formula, chemical state and electronic state of the elements that exist within a material. XPS spectra are obtained by irradiating a material with a beam of X-rays while simultaneously measuring the kinetic energy (KE) and number of electrons that escape from the top 1 to 10 nm of the material being analyzed. XPS requires ultra-high vacuum (UHV) conditions. XPS detects all elements with an atomic number (Z) between those of Lithium (Z=3) and Lawrencium (Z=103). This limitation means that it cannot detect hydrogen (Z=1) or Helium (Z=2).[1]

2.3 Principles of the Technique

The base of the Photoelectron Spectroscopy data acquisition is based on the photoelectric effect. The process of photoemission is shown schematically in Figure 2.1. A photon of known energy is used to impart energy on an electron. The electron uses this energy to overcome the binding energy holding it to the atom. The electrons remaining energy is in the form of kinetic energy, which is measured. Thus the binding energy for the electron is determined by taking the difference between the incident photons energy and the kinetic energy possessed by the photoelectron. The energy of the emitted photoelectrons is analyzed by the electron spectrometer and the data presented as a graph of intensity (counts or counts/second versus electron energy).

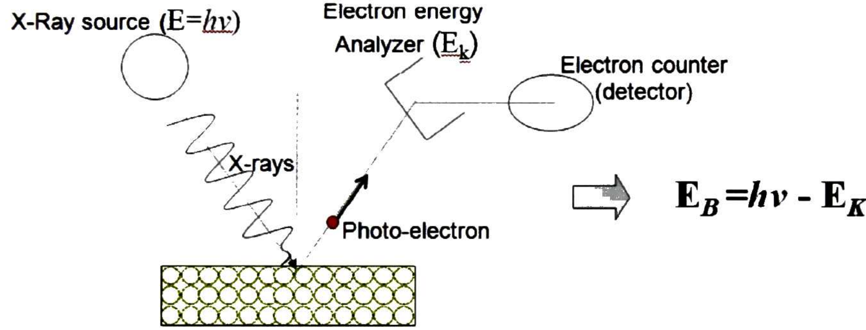

Figure 2.1 Schematic representation of photoemission process.

The kinetic energy (E_K) of the ejected photoelectron is an experimental quantity measured by the spectrometer, but this is dependent on the photon energy of the X-rays employed and is therefore not an intrinsic material property. The binding energy of the electron (E_B) is the parameter which identifies the electron specifically, both in terms of its parent element and atomic energy level. The relation between the parameters involved in the XPS experiment is:

Equation 2.1 $E_K = hv - E_B - \Phi$

Where $h\nu$ is the photon energy, E_K is the kinetic energy of the electron, and Φ is the spectrometer work function. $h\nu$ E_K and Φ are three quantities are known or measurable, it is simple matter to calculate the binding energy of the electron. AlK_α (1486.6 eV) and MgK_α (1253.6 eV) are the most used incident X-rays in the case of XPS. What makes XPS and attractive surface science tool is that photons have limited penetrating power in a solid to the order of 1-10 micrometers, and the escape depth of the emitted electrons is limited to $\approx$ 50Å.

Binding energies are expressed relative to a reference level. In gas phase photoemission, binding energies are measured from the vacuum level. For the study of the solids, the Fermi level is used as a reference. In the case of solid specimens, an electrical connection is made to the spectrometer in an attempt to minimize charging effects and maintain a well-defined and fixed potential during photoemission. For the simplest possible case of a metallic specimen in a metallic spectrometer, the energy levels and kinetic energies which result are shown in Figure 2.2.

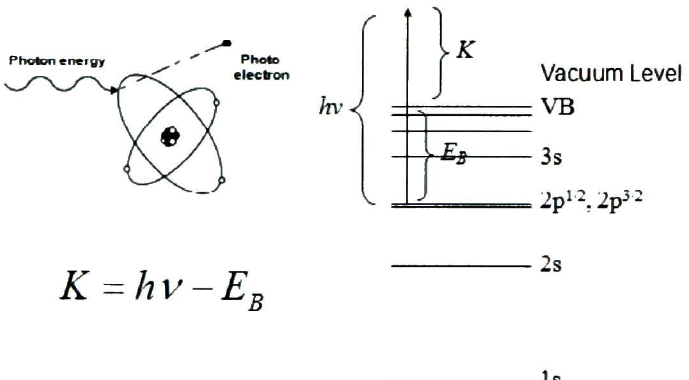

Figure 2.2 Energy level for binding energy for metallic samples.

Thermodynamic equilibrium between specimen and spectrometer requires that their electron chemical potentials or Fermi levels be equal. In a metal the absolute zero (T= 0 K), the Fermi level E_F has the interpretation as being the highest occupied level, as indicated in the figure; this interpretation of E_F is also a very good

approximation for metals at normal experimental temperatures. For semiconductors and insulators, however, it is not so simple to locate the Fermi level, which lies somewhere between the filled valence bands and the empty conduction bands. The work function Φ for a solid is defined to be the energy separation between the vacuum level and the Fermi level. When connected as shown in Figure 2.2, the respective vacuum levels for specimen and spectrometer need to be equal, however, so that in passing from the surface of the specimen into the spectrometer, the electron will feel a potential equal to the difference between the spectrometer work function Φ_{spec} and the sample work function Φ_s. ($\Phi_s - \Phi_{spec}$).

2.4 Electron spectrometer Design

The modules required for electron spectroscopy analysis are: a source of the primary beam (X-ray or electrons), an electron energy analyzer and detection system, all contained in a vacuum chamber; and a data system like an essential part of the system.

2.4.1 Vacuum system

The spectrometers are based on vacuum systems designed to operate in the ultra-high vacuum (UHV) range of 10^{-8} to 10^{-10} mbar, the reasons are the next:[1]

The analytical signal of low-energy electrons is easily scattered by the residual gas molecule and, unless their concentration is kept to an acceptable level, the total spectral intensity will decrease, while the noise present within spectrum will increase.

More importantly, the UHV environment is necessary because of the surface sensitivity of the technique themselves. At 10^{-6} mbar, it is possible for a monolayer of gas to be adsorbed onto a solid surface in about 1 s. This time period is short compared with that required for a typical spectral acquisition, clearly establishing the need for UHV environment during analysis. The conditions for UHV are typically obtained using ion pumps and titanium sublimation pumps (TSP).

2.4.2 Sample

Samples for XPS must be stable within the UHV chamber. Very porous material can cause problems as well as those which either have a high vapor pressure (~10^{-7} mbar) or have a component which has a high vapor pressure.

The mounting of conducting samples is best achieved with clips or bolt-down assemblies. For analysis, the sample is held in a high resolution manipulator with x, y, and z translations, and tilt and rotation about the z-axis (azimuthal rotation). For Angle Resolved XPS (ARXPS), the amount of backlash in the rotary drive must be small and the scale should be graduated in increments of 1° for manual operation.

Once mounted for analysis, heating or cooling of the specimen can be carried out *in vacuo.* Cooling is generally restricted to liquid nitrogen temperatures although liquid helium stages are available. Heating may be achieved by direct (contact) heating using a small resistance heater or by electron bombardment for higher temperatures. Such heating and cooling will either be a preliminary to analysis or carried out during the analysis itself. Heating in particular will often be carried out in a preparation chamber because of the possibility of severe out gassing encountered ah higher temperatures.[1]

2.4.3 Analyzers

There are two types of electron energy analyzer in general use for XPS, the cylindrical mirror analyzer (CMA) and the hemispherical sector analyzer (HSA). The CMA is used when it is not important that the highest resolution is achieved and when it is necessary to collect electrons from only a small area (<1nm diameter).

2.4.3.1 Cylindrical mirror analyzer (CMA)

The CMA consists of two concentric cylinders, the inner is held at earth potential while the outer is ramped at a negative potential, and then the deflection is caused by the potential difference. An electron gun is often mounted coaxially within the analyzer. A proportion of the Auger electrons emitted will pass through the defining aperture in the cylinder, electrons of the desired energy will pass through the detector aperture and be re-focused at the electron detector. Thus, an energy spectrum –the

direct energy spectrum– can be built up by merely scanning the potential on the outer cylinder to produce a spectrum of intensity (in counts per second) versus electron kinetic energy. This spectrum will contain not only Auger electrons but all other emitted electrons, the Auger peaks being superimposed, as weak features, on an intense background.

2.4.3.2 Hemispherical sector analyzer (HSA)

Consists of a pair of concentric hemispherical electrodes between which there is a gap for the electrons to pass. Between the sample and the analyzer there is usually a lens, or a series of lenses. The HSA is typically operated in one of two modes: constant analyzer energy (CAE), sometimes known as fixed analyzer transmission (FAT), and constant retard ratio (CRR), also known as fixed retard ratio (FRR). In the CAE mode the electrons are accelerated or retarded to some user defined energy which is the energy the electrons posses as they pass through the analyzer (the pass energy).

2.5 Spectra Characteristics

The survey spectrum is a first wide scan recording for the sample characterization. It allows to identify the chemical components in the sample and to define acquisition windows, the interest lines are recorded after with high resolution.

2.5.1 Core level

The XPS lines associated with core levels may have variable intensities and widths, which, except for the *s* level, are doublets. Photoelectrons, which originate from core-levels, give rise to the most intensive lines in the XPS spectra. The position of the core level lines is like a fingerprint for each element and thus the chemical identification of the components in the investigated specimen can be easily performed. Generally two or more elements will be detected on the surface. The relative intensities of their lines is governed by: occupancy of the sub–shell, stoichiometry, atomic cross-section σ. The values of σ can be derived from X-ray mass absorption coefficients or can be directly calculated[3]. Since the occupancy of the atomic sub-shells is known, XPS can be used as a non-destructive chemical

analysis tool. The width of the peak is defined as the full width at half maximum intensity (FWHM). This is a sum of three distinct contributions[4]: the natural inherent with of the core-level γ_n, the width of the photon source γ_p and the analyzer resolution γ_a . Thus the overall FWHM will be given by:

Equation 2.2 $$\gamma = \sqrt{\gamma_n^2 + \gamma_p^2 + \gamma_a^2}$$

The firs contribution is dictated by the uncertainty principle $\Delta E \Delta t \geq \hbar$ by the core-hole life time τ .

Equation 2.3 $$\gamma_n = \frac{h}{\tau}$$

Where h is the Planck constant. The lifetimes depend on the relaxation process which follows the photoemission. The narrowest core-levels have lifetimes in the range 10^{-14} -10^{-15} a whilst the broader have lifetimes close or slightly less than 10^{-15} s.

2.6 Components of an XPS system

The main components of an XPS system include: a source of X-rays, an ultra-high vacuum (UHV) stainless steel chamber with UHV pumps, an electron collection lens, an electron energy analyzer, mu-metal magnetic field shielding, an electron detector system, a moderate vacuum sample introduction chamber, sample mounts, a sample stage and a set of stage manipulators.

Monochromatic aluminum K-alpha X-rays are normally produced by diffracting and focusing a beam of non-monochromatic X-rays off of a thin disc of natural, crystalline quartz with a <1010> lattice. The resulting wavelength is 8.3386 angstroms (0.83386 nm) which corresponds to a photon energy of 1486.7 eV. The energy width of the monochromated X-rays is 0.16 eV, but the common electron energy analyzer (spectrometer) produces an ultimate energy resolution on the order of 0.25 eV which, in effect, is the ultimate energy resolution of most commercial systems. When working under everyday conditions, the typical high energy resolution (FWHM) is usually 0.4-0.6 eV.

Non-monochromatic magnesium X-rays have a wavelength of 9.89 angstroms (0.989 nm) which corresponds to a photon energy of 1253 eV. The energy width of the non-monochromated X-ray is roughly 0.70 eV, which, in effect is the ultimate energy resolution of a system using non-monochromatic X-rays. Non-monochromatic X-ray sources do not diffract out the other nearby X-ray energies and also allow the full range of high energy Bremsstrahlung X-rays (1–12 keV) to reach the surface. The typical ultimate high energy resolution (FWHM) for this source is 0.9–1.0 eV, which includes with the spectrometer-induced broadening, pass-energy settings and the peak-width of the non-monochromatic magnesium X-ray source.

2.6.1 X-Ray source

X-rays are generated by bombarding an anode material with high-energy electrons. The efficiency of X-rays emission from anode is determined by electron energy, relative to the X-ray photon energy.

2.6.1.1 Anode of X-ray source

A convenient source of characteristic X-rays is provided by electron bombardment of Mg or Al targets.

In the case of the X-ray source used in this thesis, the AlKα (1486.6 eV) photon flux from an Al anode increases by a factor of more than five if the electron energy is increased from 4 keV to 10 keV. At a given energy, the photon flux from an X-ray anode is proportional to the electron current striking the anode. The maximum anode current is determined by the efficiency with which the heat, generated at the anode, can be dissipated. For this reason, X-ray anodes are usually water-cooled.

The choice of anode material for XPS determines the energy of X-ray transition generated. It must be of high enough photon energy to excite an intense photoelectron peak from all elements of the periodic table (with the exception of very lightest); it must also posses a natural X-ray line width that will not broaden the resultant spectrum excessively.

The main reasons for choice higher-energy anodes are[1]:

- Energy levels not available in conventional XPS become accessible in AlKα radiation the Mg 1s electron is the highest K electron attainable, in SiKα this is extended to the Al 1s electron, in ZrLα the Si 1s electron, AgLα the Cl 1s electron and in TiKα the Ca 1s electron.
- The use of higher-energy photon sources increases the kinetic energy of the ejected photoelectrons available when compared with conventional XPS, higher-energy XPS provides a non-destructive means of increasing the analysis depth. It is therefore possible to build up a depth profile of a specimen merely by changing the X-ray source an monitoring the apparent change in composition.

2.6.1.2 X- ray monochromators

X-ray monochromators usually make use of crystal diffraction to energy select the beam. The purpose of the monochromator is to produce a narrow X-ray line by using diffraction in a crystal lattice, process.

The basis of x-ray diffraction is the Bragg equation which describes the condition for constructive interference for X-rays scattering from atomic planes of a crystal (Figure 2.3). The condition for constructive interference is:

Equation 2.4 $$n\lambda = 2d\sin\theta$$

Where λ is the wavelength of the incident radiation, n is the diffraction order, d is the crystal lattice spacing, and θ is the Bragg angle (angle of diffraction). The Bragg law requires that θ and λ be matched for diffraction. The condition may be satisfied by varying λ, or varying the orientation of a single crystal. In thin films the distribution of crystallite orientations is nearly continuous. Diffraction occurs from crystallites which happen to be oriented at the angle to satisfy the Bragg condition.[2]

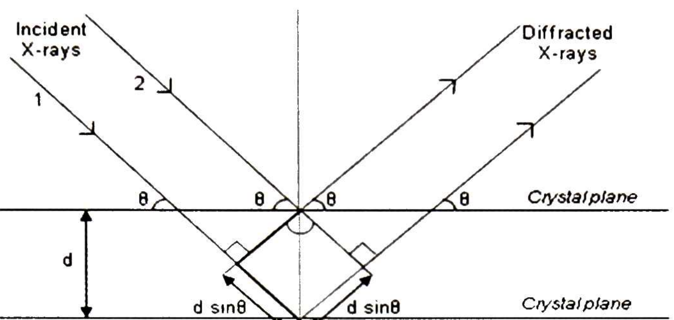

Figure 2.3 Diffraction of X-rays at a quarts crystal.

The commercially available X-ray monochromators used for XPS employ a quartz crystal (usually the$(10\bar{1}0)$ crystal face) as the diffraction lattice. Usually, the monochromator on an XPS instrument is used for AlKα radiation, the spacing in the quartz crystal lattice means that first-order reflection occurs at a convenient angle. Quartz is a convenient material because it is relatively inert, compatible with UHV conditions, it can be bent and/or ground into the correct shape ant its lattice spacing provides a convenient diffraction angle for AlKα radiation.

The most important reasons for choose to use an X-ray monochromator in an XPS spectrometer, are as follows[1]:

- The monochromated radiation allows the reduction in X-ray line width. Narrower X-ray line width results in narrower XPS peaks and consequently better chemical state information.
- Unwanted portions of the X-ray spectrum, i.e. satellites peaks and the Bremsstrahlung continuum are also removed.
- For maximum sensitivity, a twin anode X-ray source is usually positioned as close to the sample as possible. The sample is therefore exposed to the radiant heat from the source region which could damage or alter the surface of delicate sample. When a monochromator is used, this heat source is remote from the sample and thermally induced damage is avoided.

- It is possible to focus X-rays into a small spot using the monochromator. This means that small area XPS can be conducted with high sensitivity.
- Use a focusing monochromator means that only the area of the specimen being analyzed is exposed to X-rays. Thus, a number of samples may be loaded into the spectrometer without the risk of X-rays damaging samples while they await analysis. Similarly, multipoint analysis can be performed on the same delicate sample.
- The quartz crystal is curved in such a way it focuses the X-ray beam as well as causing it to be diffracted. By this means, the size of the sample is approximately equal to that of the electron spot on the anode. Thus, by varying the focusing of the electron source, the analyst can vary the analysis area.

2.7 Angle Resolved XPS

Angle Resolved XPS is a procedure in which X-ray photoelectron intensities are measured as a function of the angle of emission.

The finite mean free path of electrons within a solids means that the information depth in XPS analysis is of the order of a few nanometers. This is only true if the electrons are detected at a direction normal to the sample surface. If electrons are detected at some angle to the normal, the information depth is reduced by an amount equal to the cosine of the angle between the surface normal and the analysis direction; it is the basis for this analysis technique.

ARXPS is a powerful analysis technique, its presents some advantages:

- Can be applied to films which are too thin to be analyzed by conventional depth profiling techniques or those that are irretrievably damaged by such methods.
- It is a non-destructive technique which can provide chemical state information, unlike method based upon sputtering.

2.8 Data Analysis

The aim of spectral analysis in XPS is to determine the location, intensities, and in certain cases also shapes of the various peaks observed, many of which are not clearly resolved from one another.

In Figure 2.4 is squematically represented how is determined the depth profile compositional of the multilayers formed in the samples. The XPS data acquired is fitted and modeled making use of information available for each core level and finally the stoichiometry and thickness of the multilayer formed is determined.

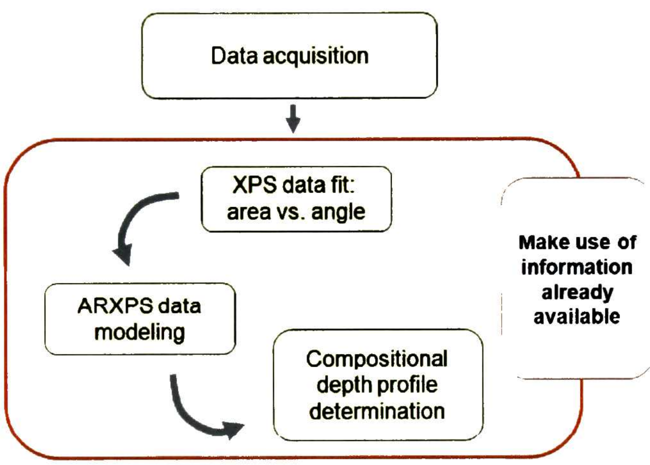

Figure 2.4 Compositional depth profiling in ARXPS

The stoichiometry and thickness of the multilayers formed was studied through a carefully analysis of Angle Resolved XPS data. It was possible to determine by an appropriate selfconsistent analysis using like tools AAnalyzer® and XPS Geometry® software. AAnalyzer® and XPS Geometry® are software developed by Dr. Alberto Herrera Gómez and Dr. F. Servando Aguirre Tostado.

There are four steps which ones are the key stages of ARXPS analysis to get quantitative in depth profile determination in ultra thin films, and they are the next:

1. Data Acquisition
2. Data Fitting

3. Modeling of the angular dependence

4. Characterization of instrument

2.8.1 Data Fitting (AAnalyzer®)

AAnalyzer® is a powerful software for photoemission and infrared data analysis. Its graphic user interface (GUI) makes more approachable the fitting task. This software manages data files simultaneously, and allows for parameter correlation. This is extremely helpful when physical parameters are extracted from a set of data. AAnalyzer® displays the evolution of the fitting and also plots the value of each fitting parameter for the various data files.[5]

This software allows an adequate data deconvolution and fitting. It is possible to perform, at the same time, an analysis of all data files for a specific core level. In this way areas, energies and widths of each peaks deconvoluted are obtained.

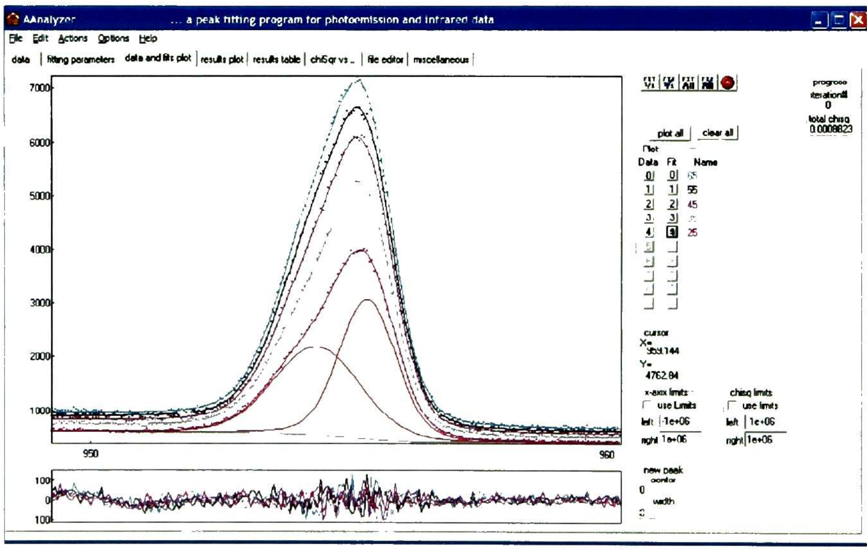

Figure 2.5 Fitting and deconvolution using AAnalyzer®.

The conventional data fitting consists of the following:

- The "best parameters" of the peaks are found for a spectrum taken at one of the angles. There is not a unique way to accomplish this, and some initial guessing is necessary.

- The values are then constrained in a small range and used to fit the rest of the data.
- By inspecting the quality of the fits, the parameters of the first file are constrained to a value that would provide a better fit for the rest of the files.
- The process is taken into a loop and repeated until a "good" fit is found for all files.

It is important to be carefully about the stability of the sample during the measurements and, in order to avoid some possible error in the data acquisition. Finally, is also important to make sure that the sample alignment is the appropriately performed.

2.8.2 Modeling of the Angle Resolved XPS Data (XPSGeometry®)

The extraction of an elemental or a chemical depth profile from ARXPS data is not a trivial task. Although the mathematical model is not complex the implementation of the model is. It requires a powerful algorithm to properly account for every factor that affects the XPS intensity dependence on the angle. This is necessary to separate the portion of the XPS intensity that only depends on the chemical depth profile characteristics. XPSGeometry® is an unique ARXPS data analysis software that performs a numerical integration of the photoemission signal dependent on the angle, atomic and geometrical parameters.[6] Through this software is possible to obtain a detailed depth profile modeling with a minimum of parameters. The analysis is based on a "square box" depth profile model which extracts only three parameters (atomic concentration, shallow end and deep end) from the angular dependence of the XPS.

The ARXPS data modeling with a square-box depth profile is illustrated in Figure 2.6 for a deep layer containing a chemical specie "S". The buried layer has some more layers on top that will attenuate its signal as explained below.

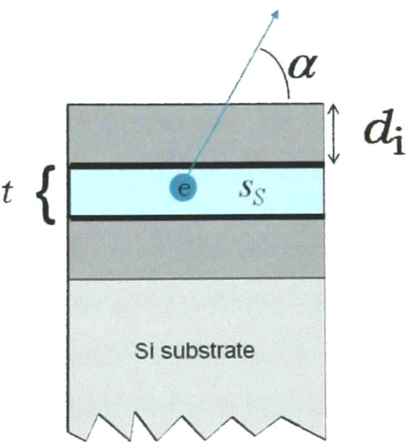

Figure 2.6 Illustration of the used square box depth profile model of a buried layer with a chemical specie "*S*" at a depth d_i with a thickness *t* and for a take-off angle α.

The structural model shown in Figure 2.6 takes into account that the layer of interest has an element "S" uniformly distributed across the layer and has several layers on top of it with thicknesses d_i's. According to this model the XPS intensity is given by the next equation of the buried layer is[7]:

Equation 2.5
$$I_{S1}(\alpha) = G(\alpha)\, X\, A\, \sigma_S\, s_S \frac{1-\exp\left(-\dfrac{d_S}{\lambda_S \sin\alpha}\right)}{1-\exp\left(-\dfrac{a_S}{\lambda_S \sin\alpha}\right)} \prod_{i}^{\text{layers above S}} \exp\left(-\frac{d_i}{\lambda_{S,i} \sin\alpha}\right)$$

Where a_S, d_S, S_S, σ_S and, λ_S are the atomic plane spacing, thickness, atomic concentration, photoionization cross section and EAL of the layer "*S*", respectively. d_i is the thickness of the overlayer *i* and $\lambda_{S,i}$ is the EAL of the "*S*" signal by the overlayer *i*. *X* and *A* are the intensity of the x-ray excitation source and the spectrometer efficiency, respectively. And at last but not least is *G(α)* a geometric factor that accounts for the intersection of spectrometer analyzing region with the x-ray source illumination area for a given geometry (in its simplest form it just depends on *α*). XPSGeometry® performs a numerical integration of every point in the sample according to Equation 2.5. The spatial integration limits where carefully chosen in the

calculations to provide better accuracy in the modeling of the ARSXP data. Figure 2.7 shows a qualitative exemplification of the XPS peak area dependence of a specie contained in a thin layer which is either on the surface or deeper in the bulk.

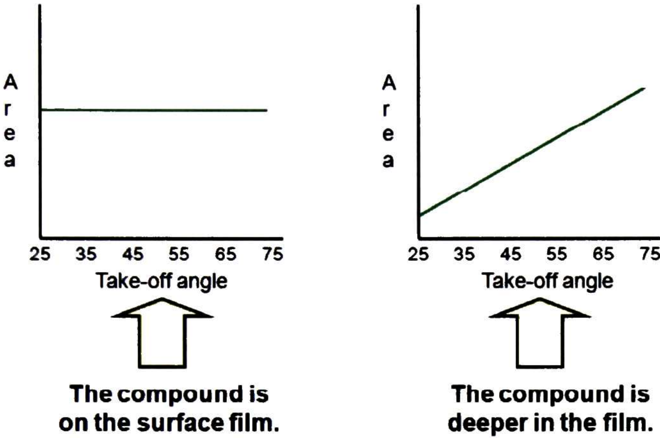

Figure 2.7 Qualitative illustration of peak area dependence in Angle Resolved XPS for a chemical specie in a thin layer that is on the surface (left) or buried (right).

2.8.3 Parameters Employed in the Calculations

The theoretical prediction of the angular dependence implied the previous knowledge of the geometrical parameters of the XPS tool. These parameters will accurately determine the *G(α)* factor expressed in Equation 2.5. The parameters of the XPS tool employed in this study are shown in Table 2.1.

Table 2.1 Set of parameters obtained in the characterization of the XPS equipment. A previous work very complete about it was carried out.

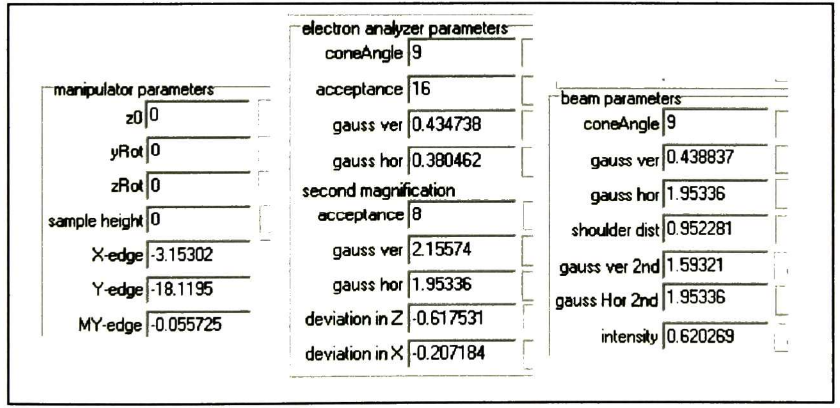

manipulator parameters	
z0	0
yRot	0
zRot	0
sample height	0
X-edge	-3.15302
Y-edge	-18.1195
MY-edge	-0.055725

electron analyzer parameters	
coneAngle	9
acceptance	16
gauss ver	0.434738
gauss hor	0.380462
second magnification	
acceptance	8
gauss ver	2.15574
gauss hor	1.95336
deviation in Z	-0.617531
deviation in X	-0.207184

beam parameters	
coneAngle	9
gauss ver	0.438837
gauss hor	1.95336
shoulder dist	0.952281
gauss ver 2nd	1.59321
gauss Hor 2nd	1.95336
intensity	0.620269

The calculations also required the previous knowledge of:

- the photoemission cross section for each core level employed (see Table 2.2), parameters that were obtained from the literature, and
- the effective attenuation length for the different materials (see Table 2.3) constituting the film.

Table 2.2 The kinetic energy[8] and cross section[9] of the photoelectrons employed in the calculations were found in the literature.

element	kinetic energy	PE cross section
Si2p	1387	0.011
Si2p	1387	0.011
Hf4f	1469	0.1108
O1s	955	0.04

Table 2.3 Effective Attenuation Length values were calculated using the NIST Electron Effective Attenuation Length Database. Lattice constant of the layers and bulk were calculated too.

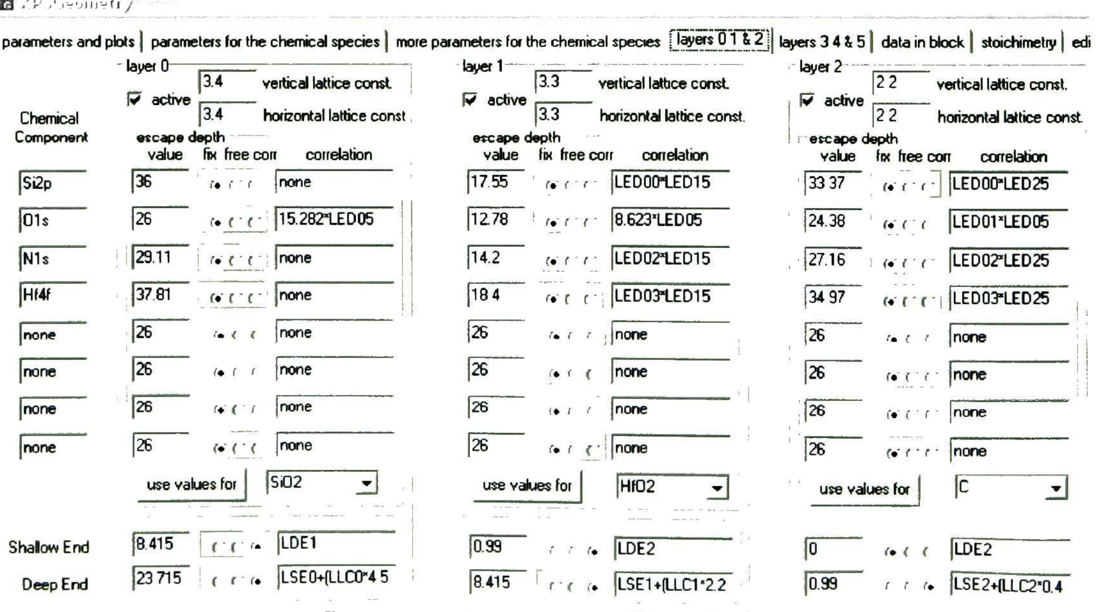

parameters and plots | parameters for the chemical species | more parameters for the chemical species | layers 0 1 & 2 | layers 3 4 & 5 | data in block | stoichimetry | edi

	layer 0		layer 1		layer 2	
active	✓		✓		✓	
vertical lattice const.	3.4		3.3		2.2	
horizontal lattice const.	3.4		3.3		2.2	
Chemical Component	escape depth value	correlation	escape depth value	correlation	escape depth value	correlation
Si2p	36	none	17.55	LED00*LED15	33.37	LED00*LED25
O1s	26	15.282*LED05	12.78	8.623*LED05	24.38	LED01*LED05
N1s	29.11	none	14.2	LED02*LED15	27.16	LED02*LED25
Hf4f	37.81	none	18.4	LED03*LED15	34.97	LED03*LED25
none	26	none	26	none	26	none
none	26	none	26	none	26	none
none	26	none	26	none	26	none
none	26	none	26	none	26	none
use values for	SiO2		HfO2		C	
Shallow End	8.415	LDE1	0.99	LDE2	0	LDE2
Deep End	23.715	LSE0+(LLC0*4.5	8.415	LSE1+(LLC1*2.2	0.99	LSE2+(LLC2*0.4

The Effective Attenuation Length of Table 2.3 was obtained from the NIST Electron Effective Attenuation Length Database employing the parameters shown in Table 2.4 and Table 2.5. These two set of parameters were also obtained from the same NIST database.

Table 2.4 Core level parameters employed in the calculation of the effective attenuation lengths with the software provided by NIST.[10]

Peak	Assimetry parameter (β)
Si2p	1.03
O1s	2
Hf4f	1.06

Table 2.5 Layer parameters employed in the calculation of the effective attenuation lengths with the software provided by NIST.[10]

Material	Gap (eV)	Valence electrons	Density (g/cm^3)
Si	1.1	4	2.3
SiO_2	9	16	2.2
HfO_2	6	16	9.8

The ARXPS data is shown in Section 4.7 and the respective quantitative analysis and fitting are shown in Chapter 5.

References (Chapter 2)

1 An Introduction to Surface Analysis by XPS and AES. John F. Watts and John Wolstenholme. John Wiley & Sons, Ltd (2003).

2 Fundamentals of Surface And Thin Film Analysis. Leonard C.Feldman and James W. Mayer. North Holland Ed. (1986).

3 V.I. Nefedof, N.P. Sergushin, I.M. Band, and M.B. Trazhaskovskaya. Relative intensities in x-ray photoelectron spectra. Journal of Electron Spectroscopy and Related Phenomena.

4 D. Briggs and J. C. Riviere. Spectral Interpretation.

5 Alberto Herrera-Gómez, “AAnalyzer: Un Programa de Análisis para Espectros de Infrarrojo y de Fotoemisión”. Reporte Interno, Julio de 1998 LIM-CINVESTAV (Registro S.E.P. Número 03-1999-051710412300, diciembre de 1999, México).

6 A. Herrera-Gomez “XPSGeometry: A program for depth profile analysis for ARXPS” (2006).

7 A. Herrera-Gomez, F.S. Aguirre-Tostado, G.K. Pant, M. A. Quevedo-Lopez, Paul D. Kirsch, J. Wang, M. Kim, B.E. Gnade, and R.M. Wallace "Thermal stability of nitrogen in nitrided $HfSiO_2/SiO_2/Si(001)$ ultrathin films." (To be published).

8 X-ray Data Booklet edited by A. Thompson and D. Vaughan (Lawrence Berkeley Labs, Berkeley, 2001). See http://xdb.lbl.gov/.

9 J. J. Yeh and I. Lindau, At. Data Nucl. Data Tables 32, 1–155 (1985).

10 C. D. Wagner, Alexander V. Naumkin, A. Kraut-Vass, J. W. Allison, C. J. Powell, and J.R. Rumble Jr., NIST X-ray Photoelectron Spectroscopy Database, NIST Standard Reference Database 20, Version 3.4 (Web Version). See: http://srdata.nist.gov/xps/index.htm.

Chapter 3

Experimental Techniques

A detailed explanation of the experimental techniques used for sample preparation and characterization is presented in this chapter.

Chapter 3. Experimental Techniques

3.1 Aqueous Chemical Wafers Cleaning Process

In the fabrication of semiconductor microelectronic devices is extremely important to clean the substrate surface. This is because device performance, reliability, and yield of silicon integrated circuits are critically affected by the presence of contaminants and particles on the silicon wafer or device surface.

The basic requirement for the cleaning processes is the removal of contamination. Aqueous chemistries involve a variety of solutions which can be made by dissolving a gas, liquid, or solid in water. Aqueous cleaning solutions are currently the most widely used due to their many advantages over alternative processes.[1]

3.2 RCA Cleaning

The most common cleaning procedure for silicon wafers is the RCA standard clean (SC) method, divided in two steps typically known as SC1 and SC2. It is an aqueous mixture of unstabilized hydrogen peroxide with ammonia and hydrochloric acid. This is the standard cleaning process used in Si MOSFET processing developed before 1970 by RCA Corporation. The original RCA clean consisted of two cleaning solutions:[1]

1. NH_4OH (29w/w%) + H_2O_2 (30%) + DI H_2O at 70 - 80°C

2. HCl (37w/w%) + H_2O_2 (30%) + DI H_2O at 75 - 80°C

The purpose of the first step, known as Standard Clean 1 or SC-1, is to oxidize surface organic films and remove some metal ions. The second step, known as Standard Clean 2 or SC-2, is to remove alkali cations and other cations like Al^{+3}, Fe^{+3} and Mg^{+2}. The solutions were mixed typically in the ratio 1:1:5.[1] Each of these steps is followed by a deionized (DI) water rinse.

The sequence of chemical solutions used to clean a wafer depends upon the contaminants present and the requirements of the clean. A possible sequence of the chemistries used in a common modified RCA, consists of the following steps[1]:

1. Organic removal
2. Native oxide removal
3. Particle removal with simultaneous oxide regrowth
4. Metal removal

3.2.1 Organic Removal

This is the first step in cleaning, because of the presence of organic films on wafer surfaces can render the surface hydrophobic and prevent other cleaning solutions from reaching the surface. There are two solutions commonly used for removing organic films. If heavy organic contamination like photoresist is present, mixtures of H_2SO_4, and H_2O_2 at 80°C are often used.[2] Light organics can be removed at 80°C using the NH_4OH/H_2O chemistries described above.[3] If very heavy contamination is present the H_2SO_4/H_2O_2 solution followed by the NH_4OH/H_2O_2, solution may be effective.[1]

3.2.2 Native Oxide Removal

This step is included because a thin layer of oxide is always present on a silicon surface and inorganic contaminants are often trapped in this layer. When the oxide is removed the contaminants are also removed, resulting in a surface with very low metallic contamination.[4] Oxide can be removed using either dilute solutions of HF or buffered oxide etch (BOE). BOEs are commonly used instead of dilute HF because they provide a more stable etch rate. However, the formulation of BOEs is not straightforward. Surfactants are often added to improve wetting of the wafer surface since silicon becomes hydrophobic when the oxide is removed. The surfactants tend to make the solution foam, so defoamers are added. Optimization of this multicomponent solution is a very complex task.[5]

HF solutions need to have extremely low metal levels to be effective. Metals like copper and gold, which have a lower electronegativity than silicon, can plate onto the wafer surface.[6,7] The solutions should also be free of organics, as well as all subsequent cleaning or rinsing solutions used before a clean oxide is grown,

because the hydrophobic silicon surface is very prone to hydrocarbon adsorption.[8] In addition, the hydrophobic surface following this clean is very susceptible to particulate contamination[9,10] that may result when it is exposed to gas-liquid interfaces.[8] Hence, the methods used to rinse and dry the wafer following this step are critical in controlling particle contamination.[11]

3.2.3 Particle Removal with Simultaneous Oxide Regrowth

Because the oxide removal process tends to add particles to the wafer surface, it is often followed by an NH_4OH/H_2O_2 step. This step is effective in both removing particles and growing a thin oxide film. The oxide "passivates" the surface by making it hydrophilic and less susceptible to organic and particulate contamination.[12,13] Particles are presumably removed by slowly etching the surface of the silicon from under the particles. The etch rate is a function of the type of oxide present and is in the range of 0.09-0.4 nm/min at 80°C when the ratio of $NH_4OH:H_2O_2:H_2O$ is 1:1:5.[14] This step is extremely effective in removing particles when it is combined with ultrasonic cleaning.[15] One disadvantage of using the NH_4OH/H_2O_2 solution to grow an oxide is that some metals are insoluble in this highly basic solution and, if present, have a high tendency to precipitate onto the wafer surface. Aluminum is an example of a metal of this type which, when present in sub-ppm concentrations, can cause a substantial shift in the flat band voltage of a dual dielectric.[16] Also, because aluminum is one of the few metals which does not cause H_2O_2 to decompose, the equipment used to make and store H_2O_2, was historically made of aluminum. The resulting H_2O_2, contained significant levels of aluminum.[17] Recent advances in the technology of making H_2O_2 have virtually eliminated this source of contamination.[18]

3.2.4 Metal Removal

Metal removal is usually accomplished using the HCl/H_2O_2 solution described above. This solution effectively removes metals and prevents them from plating back onto the surface by complex formation. It has been shown to be effective for removing cobalt, copper, iron, lead, magnesium, nickel and sodium as well as aluminum precipitated from the NH_4OH/H_2O_2 solutions[19] and other metals.

3.3 Rinsing and Drying

The last steps in the wafer cleaning process are rinsing and drying. Both are critical because clean wafers become recontaminated easily if not processed properly. Rinsing after wet cleaning is done with flowing high purity and ultrafiltered high-resistivity deionized (DI) water, usually at room temperature.[20] Rinsing in DI water is important at all stages of the preparation, as it removes species that are weakly bound to the surface (physisorbed or hydrogen bonded) and can even etch the silicon surface.[21] In fact, wafer drying may be the most important step for ensuring that a cleaning process is successful in eliminating contamination. The drying process must remove water from the surface before it can evaporate, leaving residue behind.[22,23] There are three basic drying mechanisms: physical separation as in centrifugal drying, solvent displacement of DI water followed by solvent removal as in vapor drying, and evaporation as in hot water drying techniques.[1]

Centrifugal or spin dryers are very common in the semiconductor industry. The centrifugal force resulting from spinning wafers at high speed eliminates the major portion of water from the wafer surface. The thin layer left behind evaporates. Because the evaporating water layer is very thin, deposition of residuals is minimal.[24]

3.4 Atomic Layer Deposition (ALD)

ALD was developed under the name "Atomic Layer Epitaxy (ALE)" in Finland by Suntola and co-workers[25], in the 1970's. ALD is a chemical vapor deposition (CVD) technique suitable for manufacturing inorganic material layers with thickness down to a fraction of a monolayer.[26,27] ALD has the capability to coat extremely complex shapes with a conformal material layer of high quality, a capability unique among thin-film deposition techniques.[26,27,28]

ALD can be defined as a film deposition technique that is based on the sequential use of self-terminating gas–solid reactions.[25] Figure 3.1 illustrates a typical cycle of an ALD process using AX_n and BY_n precursors to obtain the compound AB (e.g. a dielectric metal oxide film) through the following chemical reaction[29]:

$$AX_n + BY_n \rightarrow AB + nXY$$

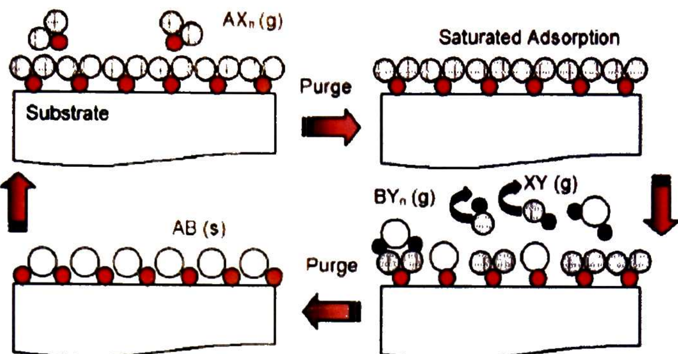

Figure 3.1 Typical sequence for one unit cycle of the ALD process to obtain AB films by using AX_n and BX_n precursors.[29]

The growth of material layers by ALD consists of repeating the following characteristic four steps[25]:

5. 1. A self-terminating reaction of the first reactant (Reactant A).
6. 2. A purge or evacuation to remove the nonreacted reactants and the gaseous reaction by-products.
7. 3. A self-terminating reaction of the second reactant (Reactant B) -or another treatment to activate the surface again for the reaction of the first reactant.
8. 4. A purge or evacuation.

Steps 1–4 constitute a reaction cycle. Steps 1 and 3 are sometimes referred to as half reactions of an ALD reaction cycle.[30,25]

Each reaction cycle adds a given amount of material to the surface, referred to as the *growth per cycle* (GPC). To grow a material layer, reaction cycles are repeated until the desired amount of material has been deposited.[25] Before starting the ALD process, the surface is stabilized to a known, controlled state, for example, by a heat treatment. The use of self-terminating reactions leads to the conclusion that ALD is a surface-controlled process, where process parameters other than the reactants, substrate, and temperature have little or no influence. Because of the surface control, ALD-grown films are extremely conformal and uniform in thickness.[25]

3.4.1 Requirements for Self-terminating Reactions

ALD can be defined to be based on the sequential use of self-terminating gas–solid reactions. In the reaction of a gaseous compound reactant with the solid surface, atoms which are to be included in the ALD-grown film are adsorbed on the surface. Simultaneously, atoms which are not to be included in the film may be removed as gaseous reaction by products.[25]

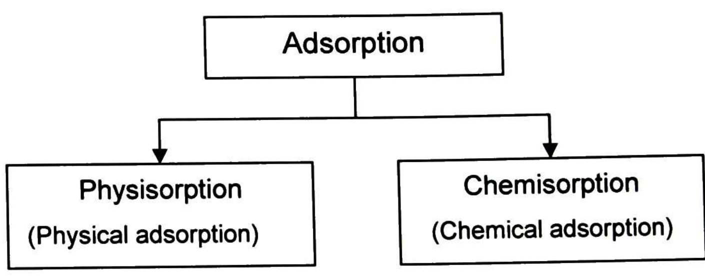

Figure 3.2 Adsorption classes.

As shown in Figure 3.2 adsorption can be divided into two general classes on the basis of the strength of interaction between the adsorbing molecule ("adsorptive") and the solid surface ("adsorbent"): physisorption and chemisorption.

- *Physisorption* originates from weak interactions, where minimal changes typically occur in the structure of the adsorbing molecule. The interactions are not specific to the molecule– surface pair, and consequently, adsorption may occur in multilayers.[31]
- *Chemisorption*, in turn, involves the making and optionally breaking of chemical bonds. Because in chemisorption, chemical bonds are formed between the adsorbing molecule and the surface, the surface "accepts" only one layer, a monolayer, of the adsorbed species ("adsorbate").[31]

In relation with ALD, one must realize that a monolayer of the adsorbed species differs both from a monolayer of the reactant molecule, and from a monolayer of the ALD-grown material (Figure 3.3):

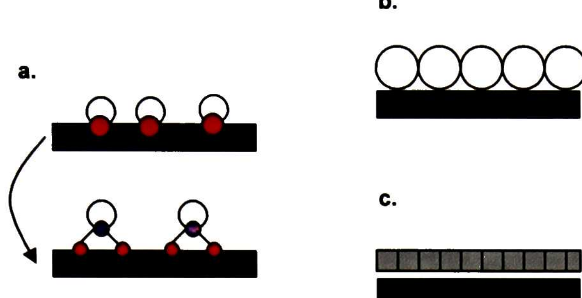

Figure 3.3 Three different types of monolayers relevant to ALD: a) a chemisorbed monolayer (the substrate before chemisorption indicated above, with reactive sites shown), b) a physisorbed monolayer, and c) a monolayer of the ALD-grown material.[25]

- Monolayer (capacity) for chemisorption is defined[31] as "the amount of adsorbate (adsorbed species) which is needed to occupy all adsorption sites as determined by the structure of the adsorbent (surface) and the chemical nature of the adsorptive (the reactant)".
- Monolayer (capacity) for physisorption is defined[31] as "the amount needed to cover the surface with a complete monolayer of molecules in a close-packed array".
- Monolayer for the ALD-grown material MZ_x can be defined as one plane of MZ_x units in a crystalline face of the bulk MZ_x material in the preferred orientation of growth.[25]

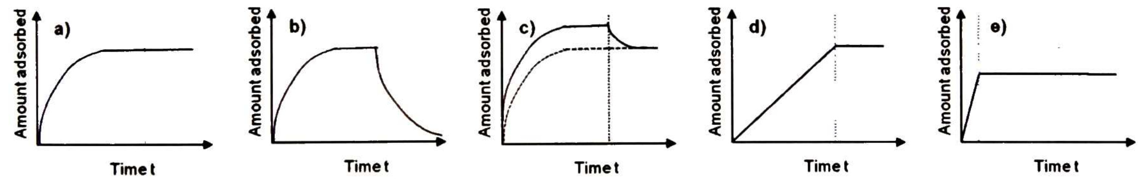

Figure 3.4 Examples of how the amount of material adsorbed can vary with time.[25]

Figure 3.4 shows the dependence between the amount of material adsorbed in gas-solid reactions on time in various ways. Both irreversible and reversible adsorption can be saturating in nature [Figure 3.4 (a) and (b), respectively]. For the adsorption to

be self-terminating, however, the adsorbed material may not desorb from the surface during the purge or evacuation. Consequently, in ALD, the type of adsorption is limited to irreversible adsorption (irreversible in the time scale of the experiment). Because physisorption is always reversible, whereas chemisorption can be reversible or irreversible, the requirement of irreversibility restricts the type of adsorption to chemisorption. In addition to irreversible adsorption, reversible adsorption may occur, but it does not contribute to ALD growth [(Figure 3.4 (c)]. Irreversible adsorption as such is not a sufficient requirement to achieve ALD growth, however, as irreversible adsorption can also be continuous and nonsaturating [Figure 3.4(d)]. Moreover, to take advantage of the self-terminating features, the irreversible, saturating reactions must be allowed to terminate, to go to completion [Figure 3.4(e)].[25]

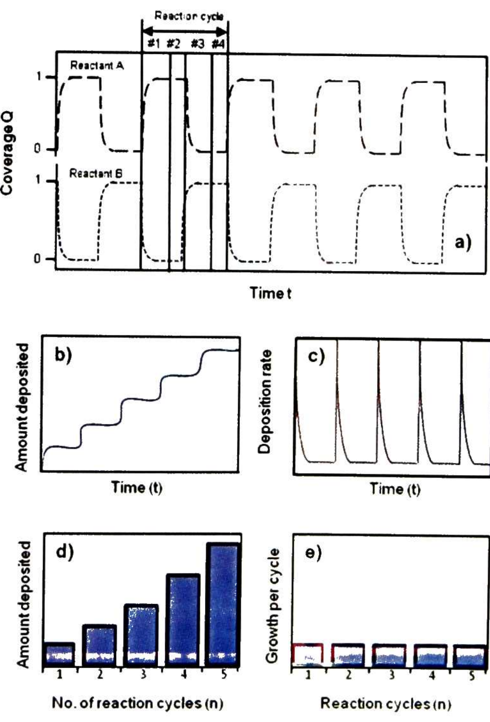

Figure 3.5 Schematic representation of five reaction cycles, assuming irreversible adsorption.[25]

Figure 3.5 (a) illustrates the chemisorption coverage as function of time for irreversible chemisorption. During the reaction of Reactant A (Step 1), typically a compound reactant MLn, the chemisorption coverage increases until it settles to one

when the reaction has terminated. During the following purge/evacuation (Step 2), the chemisorption coverage remains constant. The reaction of Reactant B (Step 3) causes the chemisorption coverage of the species adsorbed from Reactant A to decrease, ideally down to zero. Reactant B brings other types of adsorbed species on the surface, the coverage of which increases from zero to one during the reaction. During the following purge/evacuation (Step 4), the chemisorption coverages remain constant. During repeating reaction cycles of Steps 1–4, the chemisorption coverages therefore switch between zero and one [Figure 3.5 (a)].[25]

Time affects the chemisorption coverage in different way than it affects the total amount of material deposited. As illustrated in Figure 3.5(b), the amount of atoms deposited increases during step 1 of the reaction cycles. The deposition rate varies with time [Figure 3.5(c)], implying that the process is in a transient state. The amount of material deposited increases linearly with the number of reaction cycles [Figure 3.5 (d)] and the GPC is constant [Figure 3.5 (e)]. The number of reaction cycles is clearly a discrete variable, whereas time is continuous.[25]

3.4.2 Precursors

As in CVD, the ALD precursors should be highly reactive and contain surface termination groups that result in volatile by-products, but should additionally result in a self-limiting surface reaction mechanism. In some instances, an ALD process can utilize the same precursors as in a CVD process, but involve discrete alternating exposure to the precursors rather than simultaneous exposure.[33]

General requirements of reactants used in ALD are that they must be volatile (either at room temperature or at elevated temperatures), the reactants may not decompose thermally at the ALD processing temperatures, and the gas–solid reactions of the reactants have to fulfill the criterion of self-termination. Other properties of the different types of reactants may differ.[25]

The reactants used in ALD can be divided into two main groups[25]: inorganic and metalorganic.

- Metalorganic reactants can further be classified in those containing a direct metal–carbon bond, that is, organometallic reactants, and those containing no direct metal–carbon bond.
- Typically, of inorganic reactants, elements and halides have been used; of organometallic reactants, alkyls and cyclopentadienyls have been used; and of other metalorganic reactants, alkoxides, -diketonates, amides, and amidinates have been used in ALD experiments.

Additionally, oxygen (H_2O, H_2O_2, O_2, and O_3) and nitrogen (NH_3, N_2H_4, NH_xR_{3-x}, and HN_3) sources are used to produce oxides and nitrides, respectively. Gas and liquid precursors are most commonly used, but solid source precursors can also be utilized. Since the goal in ALD is rapid saturation exposure of the precursor, the source phase and volatility of the precursor and the precise exposure conditions are less critical than in CVD (although the delivery system is highly critical). The self-limiting reaction sequence (i.e., the reaction cycle) does not typically result in monolayer deposition per cycle. Depending upon the size of the reactant and the attached ligands, saturation exposure and reaction of the precursor is most often submonolayer, and thus the resulting deposition layer produced per cycle is typically submonolayer. Hence, multiple cycles are commonly required to deposit a single monolayer. Although this enhances control of the thickness and conformality, it reduces the deposition rate and throughput of the process. Hence, ALD processes are envisioned for processes requiring less than ~40 nm thin films, and typically much less. As in CVD, it is desired to utilize both the versatility of selective ALD deposition as well as blanket uniform ALD deposition (e.g., to deposit barrier layers over both metals and dielectrics).[32] Besides the opportunity for atomic-level thickness control, ALD also promises control of material stoichiometry, reduced deposition temperatures, high conformality, reduced impurity levels, and controllable material properties (e.g., crystallinity, morphology, resistivity, etc.). The potential to control thickness at the sub-nm level, and the ability to deposit thin films over highly corrugated substrates with high aspect ratio topography makes ALD of great interest for integrated circuit and data storage applications. ALD is already in use for thin film head dielectrics, and

is expected to be increasingly used in integrated circuit manufacturing when circuit dimensions reach 90 nm, 65 nm, and below. It is envisioned that ALD will be used at these dimensions for deposition of high-k dielectric materials (gate dielectrics, capacitor dielectrics), barrier layers (TaN, TiN, WN, WN_xC_y), and seed layers or nucleation layers (W, and perhaps Ta and/or Cu). Other emerging applications include microelectromechanical systems fabrication, organic light emitting diodes displays, etc.[33]

3.4.3 Deposition Equipment

Design considerations for ALD reactors are a subset of those for CVD, specifically uniform substrate heating, reliable precursor delivery, minimal reactor volume, and high throughput. Since ALD is a surface adsorption and reaction controlled process, the growth temperature can play a critical role in the extent of reaction and in desorption of ligands and byproducts. Nonuniform substrate heating adversely affects thickness uniformity, impurity levels, material stoichiometry, and interface quality. Although precise precursor exposure is not required in ALD, reliable gas delivery without gas source depletion and complete purging of the reaction zone is important. In particular, the gas exposure must exceed saturation, and should not condense or be trapped elsewhere in the reactor. Small reactor volume enhances the ease and speed of purging, and improves chemical use efficiency.[33]

The ALD reactors can be divided into two types: evacuation and flow-type reactors.

- In evacuation-type reactors the precursor is pulsed into the reactor and after a certain reaction time the reaction chamber is evacuated and is ready for the next precursor pulse. These precursor pulse and pump down cycles are repeated until the desired film thickness is obtained. This is usually time-consuming, and rather expensive pumps such as turbomolecular or diffusion pumps are needed. An additional drawback is the pressure change, which may cause particle formation due to the film peeling off the reaction chamber walls. The evacuation type reactors resemble the pulse modulated MBE reactors. The advantage of these reactors is that it is easy to ensure that the precursor pulses are not overlapping

because the pressure of residual gases can be measured directly by a simple pressure gauge. In addition, some reactions appear to take place only in evacuation-type reactors.

- Flow-type reactors are usually operated at constant pressure and precursors are pulsed into the carrier gas. Flow-type ALD reactors are closely related to CVD reactors. In flow-type reactors the cycle times can be shortened which increases the productivity which is especially important from the industrial point of view.

3.4.4 Comparison of Deposition Techniques

It is interesting to compare the typical deposition conditions and the resulting process control possible with PVD, CVD, and ALD methods as shown in Table 3.1. Deposition by PVD and CVD has developed to be used in distinct situations whose choice depends primarily on the nature of the film to be deposited. Over the years, PVD and CVD deposition technologies and deposition tools have evolved to meet the increasingly more stringent requirements needed. However, we are likely to see gradual replacement of many PVD and CVD processes by ALD as device length scales are reduced and film quality, uniformity, conformality, and thickness control become ever more critical. Growth rates and throughput may limit ALD in some applications. However, the ability of ALD to deposit high quality, pinhole-free, highly conformal thin films and film composites may spawn many new applications and the coupling of ALD and CVD, and even perhaps ALD and PVD, process technologies.[33]

Table 3.1 Comparison of deposition properties for PVD, CVD, and ALD.[33]

Deposition conditions	PVD	CVD	ALD
Vacuum requirement	$<10^{-2}$ Torr	10^{-3}-10^{2} Torr	10^{-4}-1 Torr
Deposition thickness range	5 nm- > 10 μm	10 nm- >3μm	0.1-40 nm
Uniformity control	nm	nm	0.1 nm
Deposition rate	10-100 nm/min	10-1000 nm/min	<0.2 nm/cycle
Conformality	15% at 4:1 aspect ratio	0%-100% at 4:1 aspect ratio	100% at 15:1 aspect ratio
Contamination/particles	Indirect only (flaking)	Particles can exist due to gas phase reactions	Low: no gas phase chemistry

3.5 Atomic Force Microscopy

The principle of scanning probe microscopy (SPM) is very simple. It is based on scanning the surface with a very small tip at a close distance while monitoring for tip deflection or current or voltage between the tip and the sample. There are many variants of the SPM technique depending of the measured property, for example atomic force microscopy (AFM) measures forces between the tip and the surface atoms by monitoring the tip deflection, scanning spreading resistance microscopy (SSRM) measures resistance distribution on the surface using a conducting tip, scanning tunneling microscopy (STM) measures tunneling current, ect. Among the scanning probe microscopy techniques, AFM results one of the most versatile as it does not imply any special required characteristic on the sample surface. For example, STM requires a conductive surface to assure enough tunneling.

3.6 Fourier Transformed Infrared (FTIR) Spectroscopy

Infrared spectroscopy (IR) can result in a positive identification (qualitative analysis) of every different kind of material. In IR radiation is passed through a sample. Some of the infrared radiation is absorbed by the sample and some of it is passed through (transmitted). The resulting spectrum represents the molecular absorption and transmission, creating a molecular fingerprint of the sample. The size of the peaks in the spectrum is an indication of the amount of material present. FTIR can provide information to identify unknown materials; it can determine the quality or consistency of a sample and the amount of component in a mixture.

References (Chapter 3)

1 W. Kern, Handbook of Semiconductor Wafer Cleaning Technology, p. 11 (1993).

2 Burkman, D. C., Semiconductor International, 4(7):103-114 (1981).

3 Kern, W. and Puotinen, D., RCA Review, 31:87-206 (1970).

4 Amick, J. A., Solid State Technology, 19(11):47-52 (1976).

5 Kikuyama, H. and Miki, N., Proc. 9th Internafional Symp. Contam. Control, pp. 387-383, Institute of Environm. Sciences, Mount Prospect, IL (1988).

6 Henderson, R. C., J. Electrochem. Soc., 119(6) 771-775 (1972).

7 Kern, F., Jr., Mitsushi, I., Kawanabe, I., Miyashita, M., Rosenberg, R. W. and Ohmi, T., "Metallic Contam. of Sem. Devices from Processing Chem., The Unrecognized Potential," (1991).

8 Riley, D. J. and Carbonnel, R. G., Proc. 37th Annual Technical Meeting, pp. 886-891, The Institute of Environmental Sciences, Mount Prospect, IL (1991).

9 Milner, T. A. and Brown, T. M., Proc. Microcontaminafion Conf and Exposition, pp. 146-156 (1986).

10 Menon, V. B. and Donovan, R. P., Proc. First International Symposium on Cleaning Technology in Semiconductor Device Manufacturing/7989, 90-9:167-181, (J. Ruzyllo and R. E. Novak, eds.), The Electrochemical Society, Pennington, NJ (1990).

11 Atsumi, A., Ohtsuka, S., Munehira, S. and Kajiyama, K., Proc. First International Symposium on Cleaning Technology in Semiconductor Device Manufacturing/7989,90-959-66, (J. Ruzyllo and R. E. Novak, eds.), The Electrochemical Society, Pennington, NJ (1990).

12 Menon, V. B., Clayton, A. C. and Donovan, R. P., Microcontamination,7(31):31-34, 107-109 (1989).

13 Peterson, C. A., Schmidt, W. R., Burkman, D. C. and Phillips, B. F., Proc. Technical Programme Semiconductor 1983 International, (27-29 September, 1983).

14 Watanabe, M., Harazono, M., Hiratsuka, Y. and Edamura, T., E/e&othem.Sot. Ext. Abstracts, 81-3:221-222 (1983).

15 Shwartzman, S., Mayer, A. and Kern, W., RCA Review, 46:81-105(1985).

16 Slusser, G. J. and MacDowell, L., J. Vat. Sci. Technology, A-5(4):1649-1651 (1987).

17 Kawado, S., Tanigaki, T. and Maruyama, T., Semiconductor Silicon1986, Proc. Fifth. The Electrochemical Society, Pennington, NJ (1986).

18 Seitaro, S. I. and Tanaka, F., Proc. 9th Infernafional Symposium onContamination Control, pp. 374-377, The Institute of Environm. Sciences, Mount Prospect, IL (1988).

19 Kern, W., Proc. First international Symp. on Cleaning Technology in Semiconductor Device Manufacturing/1989, 90-9:3-I 9, (J. Ruzyllo and R. E. Novak, eds.), The Electrochem. Soc., Pennington, NJ (1990).

20 W. Kern, Semicond. Int.,7 (4), 94 (1984).

21 S.Watanabe, N.Nakayama and T.Ito, Appl. Phys. Lett 59, 1458(1991).

22 W. Kern, Proc. First international Symposium on Cleaning Technology in Semiconductor Device Manufacturing/1989, 90-9:3-I 9, (J. Ruzyllo and R. E. Novak, eds.), The Electro-chemical Society, Pennington, NJ (1990).

23 Skidmore, K., Semiconductor International, 12(8):80-86 (1989).

24 W. Kern, J, Electrochem. Soc., 137(6):1887-1892 (1990).

25 Riika L. Puurunen, Journal of Applied Physics 97, 121301 (2005).

26 A. M. Shevjakov, G. N. Kuznetsova, and V. B. Aleskovskii, in Chemistry of High-Temperature Materials, Proceedings of the Second USSR Conference on High-

Temperature Chemistry of Oxides, Leningrad, USSR, 26–29 November 1965 (Nauka, Leningrad, USSR), pp.149–155, in Russian (1967).

27 T. Suntola and J. Antson, U.S. Patent No. 4,058,430 (15 November 1977).

28 M. Ritala and M. Leskelä, in Handbook of Thin Film Materials, edited by H. S. Nalwa (Academic, San Diego,), Vol. 1, pp. 103–159 (2002).

29 Hyoungsub Kim, Paul C. McIntyre, Journal of the Korean Physical Society 48-1, 5-17(2006).

30 S. M. George, A. W. Ott, and J. W. Klaus, J. Phys. Chem. 100, 13121 (1996).

31 D. H. Everett, Pure Appl. Chem. 31, 579 (1972); web version http://www.iupac.org/reports/2001/colloid_2001/ manual_of_s_and_t.pdf.

32 J. Gelatos, L. Chen, H. Chung, R. Thakur, and A. Sinha, Solid State Technol. 46, 44 (2003).

33 Crowell John E., J. Vac. Sci. Technol. A 21(5), (2003).

Chapter 4

Experimental Details and Results

The experimental details and the results obtained in this thesis are presented in this chapter. The purpose of using these methods was to characterize the chemical structure of the films studied.

Chapter 4. Experimental Details and Results

4.1 Description of the Samples

Hafnium dioxide depositions by ALD technique, AFM and FTIR measurements were carried out in the class 1000 Cleanroom of The University of Texas at Dallas (Figure 4.1). Additionally, angle-resolved monochromatic x-ray photoelectron spectroscopy measurements were performed in a unique multi-modular cluster tool for the fabrication and characterization of thin films (Figure 4.16) in the Department of Materials Science and Engineering at The University of Texas at Dallas.

Figure 4.1 Cleanroom Research Laboratory at The University of Texas at Dallas.

The process of making the samples is illustrated in the Figure 4.2, first the Silicon substrates are cleaned using the RCA method, and subsequently these wafers are HF dipped. As the focus on this work is to study the effect between Hydrogen and Silicon Oxide substrate termination, for the first case the HF dipped a wafer goes to an ALD chamber to grow HfO_2. In the second case, prior to the HfO_2 deposition, 1nm of SiO_2 is grown on top the Si substrate by thermal annealing, and finally the HfO_2 is deposited via ALD with the same conditions that in the first case.

Afterward, according to the main purpose of this thesis, the surface morphology and composition of these samples were characterized through AFM, FTIR and high-resolution Angle Resolved XPS techniques.

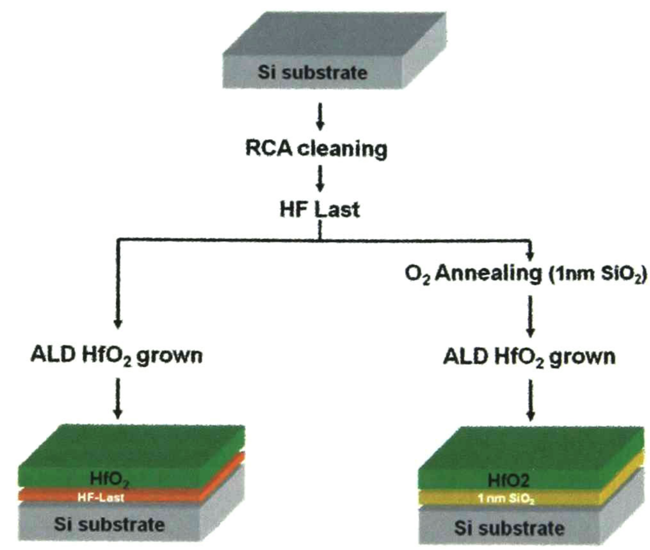

Figure 4.2 Sample preparation process.

4.2 Substrate Preparation

The surface cleaning was done in an acid hood located in a class 1000 Cleanroom Research Laboratory in The University of Texas at Dallas. The substrates used were 4 inches, p-type (100) silicon wafers and were cleaned using the modified RCA cleaning method similar to the one described in section 3.2. The modified RCA cleaning process is described step by step in the following table (Table 4.1):

Table 1.1 Modified RCA wafer cleaning process.

Step	Process	Container	Solution Temp (°C)	Time (min)	Comments
1	Pour 6 parts of H_2SO_4 and heat. Add one part of H_2O_2 at 65°C.	Glass Beaker (5000ml) on hotplate.	85	10	Stir solution at all times.
2	"Running" DI water rinse of Si		RT	1	
3	Take 4 parts of H_2O. Add 1 part of HF. Add 1 part of H_2O_2.	Teflon Bucket.	RT	1	

4	"Running" DI water rinse of Si		RT	1	
5	Take 5 parts of H_2O. Add 1 part of NH_4OH and heat. Add 1 part of H_2O_2 at 60°C.	Glass Beaker (5000ml) on hotplate.	80	5	Stir solution at all times.
6	"Running" DI water rinse of Si		RT	1	
7	Take 6 parts of H_2O. Add 1 part of HCl and heat. Add 1 part of H_2O_2 at 60°C.	Glass Beaker (5000ml) on hotplate.	85	10	Stir solution at all times.
8	"Running" DI water rinse		RT	1	
9	HF + H_2O (1:50). (ACIDIC)	Teflon Bucket.	RT	1	An Optional Step. Should be done before loading the wafer for processing.
10	Spin and drying				

The RCA cleaned wafers were dipped in HF for 60 seconds in 100:1 aqueous solution and rinsed in DI water. Then the wafer was dried by blowing CMOS-grade nitrogen. It took about 1 minute to take the wafer into the deposition chamber.

4.3 Thermal Growth of 1nm SiO_2 Layer

The presence of thin silicon oxide interfacial layer may actually facilitate better electrical properties.[1,2] This interfacial layer places constraints on the thickness of the high-κ material deposited. For example, to obtain an equivalent oxide thickness less than 2 nm, the thickness of the high-κ (e.g., κ=15-30) material should be less than 4 nm, when there is a 1nm SiO_2 interfacial layer.[3]

There have been extensive studies based on the application of ultra-violet (UV) generated ozone (O_3) for surface cleaning and oxidation processes. The potential advantages of the UV/O_3 process include the self-limiting oxide growth mechanism and thickness uniformity. However thermal oxidation provides a better quality oxide in terms of interface quality.

In this context, good quality SiO_2 was grown by UV O_3 oxidation followed by thermal annealing in O_2 at 400 °C on top the Si clean substrate, using the steps showed below.

4.3.1 UV Ozone

The UV ozone oxidation process was done in-situ to avoid any spurious interfacial layer growth and to remove carbon contaminants. The ozone was generated using ultra-high purity O_2 with a pressure of 980 mbar in the precensce of a Hg lamp. The UV lamp was installed in a wafer transit chamber in the annealing module (see Figure 4.16). The UV O_3 exposure was carried out during 10 minutes first, then the Si substrate was rotated 180° and it was exposed for 10 minutes more to provide a better uniformity. This process was done at room temperature in 980 mbar of ultra-high purity O_2.

4.3.2 O_2 Annealing

After UV O_3 oxidation, the sample was then annealed in O_2 at 400 °C for 45 min. This procedure provides a uniform SiO_2 of good quality. XPS was used to measure the thickness of silicon oxide grown layer.

4.3.3 SiO_2 Film Thickness Measurement by XPS

The SiO_2 film thickness d_{oxy} was determined using XPS by taking the area ratio of the Si 2p component of the oxide to the one from the bulk. The XPS Si 2p region of the resulting SiO_2/Si is shown in Figure 4.3.

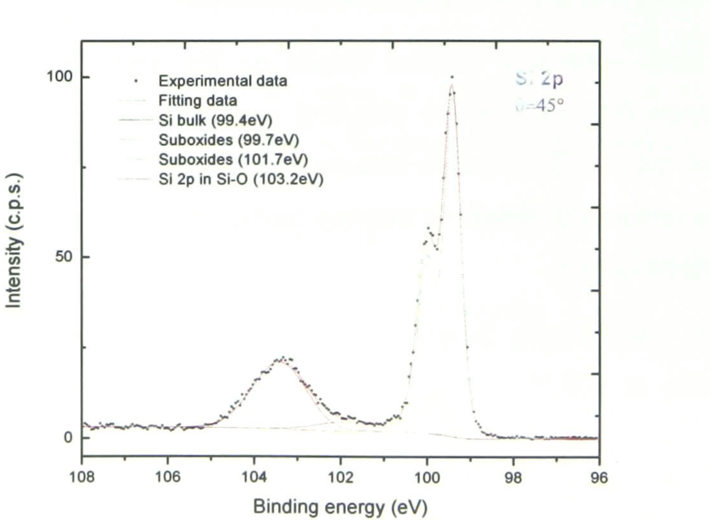

Figure 4.3 Si 2p spectrum of 1 nm SiO_2 thermally grown before HfO_2 deposition.

The calculation was done employing XSPGeometry[4] (see section 2.8.2) and Equation 4.1 and the Si 2p core level intensity ratio of the oxidized silicon film I_{oxy} and substrate silicon I_{Si} .[5]:The oxide thickness is given by:

Equation 4.1 $$d_{oxide} = \lambda_{oxide} \sin\alpha \ \ln[I_{oxide}/(\beta I_{bulk})+1]$$

where λ_{oxy} is the photoelectron effective attenuation length in the oxide film, α is the photoelectron take-off angle, and $\beta = I_{oxy,\infty}/I_{Si,\infty}$ is the ratio of measured photoelectron signals in opaque films (≥ 15 nm at α ≥70°). The Equation 4.1 was derived based on the assumption that the photoelectron signal has an exponential depth distribution function. The effective attenuation length and inelastic mean-free path are considered equivalent when elastic scattering effects are neglected.[6]

The resulting SiO_2 thickness was 1.1 nm from Equation 4.1, and 1.4 nm when employing XPSGeomety®.

4.4 ALD Growth of HfO_2 Films

The Hafnium oxide films were grown by ALD on SiO_2- and H-terminated p-type Si (100) substrates from Tetrakis-ethylmethylamino-Hafnium (TEMA-Hf) and H_2O (oxygen source) as the precursors at 300 °C.

TEMA-Hf {$Hf[N(CH_3)(C_2H_5)]_4$} is a clear liquid that reacts immediatly upon contact with water or moisture, with the evolution of ethylmethylamine and hafnium oxide/hydroxide formation. Handling in perfectly dried piping and components is mandatory for high-performance, particle-free processing.[7] A schematic ball diagram model of TEMA-Hf molecule is shown in Figure 4.4.

A commercial Savannah 100 ALD system manufactured by Cambridge Nanotech was used for the film growth in these experiments. The reactor pressure during the deposition was about 4.6×10^{-1} Torr (6.1×10^{-4} atm) and the nitrogen flow used as a carrier and purging gas was 20 sccm. The pulsing of reactants was accomplished by solenoid valves; needle valves were used to control the dose of some of the externally evaporated sources.

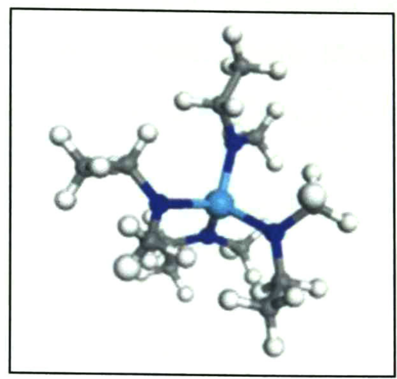

Figure 4.4 TEMA-Hf molecule. TEMA-Hf was employed as Hf source in the Hafnium oxide deposition by ALD.

The ALD equipment is controlled from the system software (Savannah-100). The temperatures used through the process were 300 °C in the substrate, 200 °C in the wall, 130 °C in the cylinder and 105 °C in the solenoid valve, as is indicate in Figure 4.5.

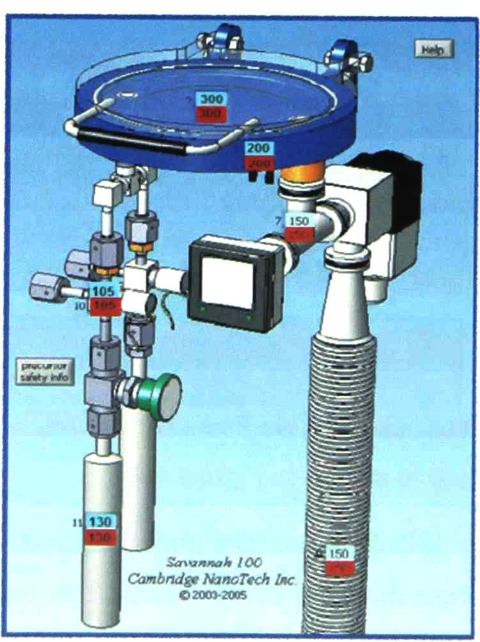

Figure 4.5 ALD Cambridge Nano Tech system. The system allows a perfect temperature control during the deposition.

The cycle matrix allows programming of a cycle sequence (recipe), the reactants pulses and N_2 pump time used during the deposition process is showed in Table 4.2. The ALD cycle parameters for this system were previously optimized by testing the thickness and film quality of HfO_2. The growth per cycle (GPC) under the mentioned conditions is ≈ 1 Å.

Table 4.2 ALD process matrix.

Valve	Pulse (s)	Expo (s)	Pump (s)
H_2O	0.05	0	7
TEMA-Hf	0.2	0	7

Each precursor is pulsed into the reaction chamber alternately, one at a time, and the pulses are separated by inert gas purging periods. Initially, TEMA-Hf is pulsed for a short time (0.2 seconds) into the reaction chamber and it is chemically adsorbed on the surface until the adsorption sites present are saturated. After the metal precursor pulse the excess of precursor is removed by nitrogen purge, during 7 seconds. Next water is pulsed into the reactor for 0.05 seconds, and it reacts with the existing precursor layer. The following step removes the excess of water and the by-product molecules by purging with nitrogen during 7 seconds. After the second purge the surface consists of the similar functional groups as in the beginning of the ALD cycle and thus it is ready for the next ALD cycle. If each step is saturative, self-limiting growth is achieved which is considered an ALD process.

By cycling the pulse/purge loop, one can obtain a well-controlled, surface-saturating deposition of a HfO_2 film, and the total growth rate is determined by the availability of precursor adsorption sites, the size of the adsorbing molecules and the tendency for desorption during the purge step.

In order to understand the effect of the initial stages of growth of HfO_2 film on the different substrates terminated, two series of samples were grown in ALD. 5 cycles and 30 cycles cases were studied. Plots of the pressure sequence into the reactor

during the ALD process are showed in Figure 4.6 and Figure 4.7, for 5 and 30 cycles, respectively.

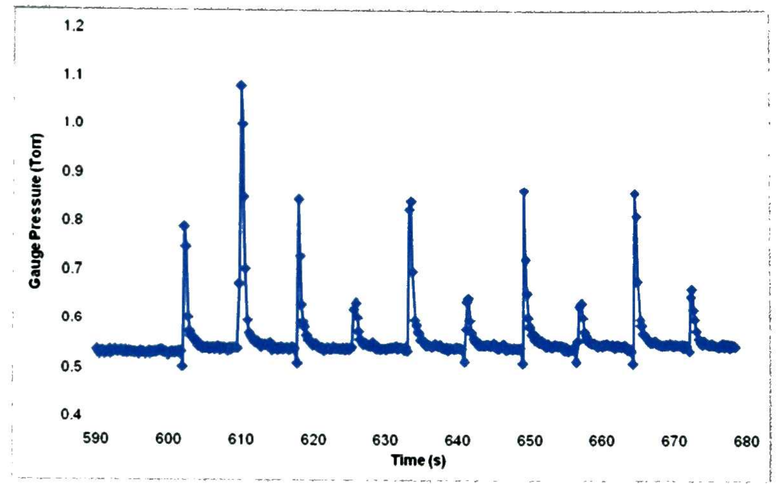

Figure 4.6 Reactor pressure during 5 cycles of HfO_2 ALD deposition.

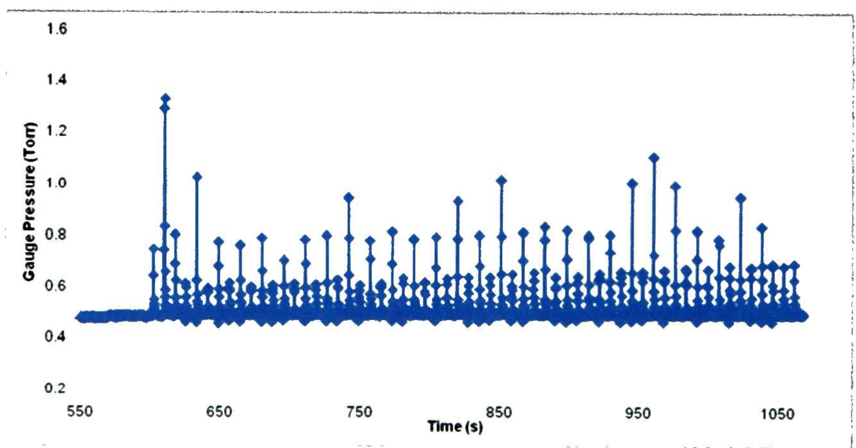

Figure 4.7 Reactor pressure during 30 cycles of HfO_2 ALD deposition.

4.4 Atomic Force Microscopy Images

The surface morphology of the HfO_2 films was studied employing AFM. AFM can give quantifive of the films topography.. The equipment used for this study was a Nanoscope XS06 (Digital Instruments Co.), which was mainly used for roughness measurements and imaging of surface structure.

Figure 4.8 and Figure 4.9 illustrate the AFM surface morphologies with the respective RMS roughness of HfO_2 film with different substrate termination: H and $-SiO_2$, using 5 ALD cycles in both cases. The RMS roughness is 0.149 nm and 0.163 nm respectively in a scan area of 500 nm.

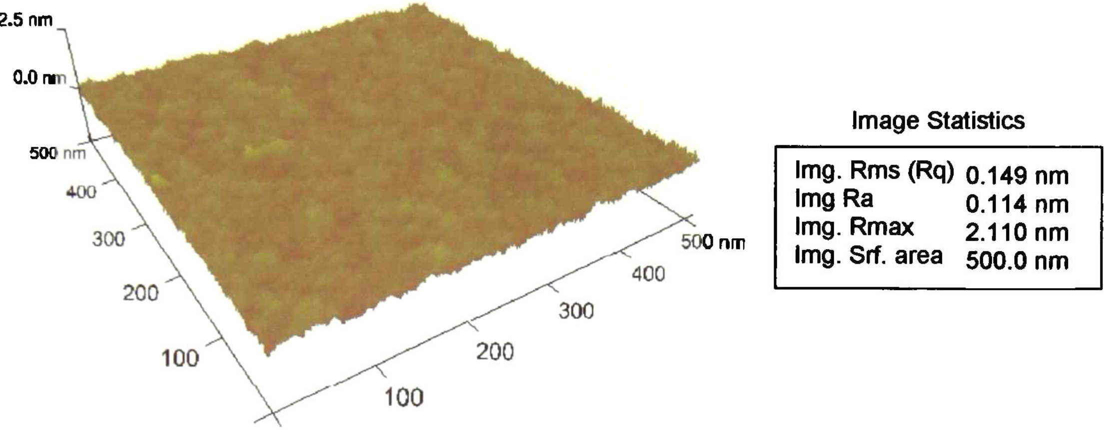

Figure 4.8 AFM topographs of the HfO_2 films on H-terminated substrates grown by ALD using 5 cycles.

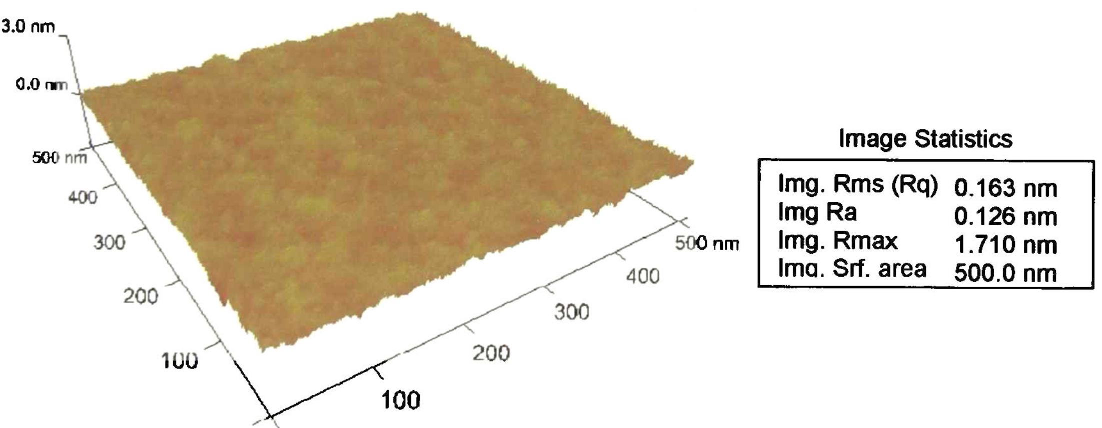

Figure 4.9 AFM topographs of the HfO_2 films on SiO_2-terminated substrates grown by ALD using 5 cycles. The RMS average roughness is 0.16 nm for 5-cycles samples.

Figure 4.10 and Figure 4.11 show the AFM topographs with the RMS roughness of HfO_2 film with H and SiO_2 substrate terminations, using 30 ALD cycles in the two cases. The RMS roughness is 0.149 nm and 0.156 nm respectively in a scan area of 500 nm.

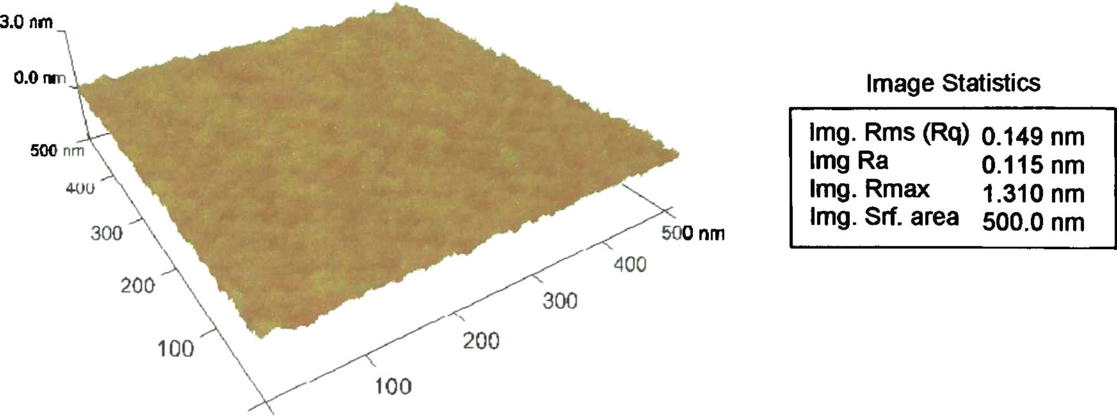

Figure 4.10 AFM topographs of the HfO_2 films on H-terminated substrates grown by ALD using 30 cycles. ALD growth allows to obtain very uniform films and with good conformality.

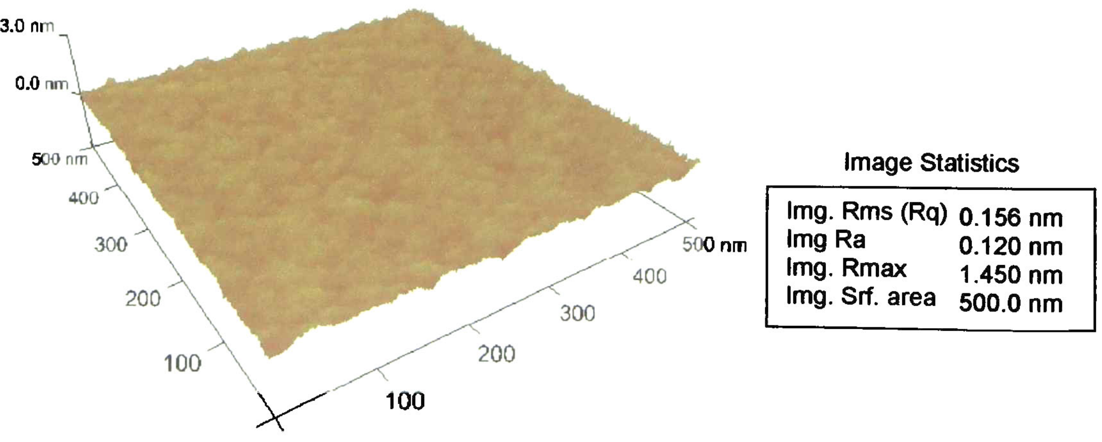

Figure 4.11 AFM topographs of the HfO_2 films on SiO_2-terminated substrates grown by ALD using 30 cycles. The RMS average roughness is 0.15 nm for 30-cycles samples.

AFM measurements prove uniformity and smooth surface of the films, topographical analysis of films surfaces show that the roughness slightly increases in the samples with SiO_2-terminated substrate but this decrease when the number of cycles used is increased.

4.6 Fourier Transmission Infrared Spectroscopy

FTIR is a rapid analytical technique based on the light absorption characteristics of various chemical compounds in a material. Each type of chemical bond (or functional group) absorbs light of a particular wavelength or range of wavelengths. The presence or absence of absorption peaks for particular bond types or functional groups provides information on the absence or presence of certain compound classes in the given sample.

FTIR absorption measurements were performed to study the structure changes in the samples. These measurements were carried out using a Nicolet 6700 spectrometer in ATR (Attenuated total reflectance) mode with a resolution of 4 cm^{-1}. A background spectrum was subtracted from the actual measurements and was taken using a reference sample cut from the same Si (100) p-type wafer. The determination of the peaks was done through comparison with reference spectra of known materials.

The spectra given in Figure 4.12 shows a comparison between thinner HfO_2 films (5 ALD cycles) on H- and SiO_2-terminated substrates. It is important to notice that in the sample with thermally grown SiO_2 the most intense absorption peak of O-Si-O at ~1240 cm^{-1} while for the H-terminated substrate it shows a shift for the O-Si-O band. In addition, the absence of any absorption peak in O-Hf-O band indicates the no presence of HfO_2 layer.

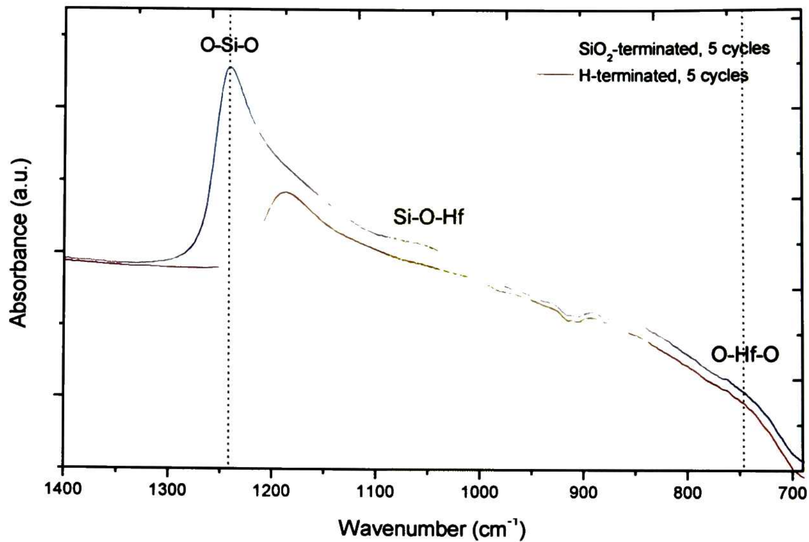

Figure 4.12 Comparison of the absorption FTIR spectra between samples using 5 ALD cycles on different terminated Si substrate: H-terminated and SiO_2-terminated. The shift of the O-Si-O band for the H-terminated sample might be attributed to the lack of a fully formed silicon oxide. The SiO_2 terminated sample showed a larger signal for the Si-O-Hf band.

The next spectra (Figure 4.13) illustrate the difference between thicker samples (30-ALD cycles) on both substrate preparation (H- and SiO2-terminated). It is important to notice that in the substrate terminated with SiO_2 presents the most intense absorption peak of O-Si-O at ~1240 cm^{-1} while the H-terminated sample shows a shift for this band. In addition, the presence of O-Hf-O absorption signal band at ~740 cm^{-1} indicates the formation of HfO_2 layer.

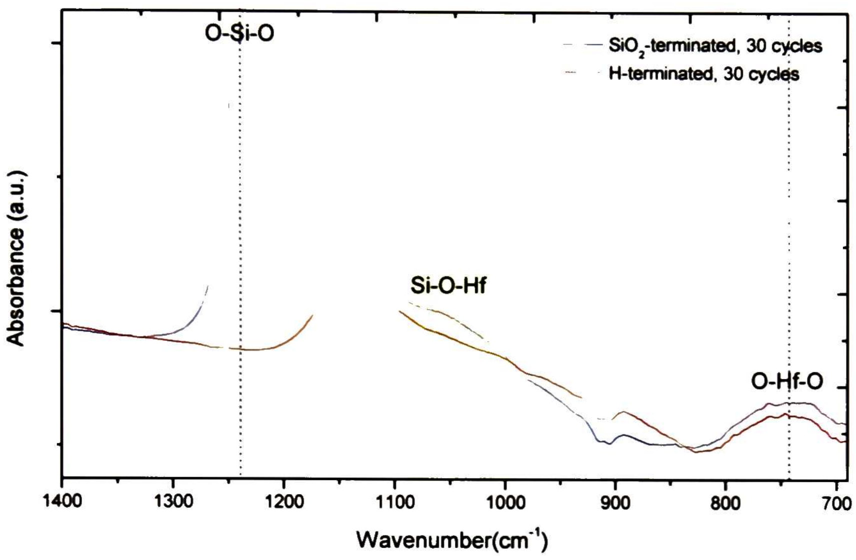

Figure 4.13 Comparison of the absorption FTIR spectra between samples using 30-ALD cylces on different substrate terminations. The band associated to Si-O-Hf is more apparent for the SiO_2- terminated sample.

Figure 4.14 and Figure 4.15 show the overlayed FTIR spectra of the 5 and 30 cycles samples for the same substrate termination. It clearly demonstrate that the signal of O-Hf-O (~740 cm^{-1}) increases with the raising of ALD number of cycles. In this context the samples with 30 ALD cycles show the HfO_2 presence while the 5-cycles did not. Furthermore, is interesting to noticing that the intense peak at ~1240 cm^{-1} (O-Si-O band) is only present for the sample terminated with SiO_2 and the samples H-terminated presents some shift in this band.

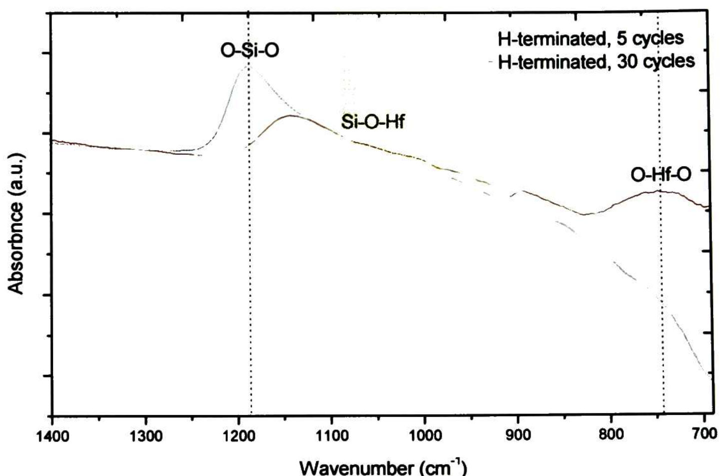

Figure 4.14 Comparison of the absorption FTIR spectra between samples with H-terminated Si substrate using different number of cycles (5 and 30) during the ALD HfO_2 deposition. The shift of the O-Si-O band for the H-terminated sample might be attributed to the lack of a fully formed silicon oxide. The SiO_2 terminated sample showed a larger signal for the Si-O-Hf band.

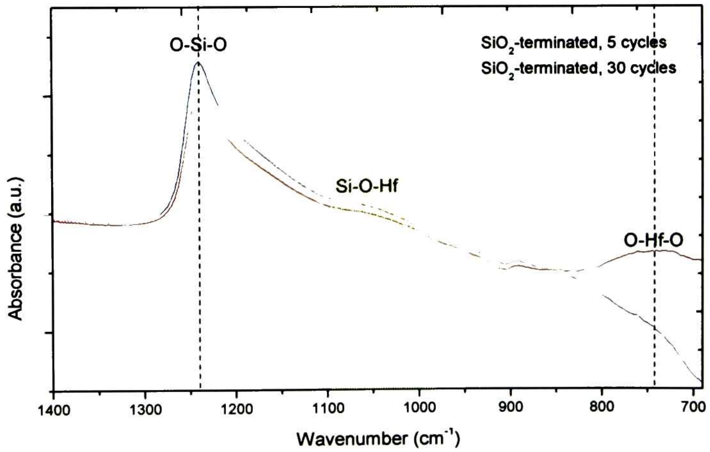

Figure 4.15 Comparison of the absorption FTIR spectra between samples with SiO_2-terminated Si substrate using different number of cycles (5 and 30) during the ALD HfO_2 deposition. The band associated to O-Hf-O indicates a clear evidence of hafnium oxide growth for 30-cycles sample, while in 5-cycles samples there is not.

All the spectra showed above (Figure 4.12, Figure 4.13, Figure 4.14 & Figure 4.15) shows the presence of Si-O-Hf band in the 1000-1100 cm^{-1} range and it could be attributed to the possible formation of silicates during the ALD deposition.

4.7 Angle Resolved XPS

For a detailed study on the chemical structure of the film and interface, we analyzed each XPS core level of interest (Si 2p, Hf 4f, C 1s, O 1s and F 1s) recorded with high resolution by using a small analyzer pass energy (15 eV). This section shows the spectra lines and the corresponding fits of each one of the sample studied in this thesis.

It is important to notice that the fitting were done using AAnalyzer® software (Section 2.8.1) with the appropriate parameters for each core level[8], the details are explained below.

4.7.1 Data acquisition

The bonding states at different depths were obtained through a carefully analysis of Angle Resolved XPS data. The XPS experiments presented in this thesis were carried out at the University of Texas at Dallas using an analytical module manufactured by Omicron Nanotechnology Ltd. This module is part of a multi-technique and characterization cluster tool depicted in Figure 4.16.

The XPS experiments were performed using a monochromatic Al Kα source (1486.7 eV) with a pass energy of 15 eV. For ARXPS multiple take-off angles were automatically taken from 25° to 75° with steps of 10°. The take-off angle is measured respect to the surface plane being 25° the most surface sensitive and 75° more sensitive to the bulk. Figure 4.17 show an actual picture of the XPS system at UTD used for these experiments.

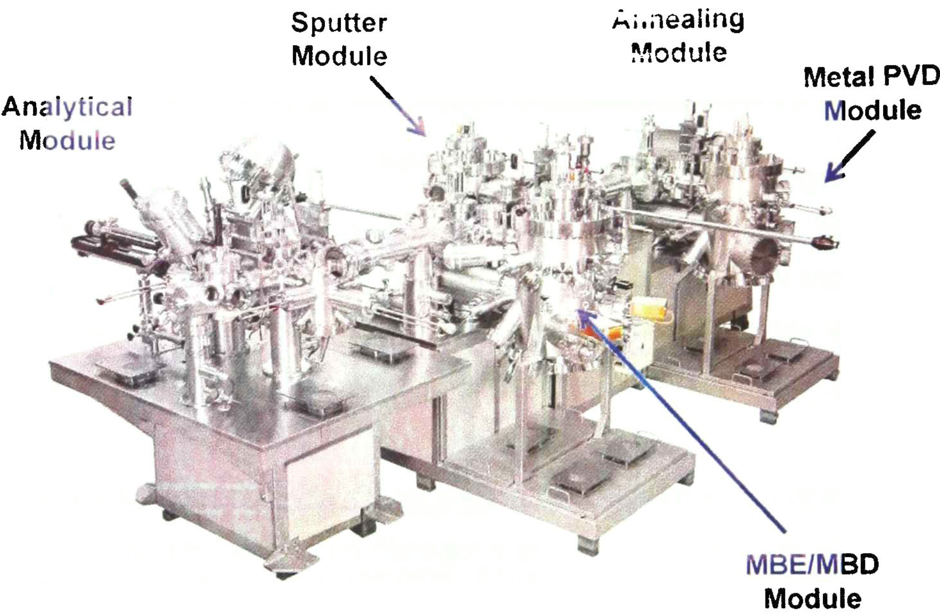

Figure 4.16 UHV deposition and characterization cluster tool at the University of Texas at Dallas.

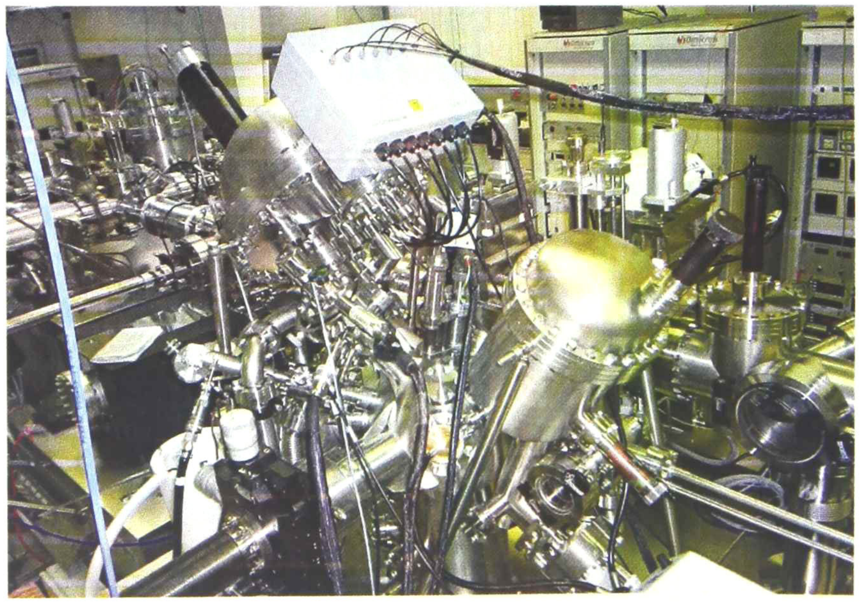

Figure 4.17 Spectroscopy chamber used for ARXPS experiments.

The ARXPS experimental setup is shown in Figure 4.18. The angle between the incoming x-ray beam and the analyzer is 90°. To perform the ARXPS experiment the sample is rotated to the desired take-off angle. This figure shows an example of ARXPS data taken on a 1 nm thick SiO_2 on Si sample. It is observed how the bulk peak (at 99.4 eV) increases with the take-off angle while the SiO_2 remains nearly unchanged.

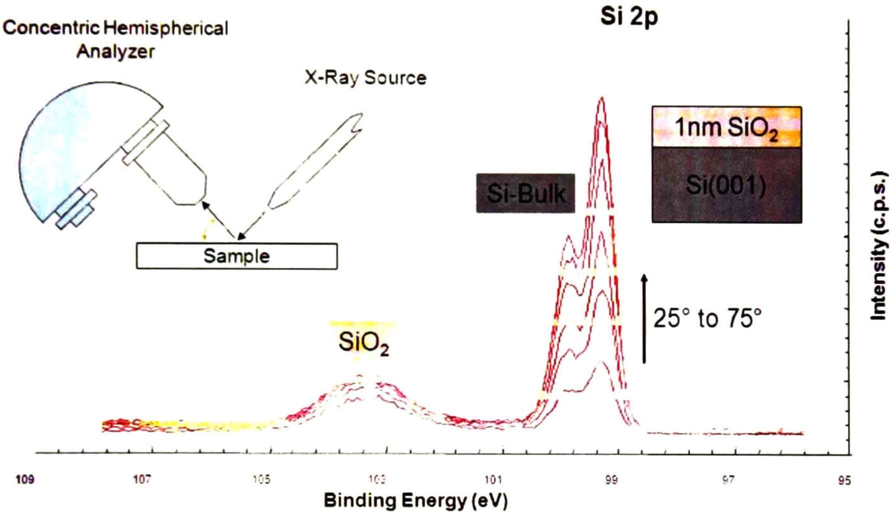

Figure 4.18 Angle Resolved XPS experiment.

4.7.2 Sample Heating in UHV

Prior to Angle Resolved XPS measurements the samples were heated *in-situ* in order to remove carbon and water from the surface.. The *in-situ* sample annealing was carried out using radiative heating from a Ta coil on the back of the sample holder. The annealing was done at 300 °C for 20 minutes (Figure 4.19). Using liquid Nitrogen the samples were cooled down to room temperature to perform the XPS measurements.

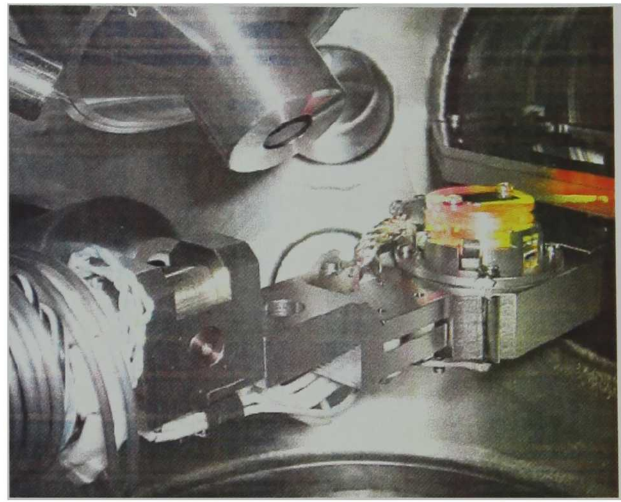

Figure 4.19 In-situ annealing in UHV to 300 °C for 20 minutes previous to Angle Resolved XPS measurements.

4.7.3 XPS Survey

During regular practice of XPS measurement a survey region is first recorded to identify the chemical components in the sample and to define acquisition windows. The survey region is a low resolution quick XPS scan. The lines of our interest Si 2p, Hf 4f, C 1s, O 1s and F 1s (Figure 4.20) which were recorded also at high resolution for an appropriate ARXPS analysis.

Similar measurements with exactly the same conditions were performed in HfO_2 films grown using 30 cycles in ALD process. The survey spectra are showed in Figure 4.21.

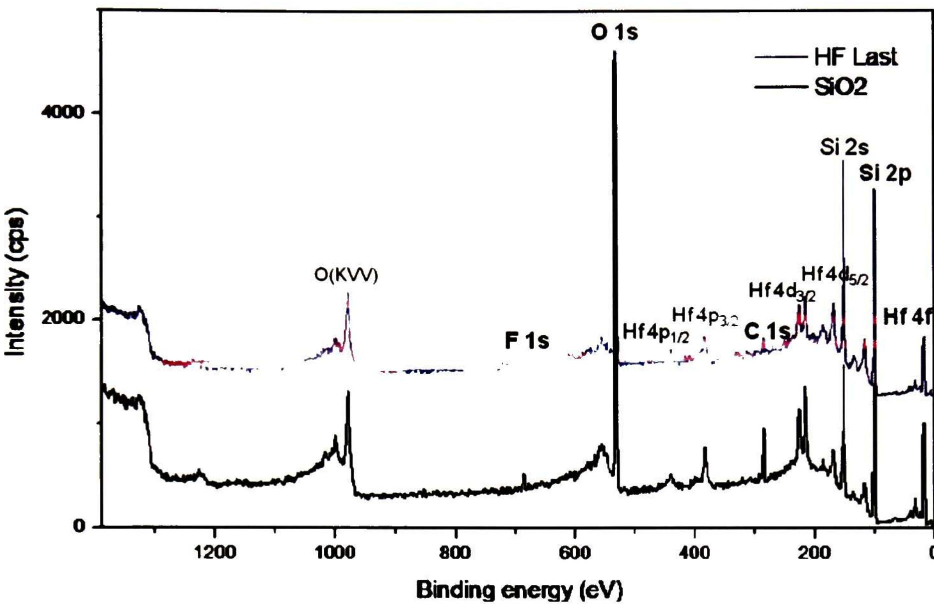

Figure 4.20 Survey for samples with 5 ALD cycles with different substrate terminations. This wide scan allows to identify the chemical components present in the sample and to define acquisition windows.

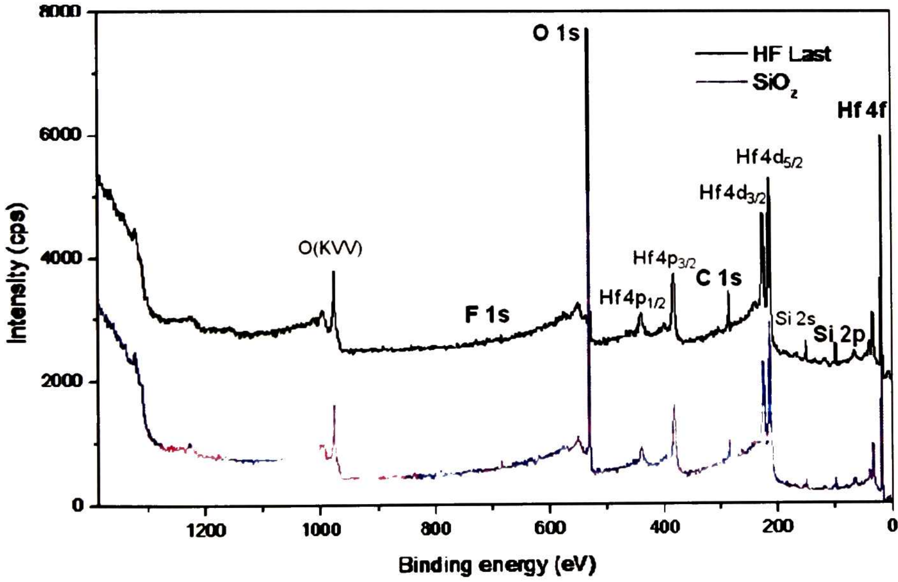

Figure 4.21 Survey for samples with 30 ALD cycles with different substrate terminated. Si 2p, Hf 4f, C 1s, O 1s and F 1s lines were recorded at high resolution for an appropriate ARXPS analysis

4.7.4 XPS Analysis of HfO_2 on H-terminated Si Substrate Using 5 ALD Cycles

The Si 2p spectrum, shown in Figure 4.22, was analyzed by its de-convolution in five components, each one being a doublet. A doublet consists of two singlets of the same width with a fixed binding energy separation (spin-orbit splitting) and a fixed intensity ratio. Each one of the singlets forming a doublet is the convolution of a Lorentzian with a Gaussian function. From now on we will refer to these parameters as the spin-orbit splitting, ratio, Gaussian and Lorentzian of the singlet for "s" orbitals and doublet "p", "d", etc., orbitals. The binding energy position for the doublet is taken as the position of the larger component. For example, for Si 2p doublet, the binding energy will be taken as the position of the Si $2p_{3/2}$ peak. . The background used for the fit of the Si 2p data was an integral function (usually called Shirley) and subtracted from the spectra. The value for the spin-orbit splitting was 0.6 eV and the doublet ratio was set to 0.5 (a typical value for a "p" orbital). The Lorentzian width had a value of 0.085 eV, and for the Gaussian the values used varied between 0.4 and 0.9 eV. The lower energy chemical component, centered at 99.4 eV, is attributed to silicon in the bulk and the higher binding energy showed at 103.2 eV is assigned to Si-O bonds.

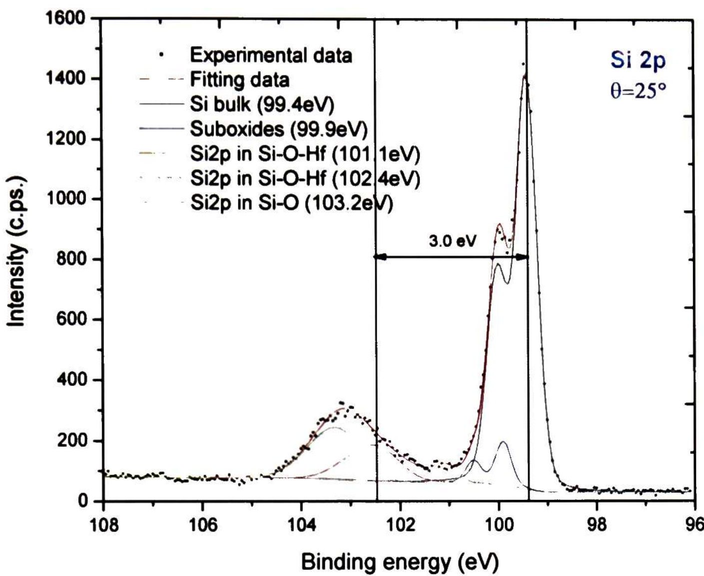

Figure 4.22 Core level Si 2p XPS spectrum at 25° for 5 ALD cycles of HfO_2 deposited on a H-terminated Si substrate. The binding energy difference between Si in the bulk and in $Hf_{0.33}Si_{0.67}O_{1.62}$ is 3.0 eV.

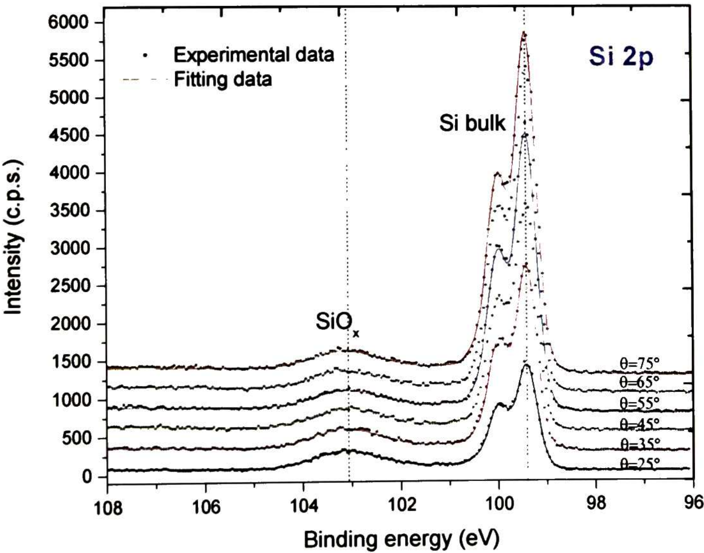

Figure 4.23 Angle Resolved XPS for Si 2p region of HfO_2 film on H-terminated Si substrate using 5 ALD cycles.

The peak found at 102.4 eV is attributed to Si-O-Hf bonds with an intermediate binding energy position between the Si substrate and SiO_2. The other peaks closer to the bulk were attributed to suboxides. Figure 4.23 shows the Si 2p high resolution spectra recorded at several take-off angles.

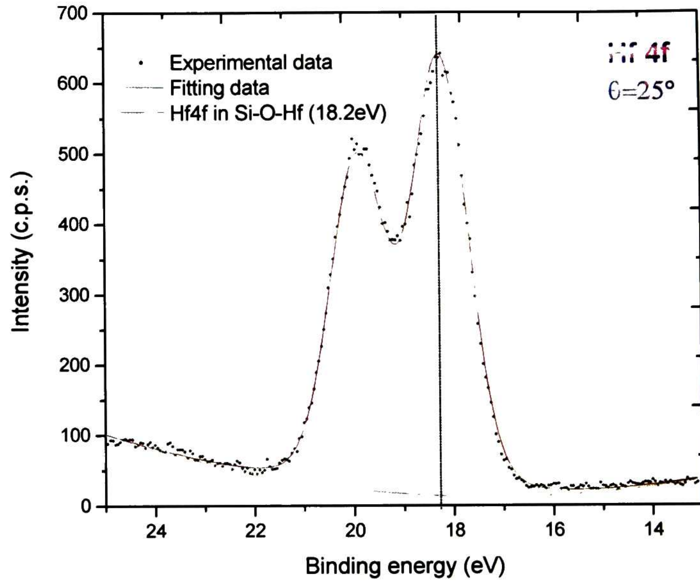

Figure 4.24 Core level Hf 4f XPS spectrum at 25° for 5 ALD cycles of HfO_2 deposition on H-terminated Si substrate. Only one chemical component is present. As it will be shown in Chapter 5, this component corresponds to hafnium silicate (18.2eV).

The Hf 4f XPS region for this sample is shown in Figure 4.24. The data was fitted with a single Hf 4f doublet. The resulting Hf 4f chemical component corresponds to Hf in hafnium silicate ($Hf_xSi_{1-x}O_y$). For this fit the spin-orbit splitting was set 1.7 eV. The Lorentzian width was found to be 0.041 eV for all the Hf 4f fits showed in this thesis. The Gaussian width obtained was1.26 eV. The background used was polynomial of second order. All the peaks were fitted consistently, *ie.*, all the peak parameters used were the same for all angles except for the peak heights that were allowed to change from angle to angle. The same procedure was applied for all the different set of ARXPS data showed in this thesis. Figure 4.25 shows a collection of Hf 4f XPS

spectra for the several take-off angles taken. The XPS data for all angles are successfully fitted with a single chemical component.

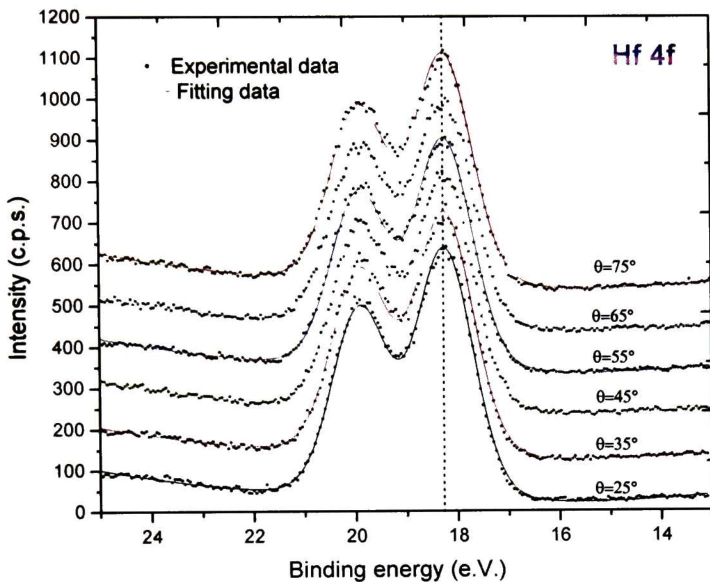

Figure 4.25 Angle Resolved XPS for Hf 4f region of HfO_2 film on H-terminated Si substrate using 5 ALD cycles.

The XPS region for O 1s is shown in Figure 4.26. The minimum number pf peaks to fit this region is two. The peak found at 531.65 eV was identified as oxygen forming Si-O-Hf bonds. The second peak found at 532.4 eV was attributed to Si-O bonds. The Lorentzian width for O 1s found was 0.25 eV and is the same value used for O 1s through all the fits. The obtained Gaussian width for this sample was 1.45 eV. The background used for this fit was integral type. Figure 4.27 shows the best fits for the O 1s region for the several take-off angles taken.

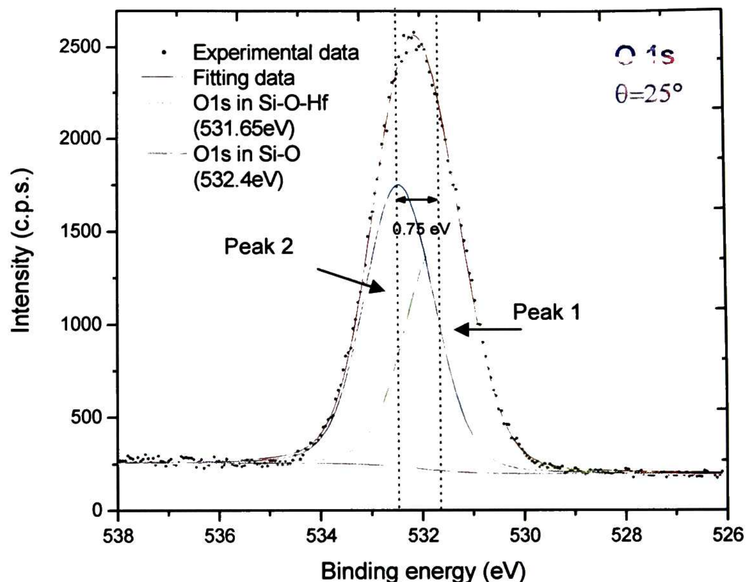

Figure 4.26 Core level O 1s XPS spectrum at 25° of HfO_2 film on H-terminated Si substrate using 5 ALD cycles. The spectrum clearly showed two peaks separated by 0.75eV, one associated to silicon oxide (532.4 eV) and another to hafnium silicate (531.65 eV).

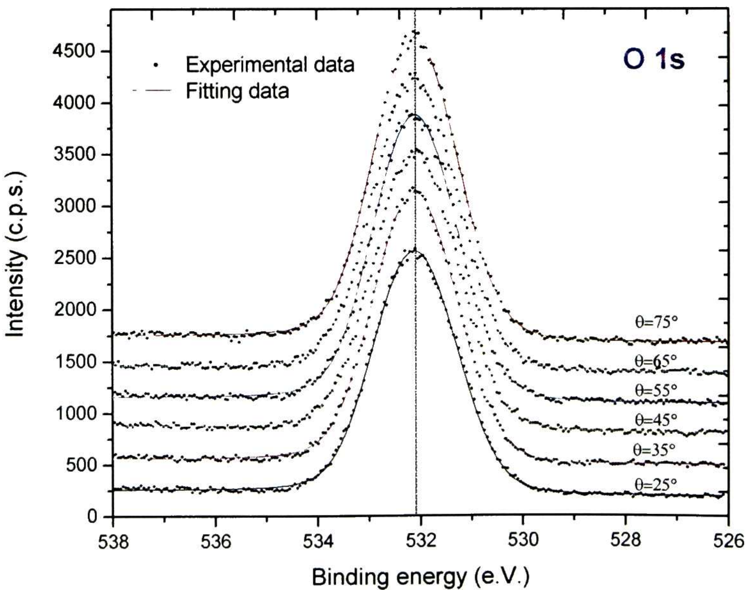

Figure 4.27 Angle Resolved XPS for O 1s region of HfO_2 film on H-terminated Si substrate using 5 ALD cycles.

Figure 4.28 shows the best fits for the C 1s region for all the angles taken. The peak found at 285 eV was assigned to C-C bonds. The peak at 286.3 eV was attributed to C-H bonds. The Lorentzian width for C 1s found was 0.25 eV and is the same value used for C 1s through all the fits. The obtained Gaussian width for this sample was 1.29 eV. The background used for this fit was integral type.

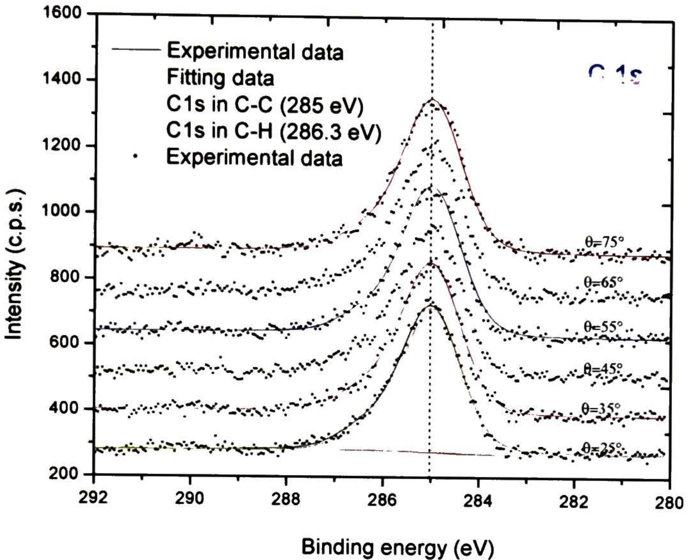

Figure 4.28 Angle Resolve XPS for core level C 1s of HfO_2 film on H-terminated Si substrate using 5 ALD cycles. The spectrum clearly showed two chemical species, one associated to C-C bond (285 eV) and another to C-H bond (286.3 eV).

Figure 4.29 shows the best fits for the F 1s region for all the angles taken. The data was fitted with a peak found at 685.8 eV was assigned to Fluorine. The Lorentzian width for F 1s found was 0.085 eV and is the same value used for F 1s through all the fits. The obtained Gaussian width for this sample was 2.48 eV. The background used for this fit was integral type.

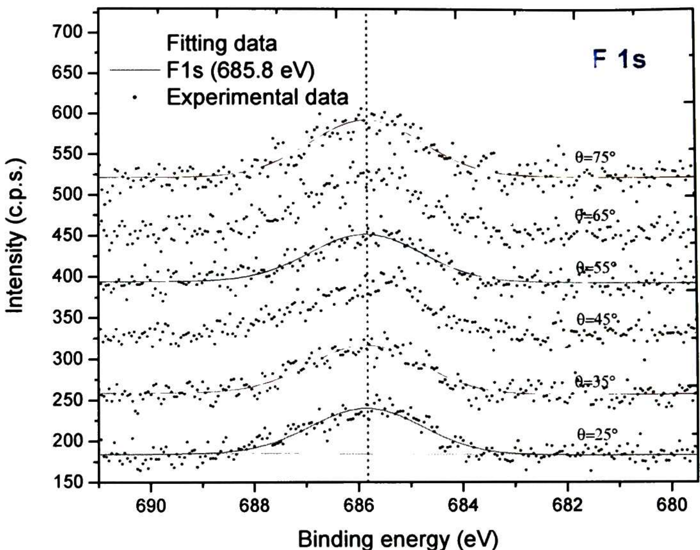

Figure 4.29 Angle Resolve XPS for core level F 1s of HfO_2 film on H-terminated Si substrate using 5 ALD cycles. The spectrum clearly showed one chemical specie associated to Fluorine (685.8 eV).

4.7.5 XPS analysis of HfO_2 on SiO_2-terminated Si Substrate Using 5 ALD cycles

Figure 4.30 shows the Si 2p spectrum at 25° take-off angle for 5 ALD cycles of HfO_2 on a SiO_2-terminated Si substrate. The data was fitted in the same way as in the case of the 5 ALD cycles sample. The Gaussian width for this case was 1.1 eV. All the other peak parameters were kept fixed as indicated in section 4.7.4. In this case the number of Si 2p chemical components are the same as in the previous case.

Comparing the Si 2p region in Figure 4.22 and Figure 4.30 is noticeably the increased Si-O peak. This is due to the SiO_2 starting layer in the later case. Figure 4.31 shows the Si 2p spectra recorded at several take-off angles.

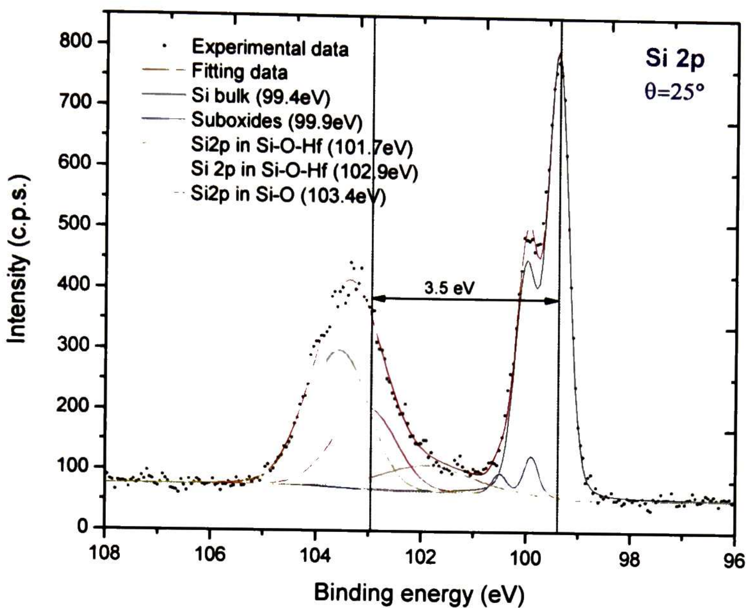

Figure 4.30 Core level Si 2p XPS spectrum at 25° of HfO_2 film on SiO_2-terminated Si substrate using 5 ALD cycles. The binding energy difference between Si in the bulk and in $HfSi_xO_y$ is 3.5 eV.

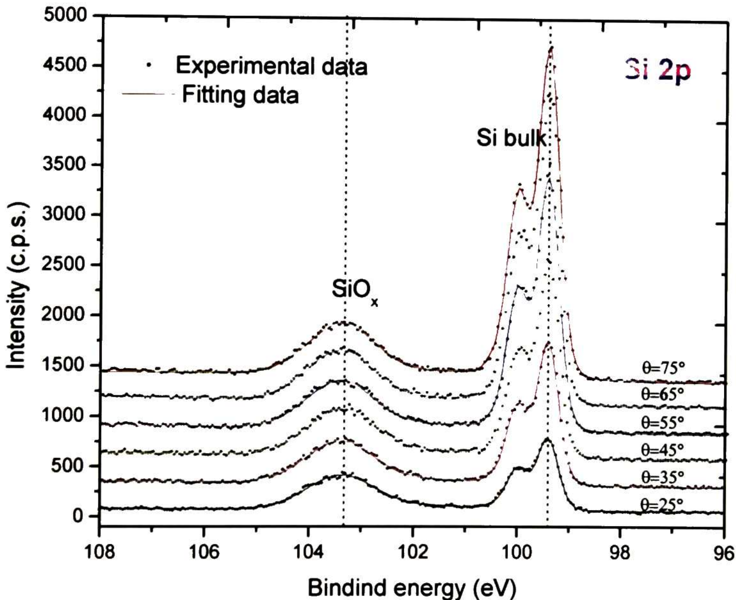

Figure 4.31 Angle Resolved XPS for Si 2p region of HfO_2 film on SiO_2-terminated Si substrate using 5 ALD cycles.

The Hf 4f XPS region for this sample are shown in Figure 4.32. Again, this region was fitted in the same way as in the previous section. However, in this case it was not possible to obtain a good fit using a single chemical component. The two He 4f chemical component found correspond to Hf in hafnium silicate. The binding energies for this two components are 18.1 and 18.8 eV, consistent with the binding energy of Hf in hafnium silicate. The Lorentzian width, spin-orbit splitting and doublet ratio are the same as in the previous section. The Gaussian of the two components are the same with a value of 1.24 eV. The background used was polynomial of second order. Figure 4.33 shows the ARXPS data and fits for Hf 4f.

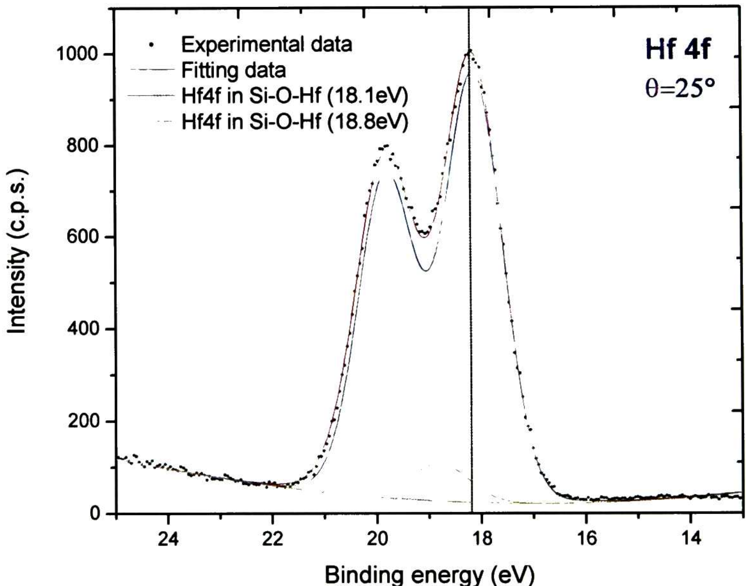

Figure 4.32 Core level Hf 4f XPS spectrum at 25° of HfO_2 film on SiO_2-terminated Si substrate using 5 ALD cycles. The best fitting was done using two peaks. As it is shown in Chapter 5, both corresponding to hafnium silicate.

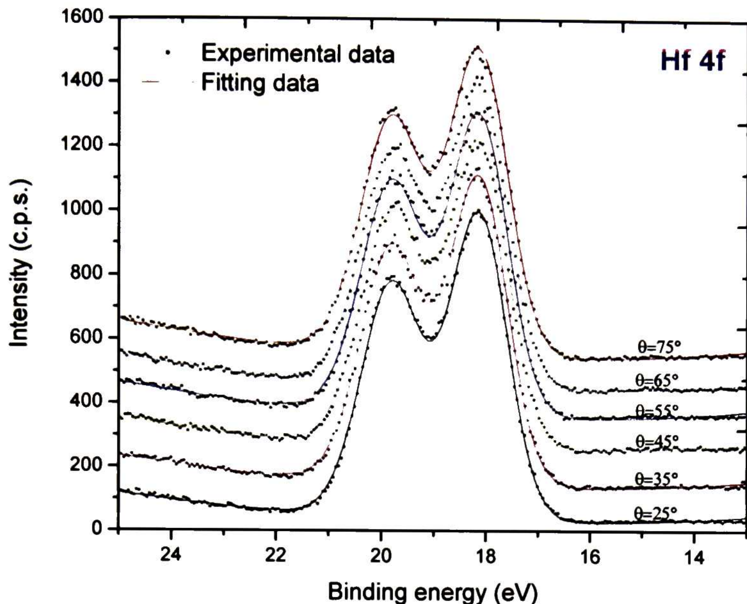

Figure 4.33 Angle Resolved XPS for Hf 4f region of HfO_2 film on SiO_2-terminated Si substrate using 5 ALD cycles. Employing a pass energy of 15eV resulted in high resolution XPS data that allowed for the proper deconvolution of the peaks.

The de-convolution of the O 1s XPS region is shown in Figure 4.34. The data fit shows clearly two oxygen chemical components, similarly to the 5 ALD cycles HfO_2 on H-terminated sample. However in this case the chemical component associated to SiO_2 is substantially larger, respect to Hf-O-Si component, than in the previous case. The Lorentzian width was kept the same as in the previous section. The binding energies obtained for the two chemical components were 532.6 eV for the Si-O-Si bonds and 531.3 eV for the Si-O-He bonds. The Gaussian widths were 1.33 eV for both components. The background used was integral type. Figure 4.35 shows the best fits for O 1s spectra for the several take-off angles recorded.

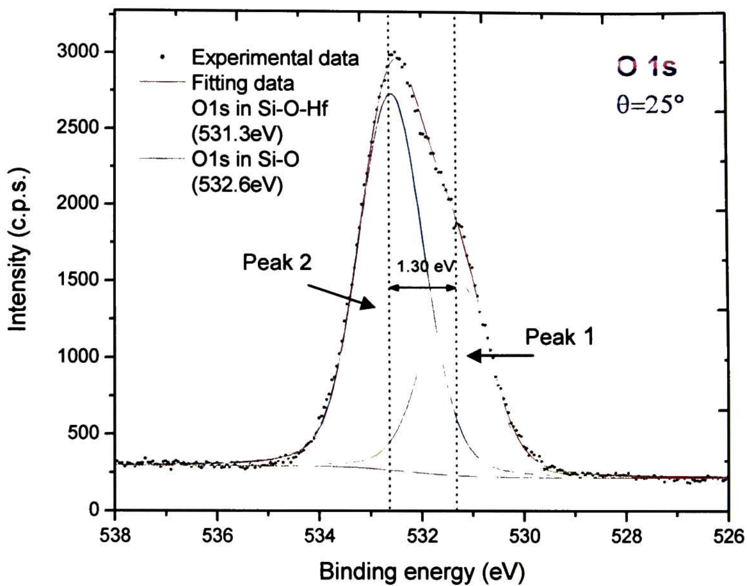

Figure 4.34 Core level O 1s XPS spectrum at 25° of HfO_2 film on SiO_2-terminated Si substrate using 5 ALD cycles. The spectrum clearly showed two peaks separated by 1.30eV, one associated to silicon oxide (532.6eV) and another to silicate (532.6eV).

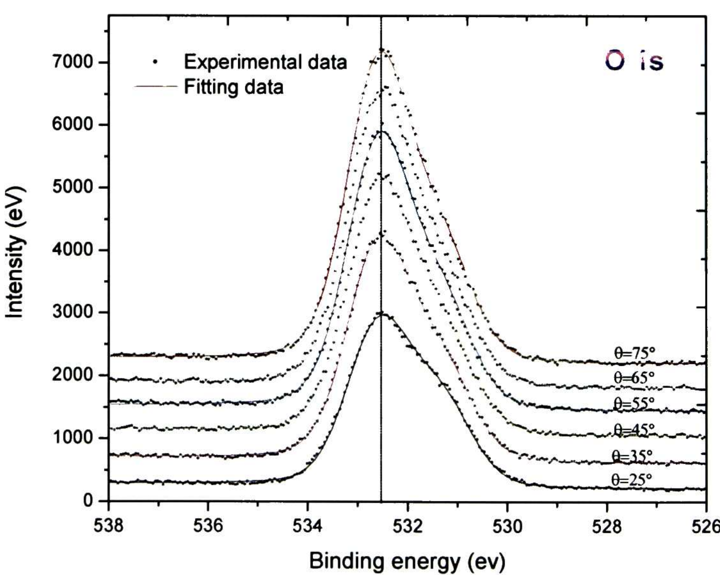

Figure 4.35 Angle Resolved XPS for O 1s region of HfO_2 film on SiO_2-terminated Si substrate using 5 ALD cycles.

Figure 4.36 shows the best fits for the C 1s region for all the angles taken. The peak found at 284.9 eV was attributed to C-C bonds. The peak at 286.2 eV was assigned to C-H bonds. The Lorentzian width for C 1s found was 0.25 eV and is the same value used for C 1s through all the fits. The obtained Gaussian width for this sample was 1.3 eV. The background used for this fit was integral type.

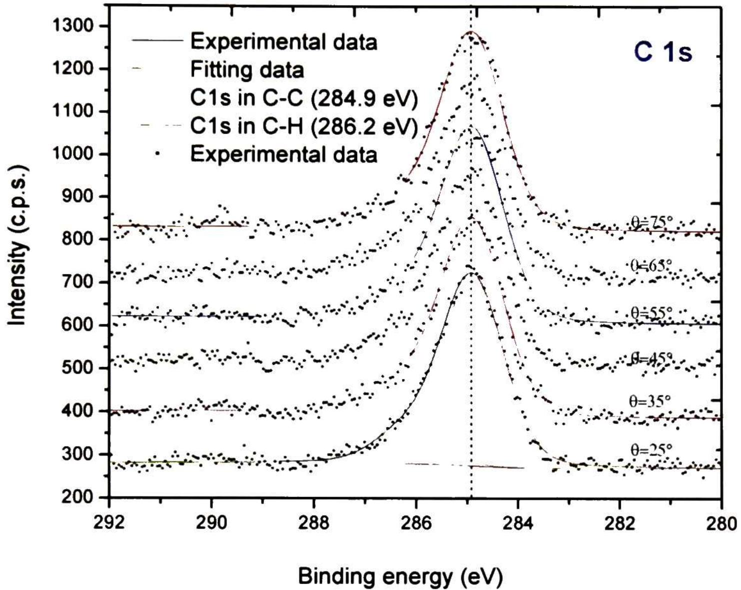

Figure 4.36 Angle Resolve XPS for core level C 1s of HfO_2 film on SiO_2-terminated Si substrate using 5 ALD cycles. The spectrum clearly showed two chemical species, one associated to C-C bond (284.9 eV) and another to C-H bond (286.2 eV).

The region for F 1s is showed in Figure 4.37, it shows the best fits for this region for all the angles taken. The data was fitted with a peak found at 685.5 eV was assigned to Fluorine. The Lorentzian width for F 1s found was 0.085 eV and is the same value used for F 1s through all the fits. The obtained Gaussian width for this sample was 2.24 eV. The background used for this fit was integral type.

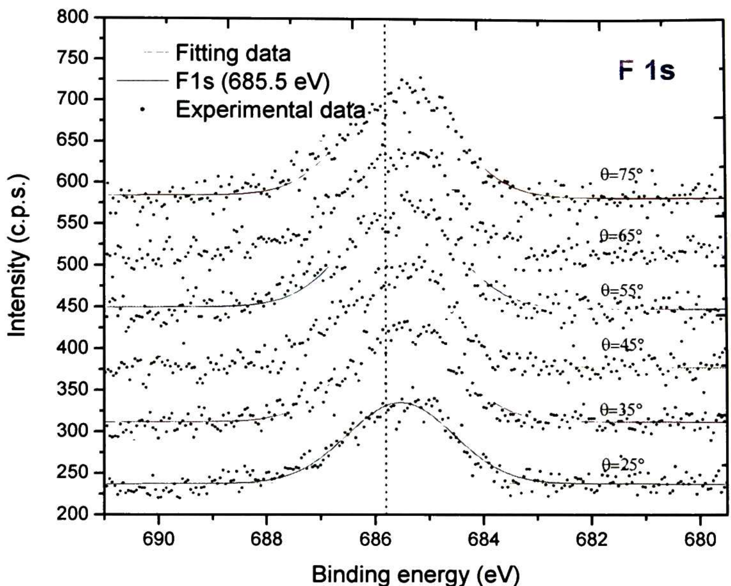

Figure 4.37 Angle Resolve XPS for core level F 1s of HfO_2 film on SiO_2-terminated Si substrate using 5 ALD cycles. The spectrum clearly showed one chemical specie associated to Fluorine (685.5 eV).

4.7.6 XPS Analysis of HfO_2 on H-terminated Si Substrate Using 30 ALD Cycles

This section shows the ARXPS data for Si 2p, Hf 4f and O 1s for a 30 ALD cycles of HfO_2 deposited on a H-terminated Si substrate. Figure 4.38 shows the Si 2p data and fit for a take off angle of 25°. The fit produces the same number of components obtained before in the previous sections with similar fit parameters. The XPS analysis for this data was performed in the same way as in the previous sections. The binding energy positions of the different chemical components are shown in the parenthesis of the plot legends in Figure 4.38. Figure 4.39 shows the corresponding Si 2p spectra for the several take-off angles.

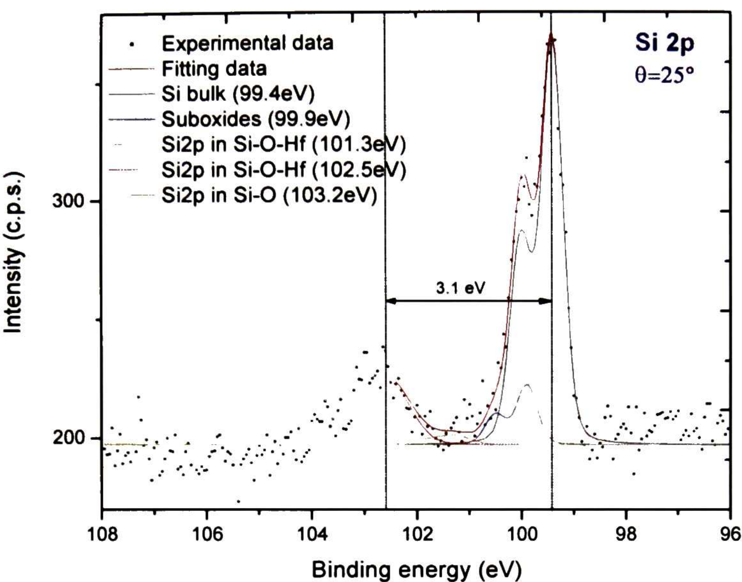

Figure 4.38 Core level Si 2p XPS spectrum at 25° of HfO_2 film on H-terminated Si substrate using 30 ALD cycles. The binding energy difference between Si in the bulk and in $HfSi_xO_y$ in this case is 3.1eV.

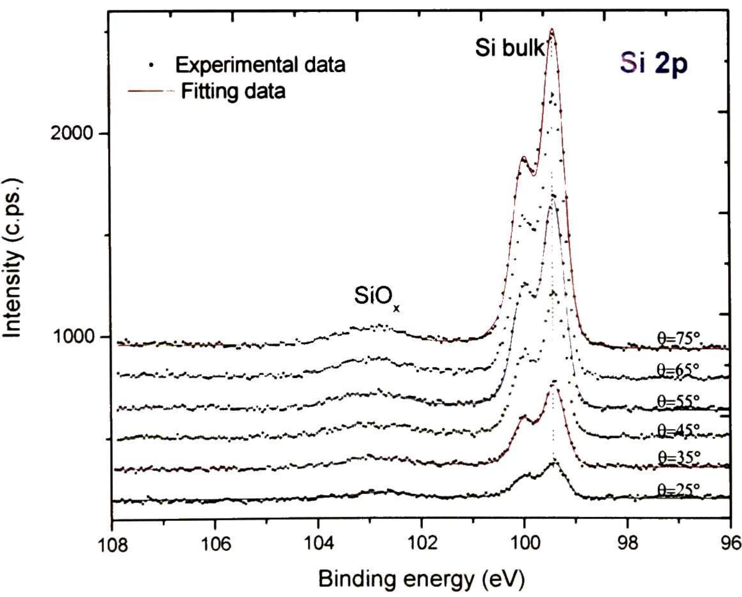

Figure 4.39 Angle Resolved XPS for Si 2p region of HfO_2 film on H-terminated Si substrate using 30 ALD cycles.

Figure 4.40 shows the Hf 4f XPS data and fit. It is clear from the fits that this region is composed by two well separated chemical components. The lower binding energy component (17.9 eV) is attributed to HfO_x formation while the higher binding energy component (18.3 eV) corresponds to the formation of interfacial hafnium silicate (O-Hf-Si bonds). The Gaussian width obtained for the two components was the same with a value of 0.99 eV. This value is considerably smaller than in the case of 5 ALD cycles. This finding indicates an increase in the order of the chemical environment of the Hf atoms bond arrangement. Figure 4.33 shows the XPS fits of the Hf 4f region for the several take-off angles recorded.

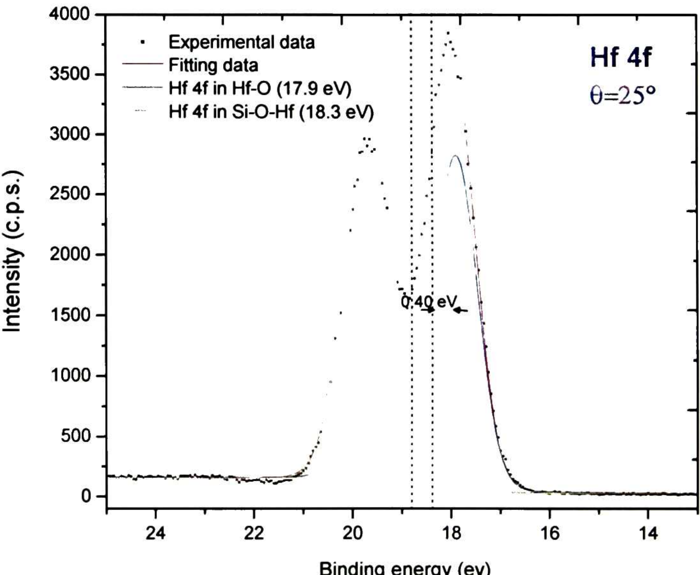

Figure 4.40 Core level Hf 4f XPS spectrum at 25° of HfO_2 film on H-terminated Si substrate using 30 ALD cycles. Two chemical components are present. As it will be shown in Chapter 5, one corresponds to hafnium silicate and another to hafnium oxide. The binding energy difference between them is 0.40 eV.

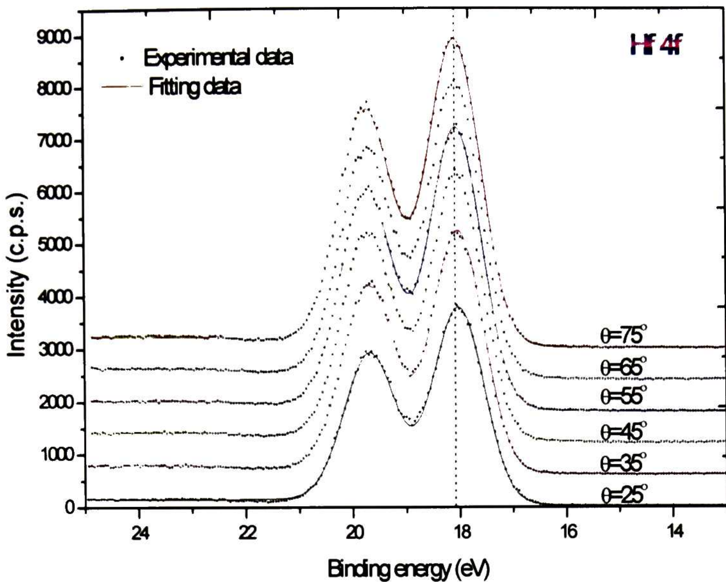

Figure 4.41 Angle Resolved XPS for Hf 4f region of HfO_2 film on H-terminated Si substrate using 30 ALD cycles.

Figure 4.42 shows the O 1s XPS region. The de-convolution of the O 1s XPS region shows at least three components. The lower binding energy component is attributed to HfO_2 while the higher binding energy component is associated with SiO_2. Figure 4.43 shows the fits for the O 1s XPS region for each take-off angle.

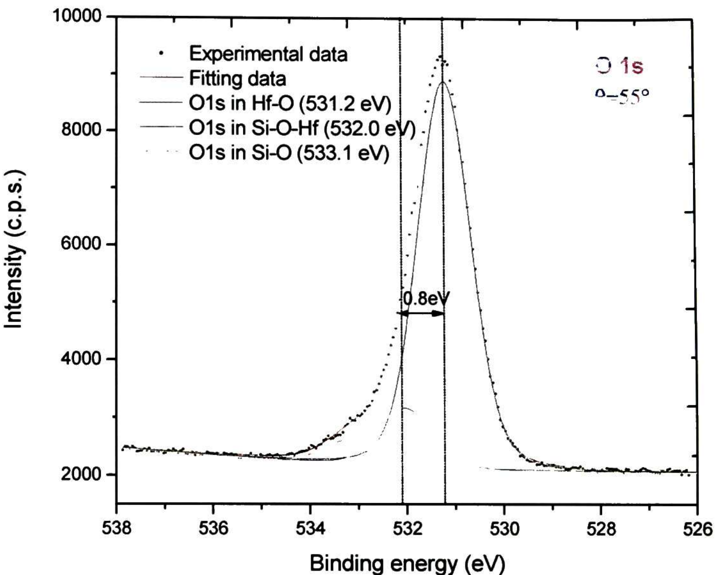

Figure 4.42 Core level O 1s XPS spectrum at 55° of HfO_2 film on H-terminated Si substrate using 30 ALD cycles. The shape of oxygen spectra allows three peaks deconvolution, the first associated to hafnium oxide (531.2eV), the second attributed to hafnium silicate (532eV) and the third to silicon oxide (533.1eV).

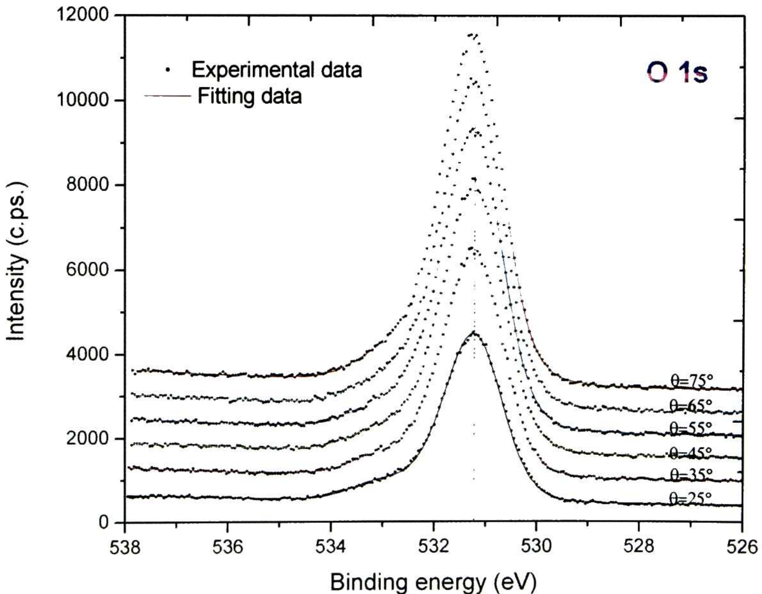

Figure 4.43 Angle Resolved XPS for O 1s region of HfO_2 film on H-terminated Si substrate using 30 ALD cycles.

Figure 4.44 shows the best fits for the C 1s region for all the angles taken. The peak found at 285.3 eV was assigned to C-C bonds. The peak at 286.6 eV was attributed to C-H bonds. The Lorentzian width for C 1s found was 0.25 eV and is the same value used for C 1s through all the fits. The obtained Gaussian width for this sample was 1.29 eV. The background used for this fit was integral type.

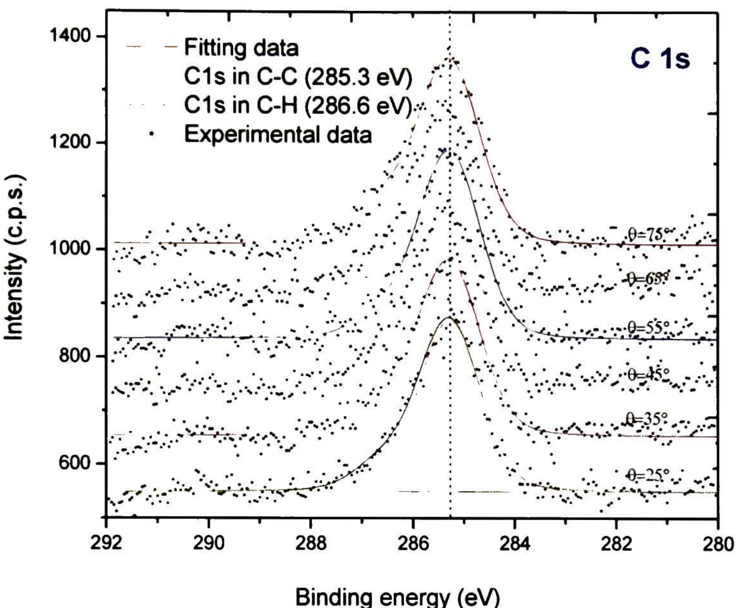

Figure 4.44 Angle Resolve XPS for core level C 1s of HfO_2 film on H-terminated Si substrate using 30 ALD cycles. The spectrum clearly showed two chemical species, one associated to C-C bond (285.3 eV) and another to C-H bond (286.6 eV).

Figure 4.45 shows the best fits for the F 1s region for all the angles taken. The data was fitted with a peak found at 685.6 eV assigned to Fluorine. The Lorentzian width for F 1s found was 0.085 eV and is the same value used for F 1s through all the fits. The obtained Gaussian width for this sample was 1.85 eV. The background used for this fit was integral type.

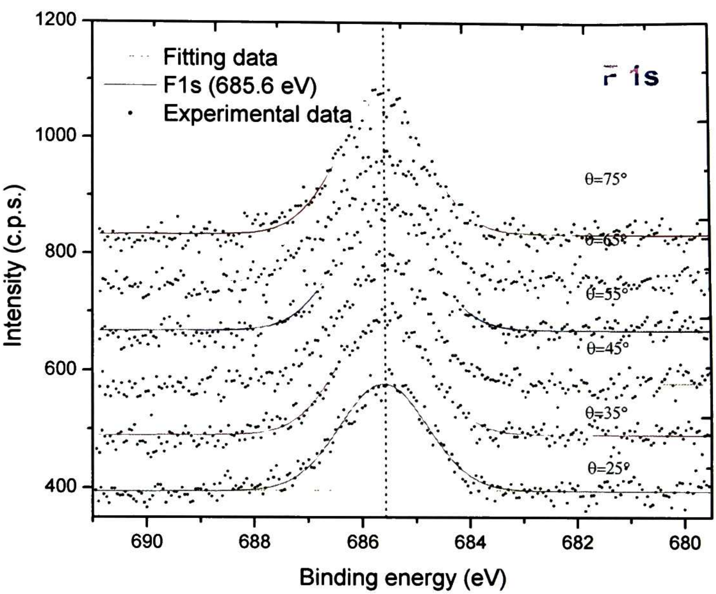

Figure 4.45 Angle Resolve XPS for core level F 1s of HfO_2 film on H-terminated Si substrate using 30 ALD cycles. The spectrum clearly showed one chemical specie associated to Fluorine (685.6 eV).

4.7.7 XPS Analysis of HfO_2 on SiO_2-terminated Si Substrate Using 30 ALD Cycles

We present in this section the ARXPS data and fits for the 30 ALD cycles of HfO_2 on SiO_2 on a Si substrate. Figure 4.46 shows the Si 2p spectrum and fit for the 25° take-off angle XPS data. The fitting was performed as in the previous section. The peak parameters obtained from the fits are summarized in the following section. Figure 4.47 shows the Si 2p spectra recorded at 25, 35, 45, 65 and 75 degrees.

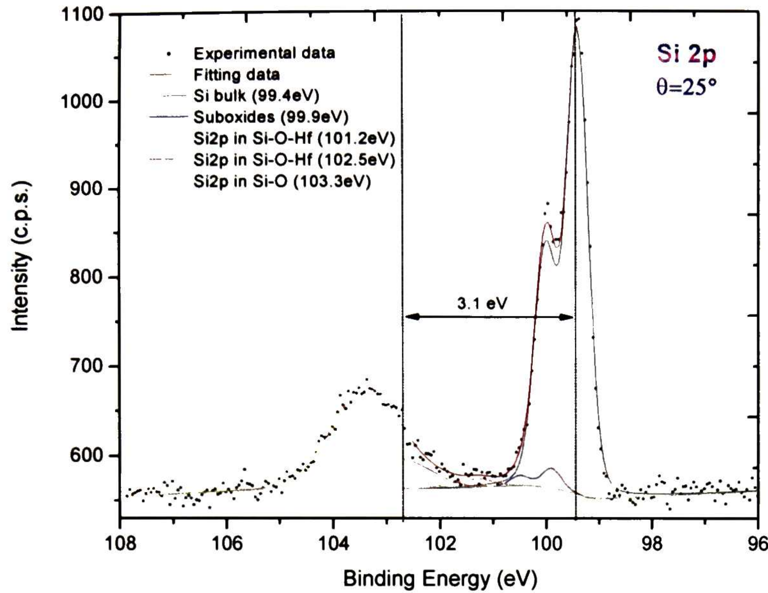

Figure 4.46 Core level Si 2p XPS spectrum at 25° of HfO_2 film on SiO_2-terminated Si substrate using 30 ALD cycles. The binding energy difference between Si in the bulk and in $Hf_{0.77}Si_{0.23}O_{2.12}$ is 3.1 eV.

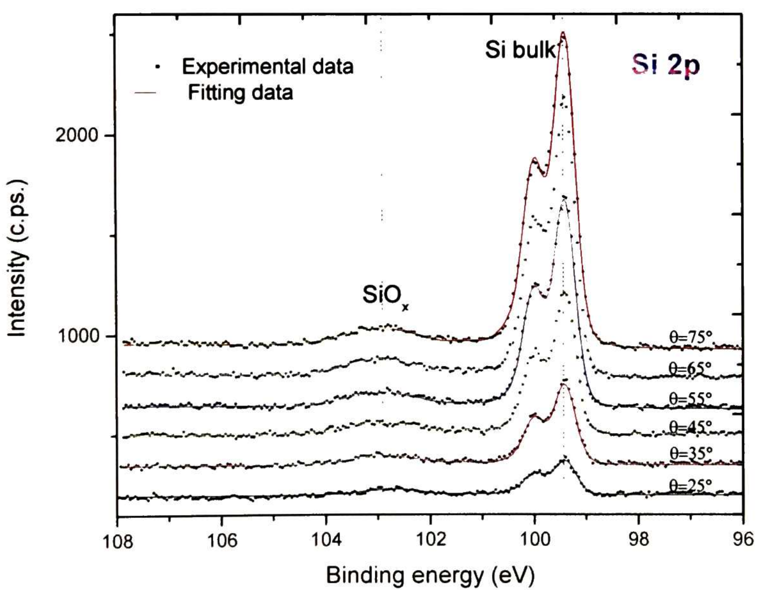

Figure 4.47 Angle Resolved XPS for Si 2p region of HfO_2 film on SiO_2-terminated Si substrate using 30 ALD cycles.

Figure 4.48 depicts the Hf 4f region for this sample clearly showing two peaks as in the 30 ALD cycles of HfO_2 deposited on a H-terminated Si. The two components correspond to the formation of hafnium oxide and hafnium silicate as well. The absence of these two well defined Hf components in the 5 cycles samples indicates that 5 cycles are not enough for the formation of hafnium oxide. The corresponding ARXPS data is shown in Figure 4.49.

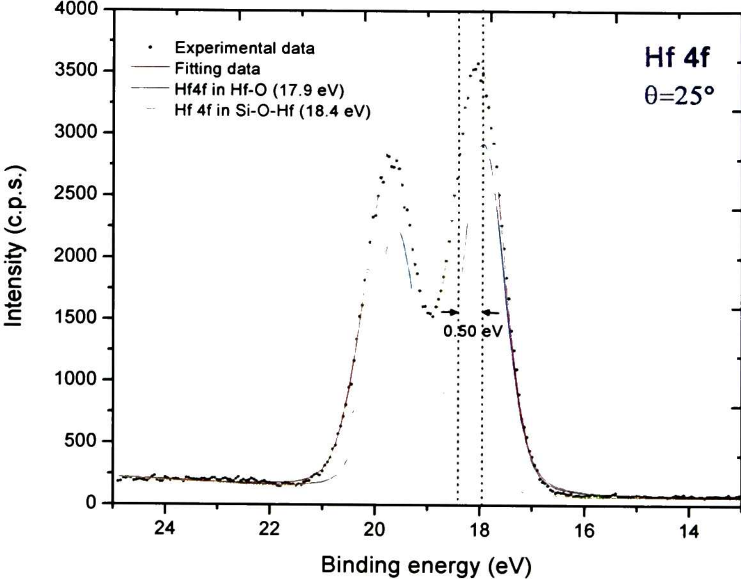

Figure 4.48 Core level Hf 4f XPS spectrum at 25° of HfO_2 film on SiO_2-terminated Si substrate using 30 ALD cycles. Two chemical components are present. As it is shown in Chapter 5, one associated to hafnium silicate and the other to hafnium oxide. The binding energy difference between them is 0.50 eV.

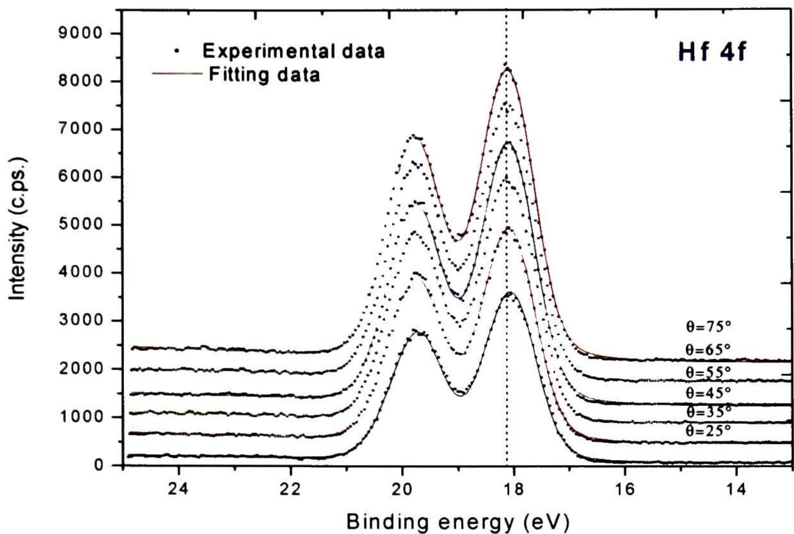

Figure 4.49 Angle Resolved XPS for Hf 4f region of HfO_2 film on SiO_2-terminated Si substrate using 30 ALD cycles.

Also for this same sample, the de-convoluted spectra of O 1s core-level shows three peaks. As is illustrated in Figure 4.50, the first peak centered at 531.3 eV could be assigned to Hf-O bonds, the second peak at 532.4 eV could be attributed to Si-O-Hf bonds and finally the third peak at 533.2 eV correspond to Si-O bonds. Figure 4.51 shows the data and fits for O 1s spectra for the several take-off angles.

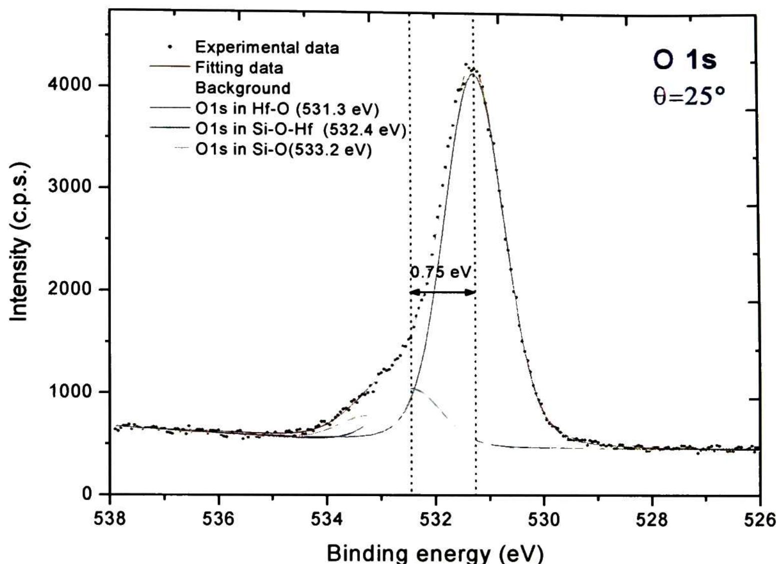

Figure 4.50 Core level O 1s XPS spectrum at 25° of HfO_2 film on SiO_2-terminated Si substrate using 30 ALD cycles. The shape of oxygen spectra allows three peaks deconvolution, one associated to hafnium oxide (531.3eV), other attributed to hafnium silicate (532.4eV) and the last to silicon oxide (533.2eV).

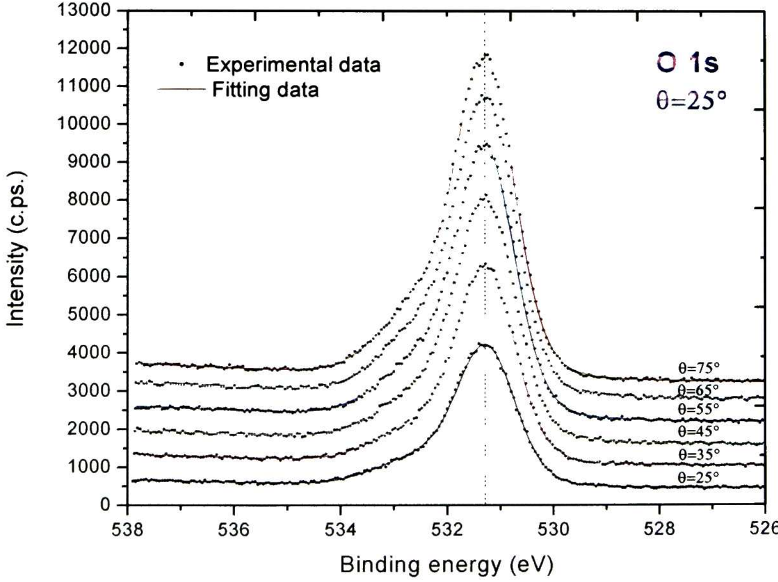

Figure 4.51 Angle Resolved XPS for O 1s region of HfO_2 film on SiO_2-terminated Si substrate using 30 ALD cycles.

Figure 4.52 shows the best fits for the C 1s region for all the angles taken. The peak found at 285.3 eV was assigned to C-C bonds. The peak at 286.6 eV was attributed to C-H bonds. The Lorentzian width for C 1s found was 0.25 eV and is the same value used for C 1s through all the fits. The obtained Gaussian width for this sample was 1.28 eV. The background used for this fit was integral type.

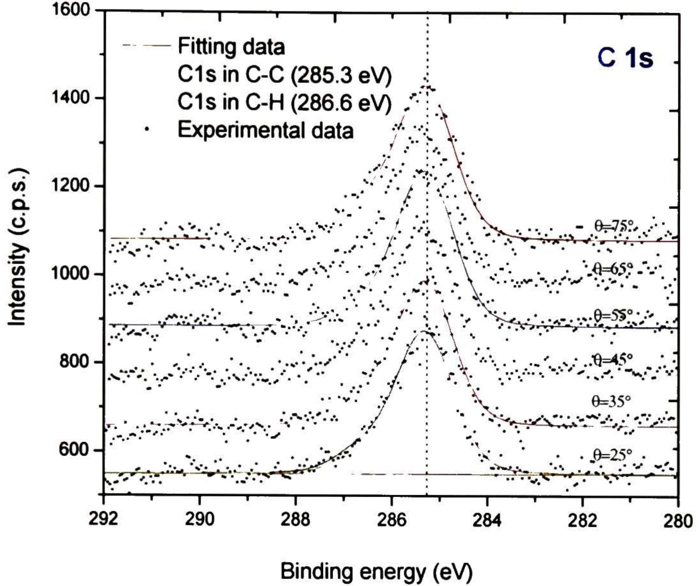

Figure 4.52 Angle Resolve XPS for core level C 1s of HfO_2 film on SiO_2-terminated Si substrate using 30 ALD cycles. The spectrum clearly showed two chemical species, one associated to C-C bond (285.3 eV) and another to C-H bond (286.6 eV).

Figure 4.53 shows the best fits for the F 1s region for all the angles taken. The data was fitted with a peak found at 685.6 eV assigned to Fluorine. The Lorentzian width for F 1s found was 0.085 eV and is the same value used for F 1s through all the fits. The obtained Gaussian width for this sample was 2.48 eV. The background used for this fit was integral type.

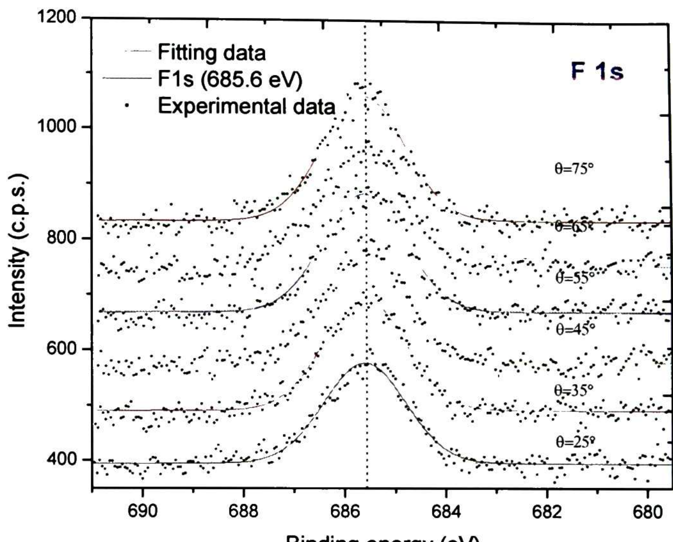

Figure 4.53 Angle Resolve XPS for core level F 1s of HfO_2 film on SiO_2-terminated Si substrate using 30 ALD cycles. The spectrum clearly showed one chemical specie associated to Fluorine (685.6 eV).

4.7.8 Summary of the Fits

The areas obtained from this XPS analysis are shown and discussed in the following chapter. In the practice the XPS data fit was performed in a self-consisting manner in such a way the peak assignation of the chemical components extracted from the XPS fits were initially feed into the ARXPS modeling to find if the depth and thickness approached the expected values. For example it is expected that the SiO_2 or $Hf_xSi_{1-x}O_y$ is found at the HfO_2/Si interface. The XPS fitting and ARXPS modeling steps followed several iterations until a consistent layer structure was obtained. The binding energy values for the XPS peaks of films and substrate obtained from the fits are shown in Table 4.3.

Table 4.3 Summary of binding energy for all the samples studied.

Sample	Binding Energy (eV)							
	Si 2p in			Hf 4f in		O1s in		
	bulk	$Hf_xSi_{1-x}O_y$	SiO_x	$Hf_xSi_{1-x}O_y$	HfOx	SiO_x	$Hf_xSi_{1-x}O_y$	HfOx
H-terminated, 5 ALD cycles	99.4	102.4	103.2	18.2	---	532.4	531.65	---
SiO_2-terminated, 5 ALD cycles	99.4	102.9	103.4	18.1	---	532.6	531.3	---
H-terminated, 30 ALD cycles	99.4	102.5	103.2	18.3	17.9	532	533.1	531.2
SiO_2-terminated, 30 ALD cycles	99.4	102.5	103.3	18.4	17.9	532.4	533.2	531.3

For the Si 2p fits, only the values corresponding to the Si-bulk, SiO_2 and $Hf_xSi_{1-x}O_y$ components are showed. The Hf 4f binding energy values for $Hf_xSi_{1-x}O_y$ are between 18.1 and 18.4 eV. The Hf component in HfO_2 was found at 17.9 eV and in only present in the 30 cycles films. In the particular case of the O 1s, the angular dependence of the individual components was not consistent with the peak assignation. For this reason the O 1s were not modeled individually in the ARXPS data analysis showed in the following chapter. Instead the total O 1s area was used and was distributed all across the film.

Table 4.4 shows the Gaussian widths for the same samples and chemical components showed in Table 4.3.

Table 4.4 Summary of Gaussian values for all the samples studied.

Sample	Gaussian							
	Si 2p in			Hf 4f in		O1s in		
	bulk	$Hf_xSi_{1-x}O_y$	SiOx	$Hf_xSi_{1-x}O_y$	HfOx	SiOx	$Hf_xSi_{1-x}O_y$	HfOx
H-terminated, 5 ALD cycles	0.44	0.94	0.94	1.26	---	1.46	1.45	---
SiO_2-terminated, 5 ALD cycles	0.43	1.11	1.11	1.24	---	1.33	1.33	---
H-terminated, 30 ALD cycles	0.43	0.88	0.88	0.99	0.99	1.15	1.15	1.15
SiO_2-terminated, 30 ALD cycles	0.44	1.13	1.13	0.85	0.85	1.16	1.16	1.16

It is important to state that an increase on the Gaussian width value might be related to an increase in the bond disorder. The bulk Si component presented a relatively fix

Gaussian width, indicating that the bonding structure of this component did not change across the samples, as expected. The Hf 4f components show a substantial reduction of the corresponding Gaussian widths in the two cases of the 30 cycles films.

References (Chapter 4)

1 E.P. Gusev, C. Cabral Jr., M. Copel, C. D'Emic, M. Gridebelyuk, Microelectron. Eng. 69 145 (2003).

2 M. L. Green, M.Y. Ho, B.Busch, G.D. Wilk, T. Joseph, T. Conrad, B. Brijs, W. Vandervorst, P.I. Raisanen, D. Muller, M. Budeand, J. Greazul, J. Appl. Phys. 92, 7168 (2002).

3 A. Deshpande, R. Inman, G. Jursich, C. Takoudis, Microelectron. Eng. 83, 547-552 (2006).

4 "Chemical depth profile of ultrathin nitrided SiO2 films." A. Herrera-Gómez, A. Hegedus, P.L. Meissner. Applied Physics Letters 81, p. 1014 (2002).

5 Z.H. Lu and J. P. McCaffrey, B. Brar, G.D. Wilk, R.M. Wallace, L.C. Feldman, S.P. Tay, Appl. Phys. Lett. 71 (19), 10 November (1997).

6 C. J. Powell, A. Jablonski, S. Tanuma, and D.R. Penn, J. Electron Spectrosc. Relat. Phenom 68, 605 (1994).

7 ALOHA CVD/ALD Materials Specifications, Electronic Performance Materials.

8 A. Herrera-Gomez, F.S. Aguirre-Tostado, Y. Sun, R. Contreras-Guerrero, R.M. Wallace, Y. Hisao, and E. Flint. Rapid Communications, Surface and Interface Analysis. In print.

Chapter 5

Analysis Results and Discussion

In this chapter, the experimental results obtained are analyzed and discussed in detail.

Chapter 5. Analysis Results and Discussion

5.1 Atomic Force Microscopy (AFM)

According to the AFM images, the growth by ALD allows excellent HfO_2 films conformality control with RMS average equal to 0.15 nm. In this context, we confirm that the study based in Angle Resolved XPS is reliable for these samples.

5.2 Fourier Transmission Infrared Spectroscopy (FTIR)

FTIR results showed in Section 4.6 demonstrate that the growth of HfO_2 by ALD were successfully achieved using 30 ALD cycles independently of substrate termination while in the thinner samples (5-cycles) there is not clear evidence of HfO_2 growth. Furthermore, is relevant to mention that the presence of O-Si-O absorption band (~1240 cm^{-1}) is strongly defined in samples with previous thermally growth SiO_2 while the H-terminated samples presented some shifts by ~ 100cm^{-1} or 200cm^{-1} , it is attributed to silicon oxide is not fully formed (there is less than one monolayer). There is a detectable Si-O-Hf band around 1000-1100 cm^{-1} for the HfO_2 films deposited on the substrates terminated with SiO_2. This finding can be explained by either a strong reaction of the SiO_2 with the Hf precursor or by the Si out-diffusion to the surface through HfO_2 during the ALD deposition.

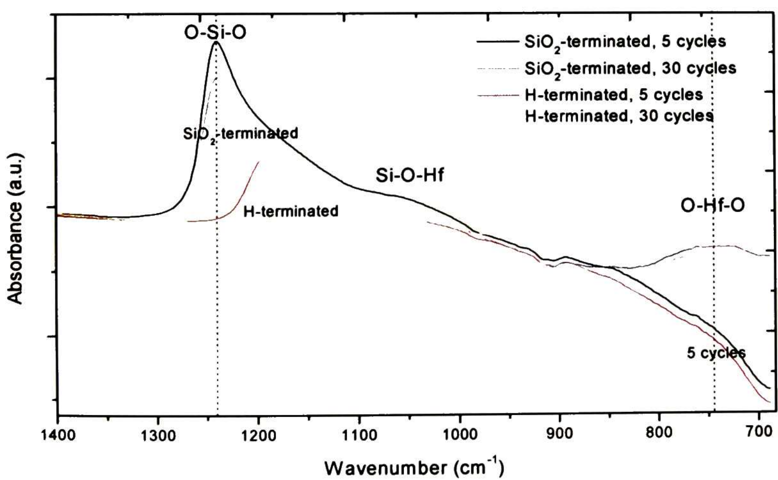

Figure 5.1 Absorption FTIR spectra for samples studied: diferent Si substrate terminated and using 5 or 30 ALD cycles.

5.3 Angle Resolved XPS: Data Analysis

Once calculated the area of each peak de-convoluted, it was possible to evaluate the stoichiometry and thickness of the multilayers formed. This was achieved through an appropriate self consistent analysis of Angle Resolved XPS data by using XPS-Geometry® software (Section 2.6.1). This software uses a numerical algorithm to integrate the photoemission signal for each point of the sample contained in the intersection of the x-ray source beam and the analyzer focal spot for a given take-off angle. Previous to ARXPS measurements, it was necessary to characterize the equipment to know the geometrical parameters of the x-ray source and analyzer focal point. The parameters of the equipment employed for the analysis are showed in the Figure 5.2. In addition to the geometry, this algorithm considers all physical parameters involved in the photoemission as the EAL's, photoionization cross section, and density of the material.

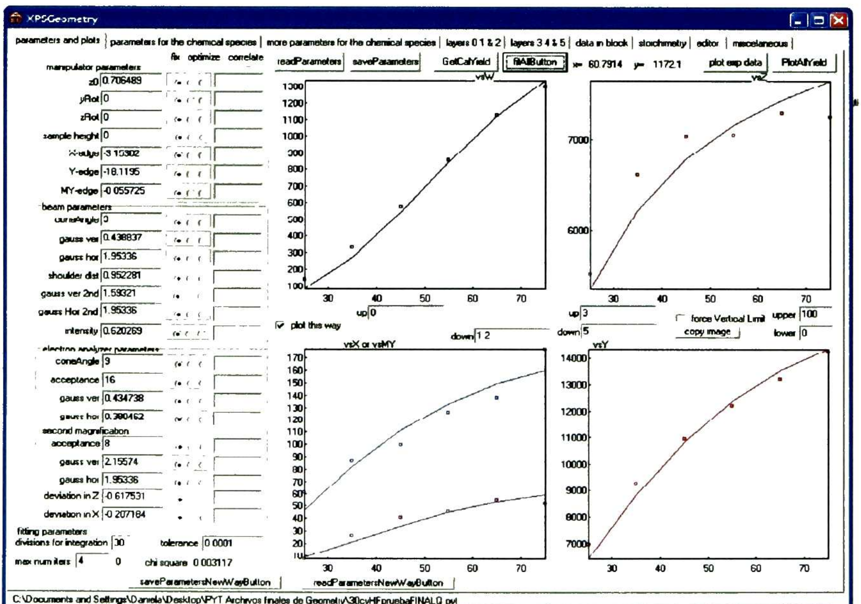

Figure 5.2 Parameters obtained of the equipment characterization.

Figure 5.3 shows the area of Si 2p core level present in the bulk for all the samples. In the 5-cycles films the Si 2p bulk signal is less attenuated because the total thickness of the multilayers on the Si substrate is smaller than for 30-cycles films. In this context, for 30-cycles samples the bulk signal detected is smaller.

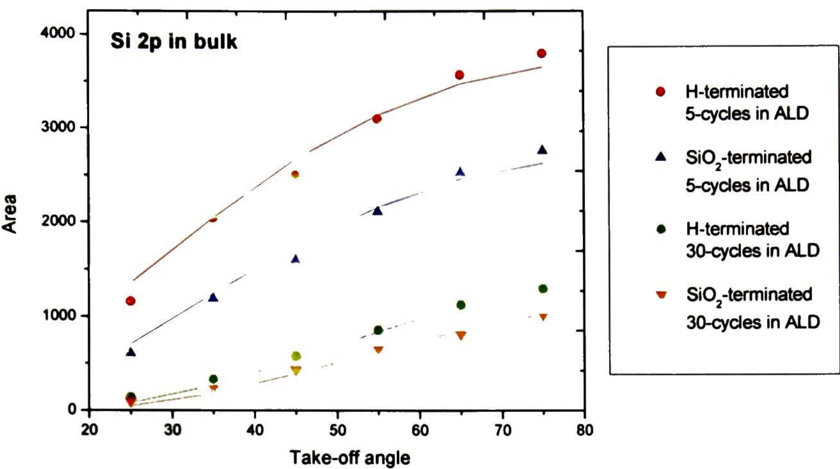

Figure 5.3 ARXPS modeled data for Si 2p in bulk for all four samples studied.

The Figure 5.4 illustrates the ARXPS data for Si 2p component in SiO_x. In the case of HfO_2 films on SiO_2 terminated substrates, the ARXPS data slope is larger indicating that this component is thicker than in the case of H-terminated substrates. For 30-cycles samples it is observed that the SiO_x signal is smaller as it gets buried by the overlayer.

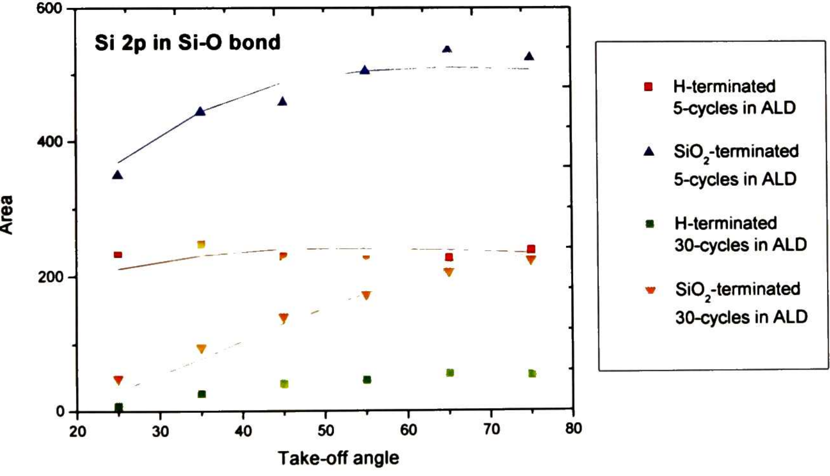

Figure 5.4 Area-angle dependence of Si 2p in Silicon oxide comparing experimental and modeled data.

Figure 5.5 shows the ARXPS areas for the Si 2p component forming Si-O-Hf bonds. The experimental data were successfully modeled for 30-cycles samples while for 5-cycles samples it was not possible to obtain the same quality of the fit. The area indicates that there are more Si2p signal detected in $Hf_xSi_{1-x}O_y$ for 5-cycles samples, it is attributed to layer is in the surface and in the case of 30-cycles samples the layer of hafnium silicate is deeper and it is attenuated for the HfO_2 film on top.

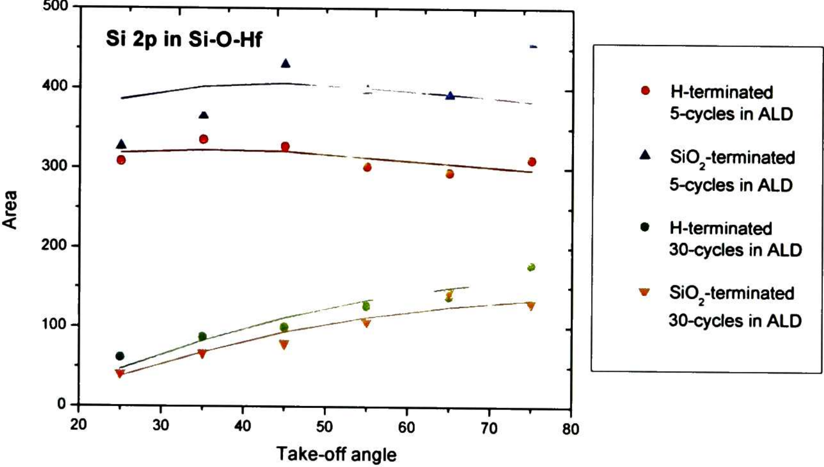

Figure 5.5 Area-angle dependence of Si 2p in Hafnium Silicate comparing experimental and modeled data.

In Figure 5.6 it is illustrated the angular dependence for Hf 4f core level present in hafnium silicate. For 30-cycles samples the dependence indicates that the compound is deep in the film but for 5-cycles samples the compound is close to the surface. Also, for $Hf_xSi_{1-x}O_y$ is evident that the value for x is bigger for 30-cycles than for 5-cycles samples.

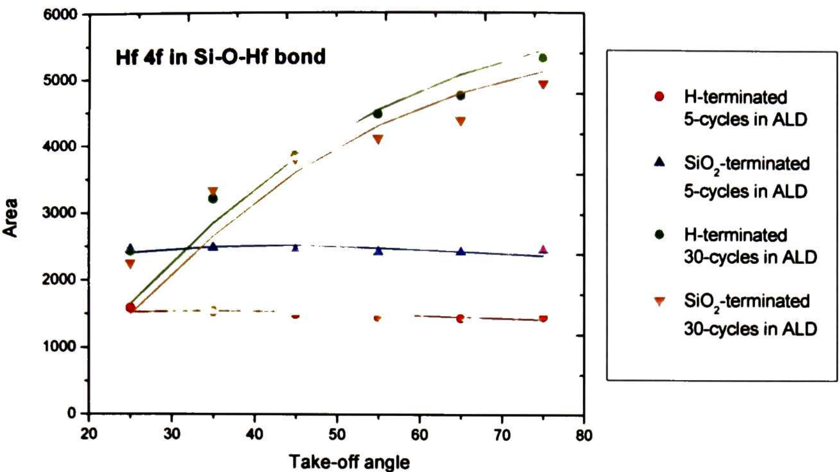

Figure 5.6 Area-angle dependence of Hf 4f in Hafnium Silicate comparing experimental and modeled data.

In Figure 5.7**Error! Reference source not found.** the slopes for 30-cycles samples indicates that O1s is distributed through a layer close to the surface, and there is a bigger amount of hafnium in SiO_2-terminated than H-terminated sample. The 5-cycles samples did not show the chemical component corresponding Hf-O bonds from the Hf 4f peak de-convolution (see sections 4.7.4 and 4.7.5).

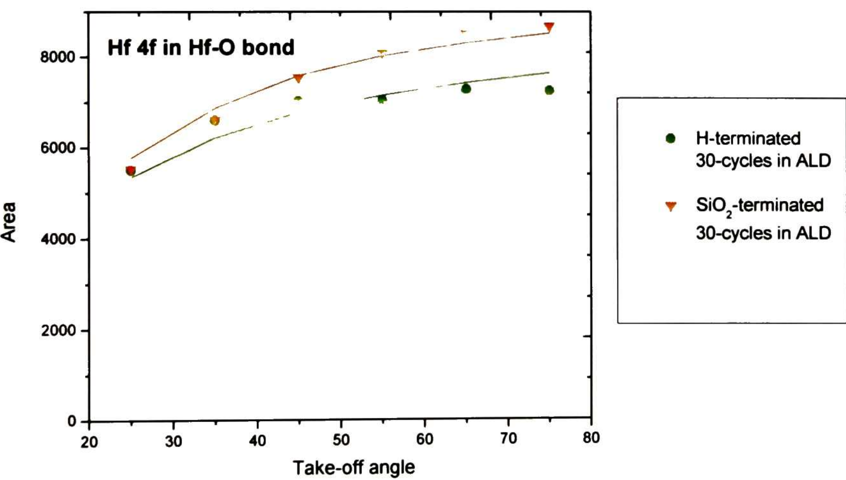

Figure 5.7 Area-angle dependence of Hf 4f in Hafnium Oxide comparing experimental and modeled data.

The qualitative analysis of O 1s core level spectra was performed successfully by means of de-convoluting features, but in the case of quantitative analysis it was not possible to obtain a consistent fitting, then the final analysis was done using the total area of O1s (see Figure 5.8). For 5-cycles samples the dependence suggests that the O 1s is close to the surface of the sample. For 30-cycles samples there is a larger amount of Oxygen and the slope indicates that it is distributed through all the multilayers formed, not depending on the substrate termination.

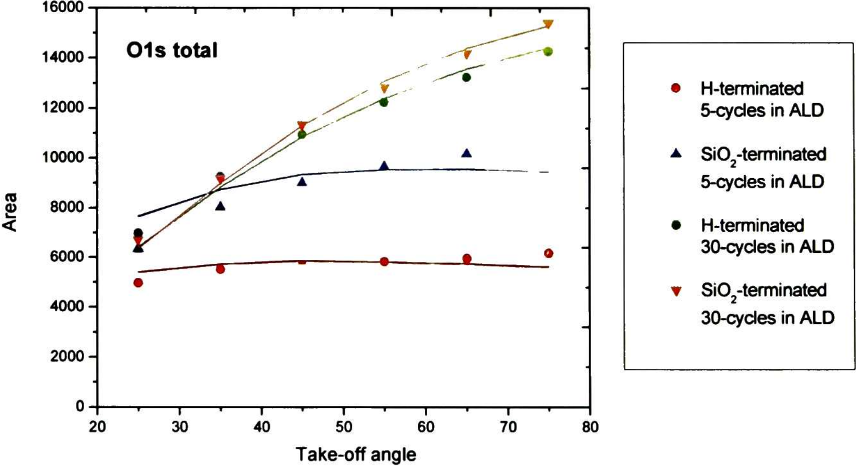

Figure 5.8 Area-angle dependence of O 1s total comparing experimental and modeled data.

5.4 Stoichiometry

Finally, the next table (Table 5.1) shows a schematic representation of each sample with the corresponding stoichiometry, thickness and number of monolayer (ML) formed in each compound.

Table 5.1 Stoichiometry and thickness of the samples.

Sample	Stoichiometry	Layer thickness
H-terminated using 5 ALD cycles	Carbon 1.41 $Hf_{0.33}Si_{0.67}O_{1.62}$ 0.88 $SiO_{1.64}$ Si substrate	Carbon: 0.7 ML (1.5 Å) $Hf_{0.33}Si_{0.67}O_{1.62}$: 1.4 ML (4.7 Å) $SiO_{1.64}$: 0.9 ML (3.1 Å)
SiO_2-terminated using 5 ALD cycles	Carbon 2.26 $Hf_{0.40}Si_{0.60}O_{1.7}$ 2.44 $SiO_{1.71}$ Si substrate	Carbon: 0.8 ML (1.8 Å) $Hf_{0.40}Si_{0.40}O_{1.70}$: 2.3 ML (7.6 Å) $SiO_{1.71}$: 2.4 ML (8.2 Å)
H-terminated using 30 ALD cycles	Carbon 2.62 $HfO_{2.07}$ 4.47 $Hf_{0.77}Si_{0.23}O_{2.12}$ 0.61 $SiO_{2.13}$ & F Si substrate	Carbon: 0.75 ML (1.7 Å) $HfO_{2.07}$: 2.6 ML (8.6 Å) $Hf_{0.77}Si_{0.23}O_{2.12}$: 4.5 ML (15.0 Å) $SiO_{2.13}$: 0.6 ML (2.0 Å)
SiO_2-terminated using 30 ALD cycles	Carbon 3.2 $HfO_{1.98}$ 4.4 $Hf_{0.80}Si_{0.20}O_{2.04}$ 2.8 $SiO_{2.20}$ & F Si substrate	Carbon: 0.5 ML (1.1 Å) $HfO_{1.98}$: 2.8 ML (9.2 Å) $Hf_{0.80}Si_{0.20}O_{2.04}$: 4.0 ML (13.3 Å) $SiO_{2.20}$: 2.8 ML (9.5 Å)

Table 5.1 give us precise information about the transformations of the samples during the HfO_x deposition by ALD. The four different cases of study presented $Hf_xSi_{1-x}O_y$

formation with different value for x and y. The formation of hafnium silicate could be explained by either an intermixing of the HfO2 film during ALD reaction (complex reaction) or Si outdiffusion to the surface through the HfO_2 films during the ALD deposition. In the earlier stages of the deposition (5-cycles samples) the hafnium oxide formation was not achieved, only in 30-cycles samples it was possible to detect and quantify the stoichiometry HfO_x with x~2 for both substrate terminations. The silicate formed for the 5-cycles films is oxygen deficient.

At some extent, the presence of Fluorine was detected in all the samples analyzed. A possible source of contamination might be the ALD reactor.

Also Carbon contamination was found in all samples. Most of this contamination comes from air exposure of the samples during the transport from the ALD chamber to the XPS analysis chamber.

Conclusions

Conclusions

- ALD growth allows obtaining films with good uniformity and conformality.
- HfO_2 growth by ALD induces the formation of a hafnium silicate.
- The FTIR band associated to O-Si-O shifts by ~ 100cm^{-1} or 200cm^{-1} when silicon oxide is not fully formed, i.e., when there is less than one monolayer.
- The FTIR band associated to Si-O-Hf is more distinguishable for the SiO_2 terminated than for the H-terminated substrate.
- Using an analyzer pass energy of 15 eV resulted in high resolution XPS data that allowed the identification of the different chemical species and helping to the proper deconvolution and data analysis.
- By characterizing the XPS equipment, employing a careful quantitative analysis, it was possible to obtain unprecedented details regarding the structure and composition of the studied films. If a layered structure is assumed, the parameters of the layers (i.e. thickness, stoichiometry and depth) can be well determined from the ARXPS data. Once the structure of the film was proposed, the stoichiometry of each layer could be determined.
- The determination of the thickness of the layers depended on the model employed (see Section 4.3.3).
- In the early stages of the HfO_2 growth, the silicate grows faster when the substrate is terminated in SiO_2.
- For the early stages (5 cycles) of HfO_2 growth, the chemical shift of Si 2*p* in the formed hafnium silicate ($Hf_{0.4}Si_{0.6}O_2$) layer varied between 3.0 and 3.5 eV respect to the Si 2*p* in the bulk. This chemical shift variation depended on the substrate termination.
- For later stages the binding energy difference between Si in the bulk and in $Hf_{0.8}Si_{0.2}O_2$ is 3.1 eV for both terminations.

- In the early stages of the growth there is only one chemical component for Hf corresponding to hafnium silicate for the H-terminated substrate and two for the SiO_2 terminated substrate, corresponding to hafnium silicate. For the later stages, the spectra shows two components, one associated to hafnium silicate and another to hafnium oxide for both substrate terminations.
- In the later stages of the growth the binding energy difference between hafnium silicate and hafnium oxide might vary between 0.40 and is 0.50 eV depending on the substrate termination.
- For 5-cycles samples, the oxygen spectra clearly showed two peaks separated by 0.75 eV, one associated to silicon oxide (532.4 eV) and another to hafnium oxide (531.65eV). For 30-cycles samples, the shape of oxygen spectra allows three peaks deconvolution, one associated to silicate (533.1 eV), other attributed to silicon oxide (532 eV) and the last to hafnium oxide (531.2 eV), not depending on the substrate termination. It was possible to make this association because the set of experiments included samples with more silicon oxide than hafnium oxide and vice versa.
- The thickness of the $Hf_xSi_{1-x}O_y$ layer was independent of the substrate termination. In addition, x was 80% for both terminations for the 30-cycles films.
- In the early stages of the ALD growth, the $Hf_xSi_{1-x}O_y$ on the SiO_2- and H-terminated substrates was oxygen deficient, while after 30 cycles it was not.

Future Work

Future Work

Several surface treatments to the Si substrate have been proposed to control the growth of this undesirable interfacial layers and maintain a good interface quality between high-k and Si substrate. A proposed future work for this project is to study the effect of the annealing and nitridation of the grown dielectric films.

Since the structure of the films were characterized in detail, it is interesting to find the effect of the structure on the electrical properties of MOS devices fabricated with these films.

EL JURADO DESIGNADO POR LA UNIDAD QUERÉTARO DEL CENTRO DE INVESTIGACIÓN Y DE ESTUDIOS AVANZADOS DEL INSTITUTO POLITÉCNICO NACIONAL, APROBÓ LA TESIS DE MAESTRÍA LA C. MAYRA DANIELA MORALES ACOSTA TITULADA: "LAS ETAPAS TEMPRANAS DEL CRECIMIENTO POR ALD DE PELÍCULAS DE HfO_2 SOBRE SUBSTRATOS DE Si(001) TERMINADOS EN H Y EN SiO_2" FIRMAN AL CALCE DE COMÚN ACUERDO LOS INTEGRANTES DE DICHO JURADO, EN LA CIUDAD DE QUERÉTARO, QRO., A VEINTISEIS DE NOVIEMBRE DEL DOS MIL SIETE.

DR. ALBERTO HERRERA GÓMEZ

DR. FRANCISCO SERVANDO AGUIRRE TOSTADO

DR. ROBERT M. WALLACE

DR. RAFAEL RAMÍREZ BON

DR. FRANCISCO JAVIER ESPINOZA BELTRÁN

CINVESTAV
BIBLIOTECA CENTRAL
SSIT000006241